

DEVELOPMENT AND APPLICATIONS OF REAL-SPACE
ELECTROSTATIC INTERACTION METHODS FOR
CHARGE-MULTIPOLES IN CONDENSED PHASE ENVIRONMENTS

A Dissertation

Submitted to the Graduate School
of the University of Notre Dame
in Partial Fulfillment of the Requirements
for the Degree of

Doctor of Philosophy

by

Madan Lamichhane,

Kathie E. Newman, Director

J. Daniel Gezelter, Director

Graduate Program in Physics

Notre Dame, Indiana

April 2016

DEVELOPMENT AND APPLICATIONS OF REAL-SPACE
ELECTROSTATIC INTERACTION METHODS FOR
CHARGE-MULTIPOLES IN CONDENSED PHASE ENVIRONMENTS

Abstract

by

Madan Lamichhane

Computing electrostatic interaction is the most expensive portion of a molecular simulation. Generally, traditional and modified Ewald methods are well known for calculating electrostatic interaction in molecular dynamics (MD) communities. But these methods are computationally very expensive for larger system. Nowadays there is a growing interest in developing real space method, scales linearly with the system size. The real space method for the charge-charge interaction was originally developed by *Wolf* and extended by *Gezelter et al.*. In this dissertation, I present three new real-space methods: Shifted Potential (SP), Gradient-Shifted Force (GSF), and Taylor-Shifted Force (TSF), for computing electrostatic interaction between dipoles and quadrupoles. I also discuss the various static and dynamic properties evaluated using newly developed real space methods. Additionally, I present three methods: fluctuation, perturbation, and potential of mean force (PMF) methods, for computing dielectric properties for multipolar fluids.

The SP method is the multipolar version of the *Wolf*'s electrostatic method. Similarly, the GSF and TSF method are natural extension of original Damped Shifted Force (DSF) method developed by *Fennell* and *Gezelter*. The energies

evaluated using SP method shows quantitative agreement with Ewald sum, therefore good choice for monte carlo (MC) simulation. The energies, forces, and torques calculated from the GSF method agrees with the Ewald's result and produce excellent conservation of energy in MD simulations. Both SP and GSF method with suitable damping parameter performs remarkably well in predicting static and dynamic properties of the liquid systems.

For the both dipolar and quadrupolar fluids, the dielectric properties predicted using perturbation method agree with fluctuation formula. We need a correction factor to obtain the dielectric constant and susceptibility from the directly measurable polarizability from the simulation. I tabulate the correction factors for both dipolar and quadrupolar fluid for all real-space as well as Ewald method. Finally, the dielectric screening from the perturbation and fluctuation method are compared with directly measured screening factor using PMF method.

To my late father Hari Bahadur Lamichhane and mother Dropati Lamichhane
for their hard work, consistent support, love, and inspiration.

CONTENTS

FIGURES	vi
TABLES	xi
ACKNOWLEDGMENTS	xii
CHAPTER 1: INTRODUCTION	1
1.1 Molecular Dynamics (MD) Simulations	3
1.1.1 Periodic Boundary Condition (PBC)	7
1.1.2 Spherical truncation and Neighbor lists	9
1.2 Monte Carlo (MC) Simulation	9
1.3 Electrostatic Methods	11
1.3.1 Ewald Method	12
1.3.2 Fourier-based Ewald Methods	15
1.3.2.1 Particle-Particle Particle-Mesh Ewald (PP PME)	15
1.3.2.2 Particle-Mesh Ewald (PME)	17
1.3.3 Real Space Methods	17
CHAPTER 2: DEVELOPMENT OF METHODS	24
2.1 Introduction	24
2.2 Methodology	26
2.2.1 Self-neutralization, damping, and force-shifting	27
2.2.2 The multipole expansion	28
2.2.3 Damped Coulomb interactions	31
2.2.4 Shifted-force methods	32
2.2.5 Taylor-shifted force (TSF) electrostatics	33
2.2.6 Gradient-shifted force (GSF) electrostatics	35
2.2.7 Generalization of the Wolf shifted potential (SP)	36
2.2.8 Body and space axes	37
2.2.9 The Self-Interaction	39
2.3 Interaction energies, forces, and torques	40

2.3.1	Forces	41
2.3.2	Torques	45
2.4	Comparison to known multipolar energies	46
2.5	Summary	51
CHAPTER 3: COMPARISONS WITH THE EWALD SUM		54
3.1	Introduction	54
3.2	Methodology	58
3.2.1	Implementation	61
3.2.2	Model systems	62
3.2.3	Accuracy of Energy Differences, Forces and Torques	63
3.2.4	Analysis of vector quantities	64
3.2.5	Energy conservation	65
3.3	Results	66
3.3.1	Configurational energy differences	66
3.3.2	Magnitude of the force and torque vectors	68
3.3.3	Directionality of the force and torque vectors	69
3.3.4	Energy conservation	72
3.3.5	Reproduction of Structural & Dynamical Features	74
3.4	Summary	80
CHAPTER 4: DIELECTRIC PROPERTIES		83
4.1	Introduction	83
4.2	Dipolar Fluids and the Dielectric Constant	87
4.2.1	Response to External Perturbations	87
4.2.2	Fluctuation Formula	88
4.2.3	Correction Factors	89
4.3	Quadrupolar Fluids and the Quadrupolar Susceptibility	94
4.3.1	Response to External Perturbations	94
4.3.2	Fluctuation Formula	95
4.3.3	Correction Factors	95
4.4	Screening of Charges by Multipolar Fluids	102
4.5	Simulation Methodology	103
4.6	Results	107
4.6.1	Dipolar fluid	107
4.6.2	Quadrupolar fluid	111
4.7	Summary	115
CHAPTER 5: CONCLUSIONS		117

APPENDIX A:	120
A.1 Smith's $B_l(r)$ functions for damped-charge distributions	120
A.2 The r -dependent factors for TSF electrostatics	121
A.3 The r -dependent factors for GSF electrostatics	123
APPENDIX B:	124
B.1 Contraction of the quadrupolar tensor with the traceless quadrupole moment	124
B.2 Quadrupolar correction factor for the Ewald-Kornfeld (EK) method	126
B.3 Generating Uniform Field Gradients	128
B.4 Point-multipolar interactions with a spatially-varying electric field	132
B.5 Boltzmann averages for orientational polarization	134
B.5.1 Dipoles	135
B.5.2 Quadrupoles	136
B.6 Gradient of the field due to quadrupolar polarization	137
B.7 Quadrupole tensors and electric field gradients	140
B.7.1 General results	141
B.7.2 Special cases of quadrupole tensors	143
B.8 Alternative method for calculating correction factor B	145
BIBLIOGRAPHY	149

FIGURES

1.1	Schematic figure showing the step-by-step process in Molecular dynamics simulation.	5
1.2	Periodic Boundary Condition for two dimensional (2D) molecular system. The central box is outlined using thicker line and replicated throughout the plane to form a 2D lattice. Usually in molecular simulations, the potential energy of the molecule is evaluated considering its interactions with the molecules or their images located in the spherical cutoff region as shown in blue dotted-circle. . . .	8
1.3	Region of neighbor list around the cutoff sphere. Molecules in the cutoff region, neighbour list, and outer region are indicated by green, yellow, and violet circles respectively. The neighbour list should be reconstructed before molecules in the outer region starts to penetrate the cutoff region.	10
1.4	In the Ewald method each point charge is surrounded by a Gaussian distribution of equal and oppositely-signed charge, evaluated in real-space. These Gaussian distributions are compensated by the opposite-singed Gaussian distribution of the charges calculated in reciprocal-space	14
1.5	Schematic diagram for Fourier-based Ewald methods where green circle represents charge and blue star denotes grid point. In the Figs., (i) a system of charges, (ii) charges mapped with grid points, (iii) force evaluated at the grid points, and (iv) force mapped back to the particles and their positions and velocities are updated. . .	16
1.6	Schematic diagram showing grouping of ions in (a) 1D (b) 2D crystals. The interaction of the central ion with the group of ions decays faster than $1/r$. The direct spherical truncation breaks the ordering of the ions at the cut off sphere providing a net charge within the cutoff sphere. The breaking of the charge ordering increases with the crystal dimension resulting in a large net charge in the higher dimensional crystal.	19

1.7	Convergence of the lattice energy constants for a 3D NaCl crystal as a function of cutoff radius for the direct (hard) cutoff method (black line). The orange line in the figure is for charge neutralized cutoff sphere (when image charge placed on the surface of the cutoff sphere). The red dotted line represents Madelung energy for NaCl crystal	21
1.8	Convergence of the lattice energy constants for the NaCl crystal as a function of net charge within a cutoff sphere. The red dotted line represents Madelung energy for NaCl crystal	22
2.1	Reversed multipoles are projected onto the surface of the cutoff sphere. The forces, torques, and potential are then smoothly shifted to zero as the sites leave the cutoff region.	29
2.2	Convergence of the lattice energy constants as a function of cutoff radius (normalized by the lattice constant, a) for the new real-space methods. Three dipolar crystal structures were sampled, and the analytic energy constants for the three lattices are indicated with grey dashed lines. The left panel shows results for the undamped kernel ($1/r$), while the damped kernel, $B_0(r)$ was used in the center and right panels.	48
2.3	Convergence of the lattice energy constants as a function of cutoff radius (normalized by the lattice constant, a) for the new real-space methods. Three quadrupolar crystal structures were sampled, and the analytic energy constants for the three lattices are indicated with grey dashed lines. The left panel shows results for the undamped kernel ($1/r$), while the damped kernel, $B_0(r)$ was used in the center and right panels. Note that for quadrupoles, $\alpha^* = 0.4$ overdamps contributions from repulsive orientations in the perfect crystal.	50
3.1	Top: Ionic systems exhibit local clustering of dissimilar charges (in the smaller grey circle), so interactions are effectively charge-multipole at longer distances. With hard cutoffs, motion of individual charges in and out of the cutoff sphere can break the effective multipolar ordering. Bottom: dipolar crystals and fluids have a similar effective <i>quadrupolar</i> ordering (in the smaller grey circles), and orientational averaging helps to reduce the effective range of the interactions in the fluid. Placement of reversed image multipoles on the surface of the cutoff sphere recovers the effective higher-order multipole behavior.	56

3.2	Statistical analysis of the quality of configurational energy differences for the real-space electrostatic methods compared with the reference Ewald sum. Results with a value equal to 1 (dashed line) indicate ΔE values indistinguishable from those obtained using the multipolar Ewald sum. Different values of the cutoff radius are indicated with different symbols (9 Å = circles, 12 Å = squares, and 15 Å = inverted triangles).	67
3.3	Statistical analysis of the quality of the force vector magnitudes for the real-space electrostatic methods compared with the reference Ewald sum. Results with a value equal to 1 (dashed line) indicate force magnitude values indistinguishable from those obtained using the multipolar Ewald sum. Different values of the cutoff radius are indicated with different symbols (9 Å = circles, 12 Å = squares, and 15 Å = inverted triangles).	70
3.4	Statistical analysis of the quality of the torque vector magnitudes for the real-space electrostatic methods compared with the reference Ewald sum. Results with a value equal to 1 (dashed line) indicate force magnitude values indistinguishable from those obtained using the multipolar Ewald sum. Different values of the cutoff radius are indicated with different symbols (9 Å = circles, 12 Å = squares, and 15 Å = inverted triangles).	71
3.5	The circular variance of the direction of the force and torque vectors obtained from the real-space methods around the reference Ewald vectors. A variance equal to 0 (dashed line) indicates direction of the force or torque vectors are indistinguishable from those obtained from the Ewald sum. Here different symbols represent different values of the cutoff radius (9 Å = circle, 12 Å = square, 15 Å = inverted triangle)	73
3.6	Energy conservation of the real-space methods for the soft DQ liquid / ion system. δE_1 is the linear drift in energy over time (in kcal/mol/particle/ns) and δE_0 is the standard deviation of energy fluctuations around this drift (in kcal/mol/particle). Points that appear in the green region at the bottom exhibit better energy conservation than would be obtained using common parameters for Ewald-based electrostatics.	75

3.7	Comparison of the structural and dynamic properties for the combined multipolar liquid (soft DQ liquid + ions) for all of the real-space methods with $r_c = 12 \text{ \AA}$. Electrostatic energies, $\langle U_{\text{elect}} \rangle / N$ (in kcal / mol), coordination numbers, n_C , diffusion constants (in $10^{-5} \text{ cm}^2 \text{ s}^{-1}$), and rotational correlation times (in ps) all show excellent agreement with Ewald results for damping coefficients in the range $\alpha = 0.175 \rightarrow 0.225 \text{ \AA}^{-1}$	79
4.1	Dielectric properties of a fluid measure the response to external electric fields and gradients (left), or internal fields and gradients generated by the molecules themselves (center), or fields produced by embedded ions (right). The dielectric constant (ϵ) measures all three responses in dipolar fluids (top). In quadrupolar liquids (bottom), the relevant bulk property is the quadrupolar susceptibility (χ_Q), and the geometry of the field determines the effective dielectric screening.	86
4.2	In the real-space electrostatic methods, the molecular dipole tensor, $\mathbf{T}_{\alpha\beta}(r)$, is not the same for charge-charge interactions as for point dipoles (left panel). The same holds true for the molecular quadrupole tensor (right panel), $\mathbf{T}_{\alpha\beta\gamma\delta}(r)$, which can have distinct forms if the molecule is represented by charges, dipoles, or point quadrupoles.	90
4.3	The polarizability (α_D), correction factor (A), and dielectric constant (ϵ) for the test dipolar fluid. The left panels were computed using external fields, and those on the right are the result of equilibrium fluctuations. In the GSF and SP methods, the corrections are large in with small values of α , and a optimal damping coefficient is evident around 0.25 \AA^{-1} . The dashed lines in the upper panel indicate back-calculation of the polarizability using the Ewald estimate (Refs.[1] and [2]) for the dielectric constant.	108
4.4	The distance-dependent screening factor, $\epsilon(r)$, between two ions immersed in the dipolar fluid. The new methods are shown in separate panels, and different values of the damping parameter (α) are indicated with different symbols. All of the methods appear to be converging to the bulk dielectric constant (~ 65) at large ion separations.	110

4.5	The quadrupole polarizability (α_Q), correction factor (B), and susceptibility (χ_Q) for the test quadrupolar fluid. The left panels were computed using external field gradients, and those on the right are the result of equilibrium fluctuations. The GSF and SP methods allow nearly unmodified use of the “conducting boundary” or polarizability results in place of the bulk susceptibility.	112
4.6	The distance-dependent screening factor, $\epsilon(r)$, between two ions immersed in the quadrupolar fluid. Results from the perturbation and fluctuation methods are shown in right and central panels. Here the susceptibility is calculated from the simulation and the geometrical factor is evaluated analytically, using the field and field-gradient produced by ions. The right hand panel shows the screening factor obtained from the PMF calculations.	114

TABLES

2.1	Self-interaction contributions for site (a) that has a charge (C_a), dipole (\mathbf{D}_a), and quadrupole (\mathbf{Q}_a)	40
2.2	Radial functions used in the energy and torque equations. The f, g, h, s, t , and u functions used in this table are defined in Appendices A.2 and A.3. The gradient shifted (GSF) functions include the shifted potential (SP) contributions (<i>cf.</i> Eqs. 2.23 and 2.25). .	42
2.3	Radial functions used in the force equations. Gradient shifted (GSF) functions are constructed using the shifted potential (SP) functions. Some of these functions are simple modifications of the functions found in Table 2.2	43
3.1	The parameters used in the systems used to evaluate the new real-space methods. The most comprehensive test was a liquid composed of 2000 soft DQ liquid molecules with 48 dissolved ions (24 Na+ and 24 Cl- ions). This test exercises all orders of the multipolar interactions developed in the chapter 2.	59
4.1	Expressions for the dipolar correction factor (A) for the real-space electrostatic methods in terms of the damping parameter (α) and the cutoff radius (r_c). The Ewald-Kornfeld result derived in Refs.[1–3] is shown for comparison using the Ewald convergence parameter (κ) and the real-space cutoff value (r_c).	93
4.2	Expressions for the quadrupolar correction factor (B) for the real-space electrostatic methods in terms of the damping parameter (α) and the cutoff radius (r_c). The units of the correction factor are length^{-2} for quadrupolar fluids.	101
4.3	The parameters used in simulations to evaluate the dielectric response of the new real-space methods.	105
B.1	Potential energy (U), force (\mathbf{F}), and torque (τ) expressions for a multipolar site at \mathbf{r} in an electric field, $\mathbf{E}(\mathbf{r})$ using the definitions of the multipoles in Eqs. (B.22), (B.23) and (B.24).	134

ACKNOWLEDGMENTS

First of all, I would like to express my deepest appreciations to my advisors, Professor Kathie E. Newman and Professor J. Dainel Gezelter for their persistent guidance, support, and inspiration. Without their help this dissertation would not have been possible.

I am grateful to my dissertation committee; Professor Morten Eskildsen, Professor Mark Alber, and Professor Rebecca Surman, for their valuable time, support, and suggestions. I am also thankful my research group: Dr. Joseph Michalka, Patrick Loudon, Suzanne Kucera, Hemanta Bhattacharai, Dr. Kelsey Stocker, and Thomas Parsons for their help, support, and valuable discussion.

I am very grateful to my wife Sumitra for her unconditional love, support, inspiration, and great patience throughout the course of my PhD research. Without her, completing research would not be this easy for me. I am also very thankful to my Parents: Hari B. Lamichhane and Dropati Lamichhane, Brothers: Bishal and Prabin, and Sisters: Indira and Rekha. My family has always been great source of inspiration for me. Without their support and encouragement, I would not have achieved this opportunity. I am indebted to my friends: Aboutaleb Amiri and Melinda Varga for their valuable support and discussion.

Financial support for this research was provided by the National Science Foundation (NSF) under grant CHE-1362211 and computational time was provided by the Center for Research Computing (CRC) at the University of Notre Dame.

CHAPTER 1

INTRODUCTION

In computer simulation of condensed phase molecular systems, molecules are commonly represented by atomic sites that interact via a parametrized force field. This force field aims to reproduce observable phenomena by incorporating the proper physics into the simulation. There are mainly two types of interaction; intramolecular and intermolecular which determines the static and dynamic properties of the molecular systems. An intramolecular interaction is the interaction within a single molecule including, bonding, bending, and torsional motion whereas an intermolecular interaction is the interaction between two or more molecules and includes van der Waals and electrostatic interactions. The computation of the electrostatic interaction is the most expensive portion of a molecular simulations. Due to this, there have been significant efforts to develop practical, efficient, and accurate methods for electrostatic interactions.

The Ewald method is one of the most well known and accurate methods but is computationally expensive, scaling as $O(N^2)$, where N is the total number of particles. The appropriate selection of a damping parameter and suitable algorithm can decrease computational cost to $O(N^{3/2})$. [4] Modified Ewald methods, using a particle mesh and fast Fourier transform (FFT), have decreased the cost to $O(N \log N)$. [5–8] But these modified Ewald methods (particle mesh Ewald (PME) and particle-particle particle-mesh Ewald (PPPME)) are still computa-

tionally expensive. In addition to this, the Ewald method requires an inherent periodicity which can be problematic in a number of protein/solvent and ionic solution environments. [9–15] To address these problems there is growing interest in the development of efficient real space electrostatic methods which scale linearly with the system size, $O(N)$. Real space methods were originally proposed by Wolf *et al.* [16] and extended initially by Zahn *et al.*[17] then by Fennell and Gezelter. [15] These methods were only limited to charge-charge interactions between atomic sites. My research developed real-space electrostatic interaction methods for higher order multipoles (dipoles and quadrupoles) and implemented these methods as code into OpenMD, [18] an open source C++-based software. We also studied applications and performance of these methods in the various condensed phase environments. In addition our research also evaluated various static, dynamic, and dielectric properties for different molecular systems, using newly developed real space methods and compared our results with the well-known Ewald method.

This dissertation consists of five chapters. This introductory chapter initially outlines the background and motivation of the research. It also briefly discusses the basic principles of widely used molecular simulation methods: Molecular Dynamics (MD) and Monte Carlo (MC) simulations, where newly developed electrostatic methods are very useful. Similarly, this chapter describes periodic boundary conditions (PBC) and spherical truncation which are both widely incorporated in molecular simulations for computational efficiency. Additionally it also discusses the traditional Ewald as well as various modified Ewald-based methods, PPPME and PME. Finally it discusses the problems created due to the direct spherical truncation in real-space methods and presents various techniques implemented to

resolve these problems.

Chapter 2 presents the mathematical formulation of our newly developed real-space electrostatic methods: Gradient Shifted Force (GSF), Shifted Potential (SP), and Taylor Shifted force (TSF). The energy constants for different dipolar and quadrupolar crystals were evaluated using newly developed real-space methods and compared with analytical results.

The accuracy of the newly developed methods tested against Ewald in Chapter 3. Furthermore various static and dynamic properties evaluated from real space methods are also compared with traditional Ewald method. The study of total energy conservation, which is very important in MD simulations, is also presented in this chapter.

Chapter 4 describes Fluctuation, Perturbation, and Potential of Mean Force (PMF) methods for evaluating dielectric properties for dipolar and quadrupolar fluids. This chapter also explores the correction factor required to obtain actual dielectric properties using SP, GSF, and TSF methods. In addition, the dielectric properties such as susceptibility and dielectric constant, obtained using all three methods are compared with each other as well as with previous simulations.

Finally Chapter 5 summarizes, draws conclusions and discusses future directions and limitations of this research.

1.1 Molecular Dynamics (MD) Simulations

Molecular dynamics is a computer simulation method for studying static and dynamic properties of molecular systems. In this method, each atom or molecule interacts with all other molecules in the system and evolves dynamically following classical equation of motion. The numerical step-by-step process for MD is

outlined in Fig. 1.1.

In a MD simulation, all molecules are initialized by assigning their initial positions and velocities using appropriate boundary conditions. Molecules are usually initialized in such a way so that system does not take too long time to reach equilibrium. Before moving a molecule in the system, the computer must evaluate force and the potential energy contributed by intramolecular interactions as well as intermolecular interactions. The potential energy of the molecule in the system can be written as:

$$U(\mathbf{r}) = \overbrace{U_{bond} + U_{bend} + U_{torsion}}^{\text{Intramolecular interactions}} + \overbrace{U_{electrostatic} + U_{van\ der\ Waals} + \dots}^{\text{Intermolecular interactions}} \quad (1.1)$$

The force and torque acting on the molecule can be calculated using following equations:

$$\mathbf{F} = \nabla_r U(\mathbf{r}, \hat{u}) \quad (1.2a)$$

$$\boldsymbol{\tau} = \mathbf{r} \times \nabla_r U(\mathbf{r}, \hat{u}), \quad (1.2b)$$

where \hat{u} is the orientation of the molecule and the evaluation of force and torque depends on the direction of orientation for the point multipoles. The force and torque are required to propagate the dynamics to the molecule at a given time step. The same process can be repeated for every molecule in the system. Once every molecule in the system is moved forward a time-step, their positions and velocities are adjusted according to applied boundary conditions (i.e temperature, pressure, volume, etc are adjusted). After adjusting positions and velocities, we can recalculate the potential energy for each molecule and repeat same process

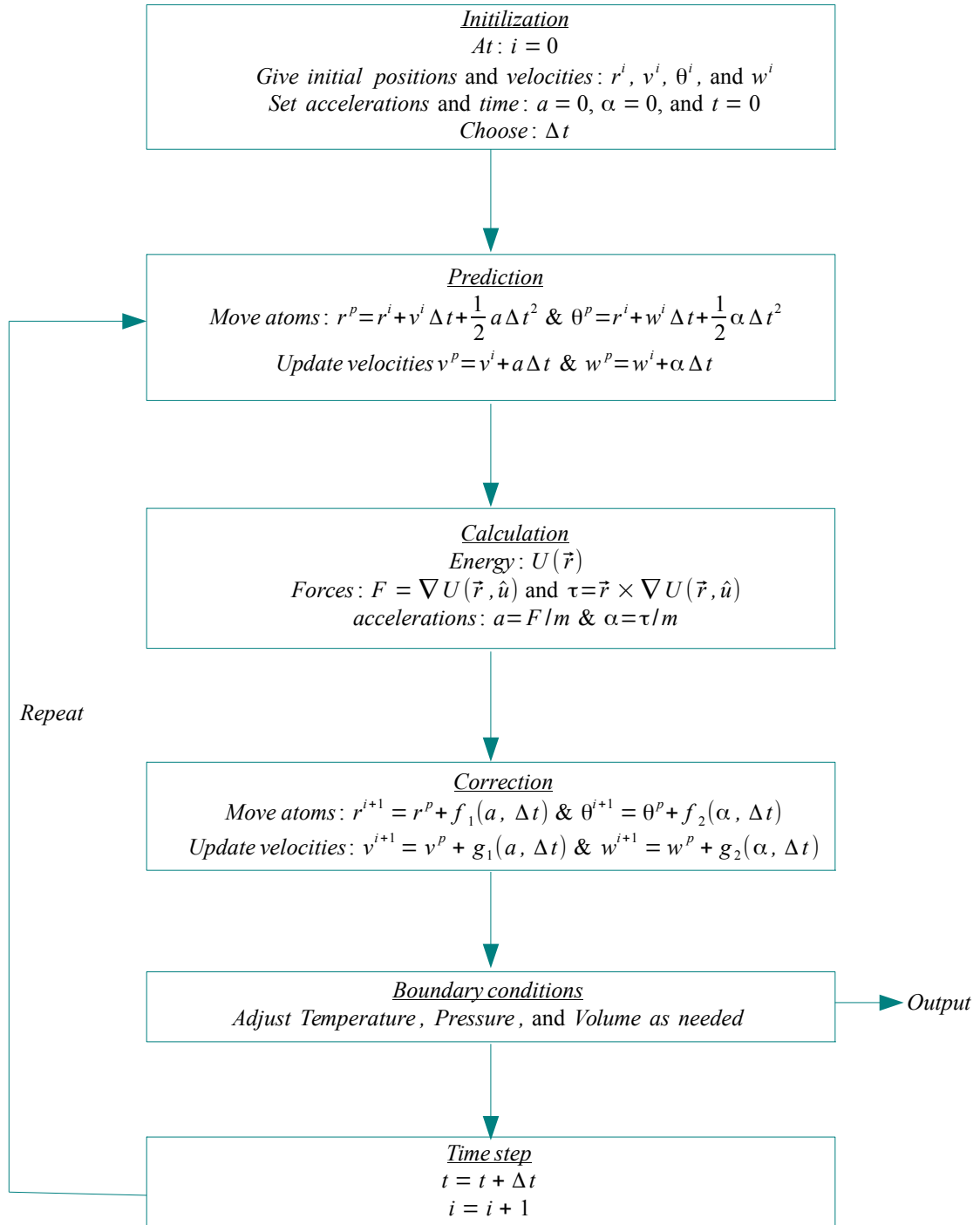


Figure 1.1. Schematic figure showing the step-by-step process in Molecular dynamics simulation.

until the simulation completes the allowed simulation time.

In MD simulations, the intermolecular interactions are the most expensive part of simulation. Among them, the van der Waals interactions are short-range interactions and are often described by Lennard-Jones (LJ) potential:

$$U_{LJ}(r) = 4\epsilon \left[\left(\frac{\sigma}{r} \right)^{12} - \left(\frac{\sigma}{r} \right)^6 \right], \quad (1.3)$$

where σ is diameter of a molecule and ϵ determines well depth of the attractive potential. The $1/r^6$ in the Eq. (1.3) is short-ranged. The $1/r^{12}$ repulsive part of the LJ potential prevents two or more molecules from occupying the same position. The electrostatic interactions are considered long-range interactions e.g. charge-charge interactions between molecules can be described by Coulomb's law:

$$U_{electrostatic}(r) = \frac{1}{4\pi\epsilon_o} \frac{q_1 q_2}{r}. \quad (1.4)$$

Electrostatic interactions decay much slower with the distance. For charge-charge, they fall off as $\frac{1}{r}$. If the lowest order moment in the molecule is a dipole, the electrostatic interaction will fall off by $1/r^3$. Even if the lowest order moment in molecule is a quadrupole, the electrostatic interaction will decay by $1/r^5$ which is longer range than LJ interaction. Since the electrostatic interaction decays slowly, we need to consider a large number of molecules around it to capture physical behavior due to interactions. Consideration of interactions with large number of molecules is not computationally efficient. The most important challenge in the molecular dynamics communities have been to capture right electrostatic behavior of a molecule considering only its interaction with a small number of neighboring molecules. There have been many efforts to develop efficient and accurate algorithms to evaluate electrostatic interaction in molecular simulation, which will be

discussed in detail in section 1.3.

1.1.1 Periodic Boundary Condition (PBC)

Real liquid systems consist of very large number of molecules. But for computational efficiency, only a small number of particles ($\sim 10^3$) are usually considered in molecular simulations. On the other hand, if we want to study and predict bulk properties of the material using small number of molecules, a large fraction of molecules will be near the edge of the sample, contributing a huge surface effect. To eliminate surface effects, Periodic Boundary Conditions (PBC) have long been employed in various molecular simulations.[19] In PBC, the simulation box is replicated throughout the space to form an infinite lattice. In the course of simulation, if a molecule moves in the central box, its images in replicated boxes will also move in the similar fashion. Similarly when a molecule leaves the central box, one of its images will enter the box through opposite face to conserve total number of particle in a central box (see Fig. 1.2). Therefore the system acts like there is no wall at the boundary of the central box and eliminates the surface effect in the computation. If we want to evaluate potential energy of a molecule, we can consider its interactions with nearest molecules or images using the minimum image convention.[20] Even for minimum image convention, we need to calculate large number of pairwise distances at every time step. Consider a system of N molecules, the potential energy of i^{th} molecule we need to find its distances r_{ij} with every j^{th} molecules or images in the system. Therefore in total we need to calculate $\frac{1}{2}N(N - 1)$ number of distinct distances at every time-step, which can make the computation very expensive.

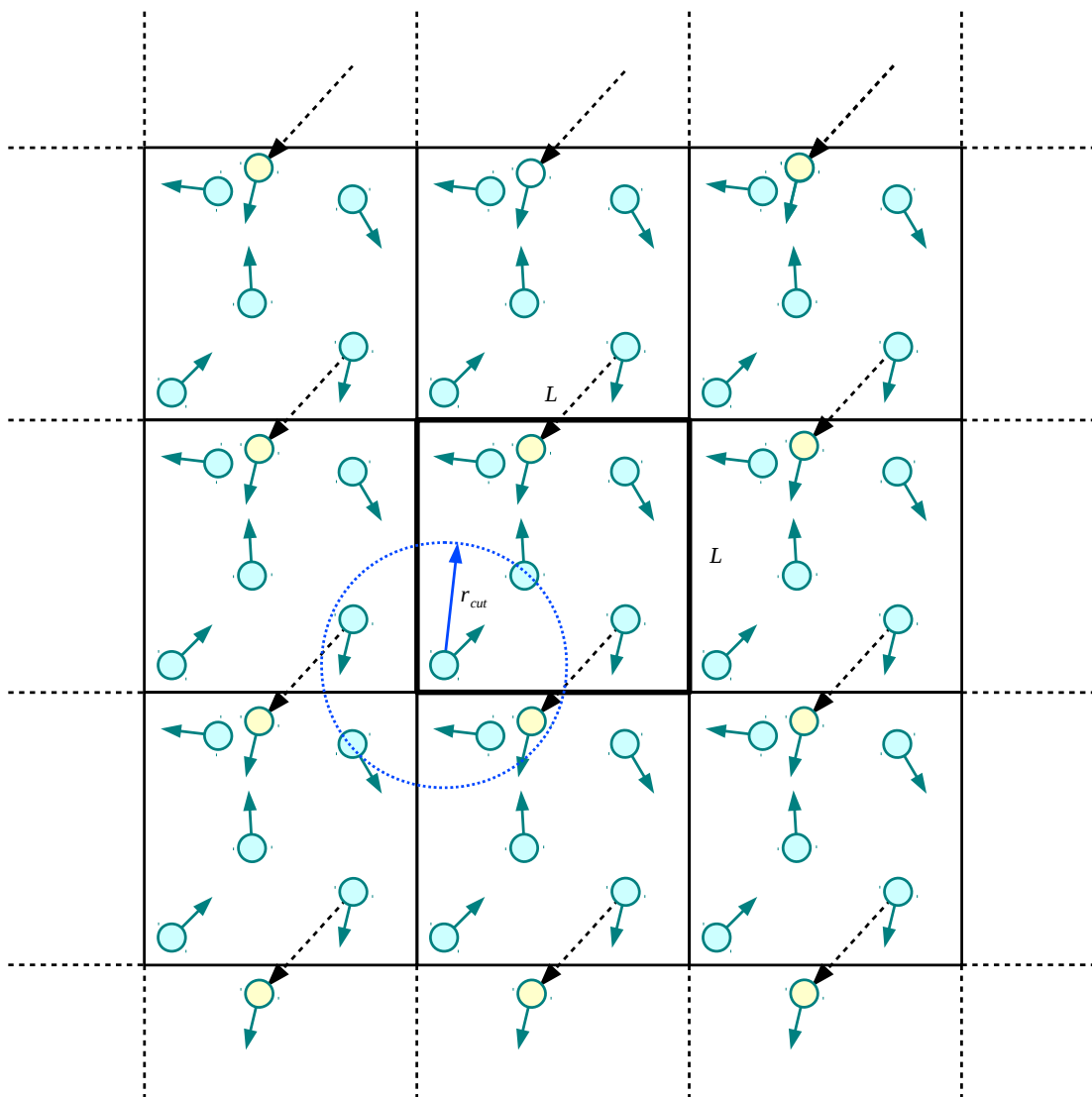


Figure 1.2. Periodic Boundary Condition for two dimensional (2D) molecular system. The central box is outlined using thicker line and replicated throughout the plane to form a 2D lattice. Usually in molecular simulations, the potential energy of the molecule is evaluated considering its interactions with the molecules or their images located in the spherical cutoff region as shown in blue dotted-circle.

1.1.2 Spherical truncation and Neighbor lists

If we assume the interaction between molecules is short-ranged, we can select small region around the molecule and consider that molecule only interacts with other molecules within that region. Often simulations use small cutoff regions around the molecule in order to make the MD simulation efficient. Beyond the cutoff region there is no interaction between the molecules. Consider a system of N molecules with box size L . If PBC is employed, r_{cut} should be less than $L/2$ in the molecular simulation. If $r_{cut} > L/2$, a molecule may interact with another molecule as well as its own image at the same time, which can lead to spurious correlations in molecular dynamics simulation. The spherical truncation implemented in PBC is shown in Fig. 1.2.

But evaluating all pair distances r_{ij} at every time step for determining whether or not a particular molecule is within cutoff region makes simulation computationally expensive. Therefore cutoff sphere r_{cut} is surrounded by the another larger sphere of radius r_{list} as shown in Fig. 1.3. At the beginning of the simulation a list of the molecules, the neighbour list, is constructed around each molecule. For a few time steps, only the molecules in the neighbour list are selected to check whether or not molecule is within the cutoff sphere. After a few time steps, the neighbour list is reconstructed by evaluating pair distances between every molecules. This reconstruction time is mainly determined by the dynamics of the molecules in the simulation.

1.2 Monte Carlo (MC) Simulation

We need to sample a large number of different configurations to study any physical and statistical properties of the system. These configurations must take into

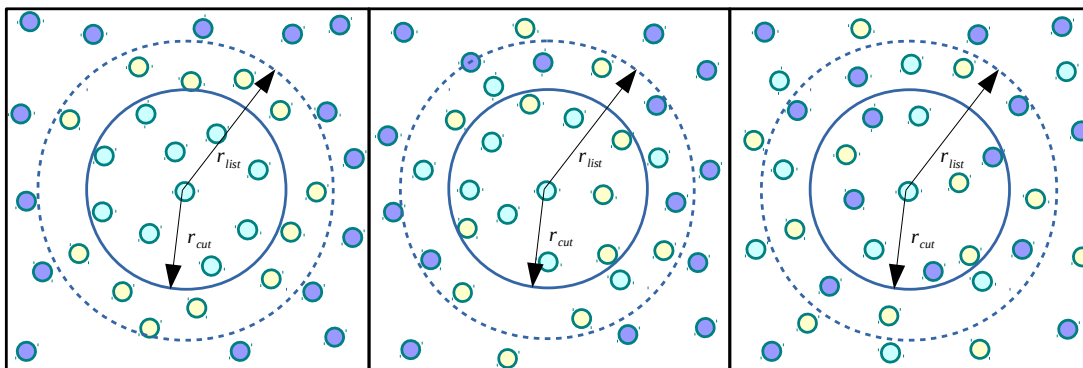


Figure 1.3. Region of neighbor list around the cutoff sphere. Molecules in the cutoff region, neighbour list, and outer region are indicated by green, yellow, and violet circles respectively. The neighbour list should be reconstructed before molecules in the outer region starts to penetrate the cutoff region.

account the ensemble being simulated. The Monte Carlo method uses probabilistic sampling of the system to generate representative configurations of the system. Each configuration depends only upon its predecessor but does not depend on the all the other configurations that were visited previously. For a canonical system, the probability of obtaining a given configuration is given by Boltzmann factor, $\exp(-\Delta E/k_B T)$. Metropolis *et.al* developed the selection criteria for acceptance of the subsequent configuration of the system. [21] According to their method, the new configuration of the system is accepted either $\Delta E < 0$ or $e^{-\frac{\Delta E}{k_B T}} > r$, where r is the random number between 0 and 1. The evaluation of the potential energy difference between subsequent configurations, ΔE , is very important in the MC simulation. For computational efficiency, this method also utilizes cutoff region r_{cut} as well as periodic boundary condition to calculate electrostatic interaction. Therefore developing an efficient and accurate electrostatic interaction method has always been subject of interest in the MC community.

1.3 Electrostatic Methods

Consider a system of N particles in a cubic box of length L replicated infinitely in 3D-space. The electrostatic potential energy for a particle with charge q_i and position \mathbf{r}_i is given by

$$U_i = \sum_n' \sum_{j=1}^N \frac{q_i q_j}{|\mathbf{r}_i - \mathbf{r}_j + \mathbf{n}L|}, \quad (1.5)$$

where q_j represents all other charges located at position \mathbf{r}_j or in periodic replica and \mathbf{n} is the cell-coordinate vector, $\mathbf{n}L = n_1 L \hat{x} + n_2 L \hat{y} + n_3 L \hat{z}$, where integers n_1, n_2 , and n_3 number cells along the x , y , and z directions and vary from 0 to ∞ . The prime in the first sum indicates that $i = j$ should be ignored for the central box, i.e. $n = 0$. The factor $1/(4\pi\epsilon_o)$ has been dropped in the Eq. (1.5) for simplicity. The total potential energy of the system can be calculated as,

$$U = \sum_{\substack{i=1 \\ i \neq j}}^N U_i = \frac{1}{2} \sum_n' \sum_{i=1}^N \sum_{j=1}^N \frac{q_i q_j}{|\mathbf{r}_i - \mathbf{r}_j + \mathbf{n}L|}, \quad (1.6)$$

where factor of $1/2$ in the second part of the Eq. (1.6) is due to removal $i \neq j$ in the summation.

As we know the electrostatic interaction is a long-range interaction which is time consuming. On the other hand the potential energy evaluated using Eq. (1.5) converges conditionally to the correct value depending on the order of summation taken into account during calculation.[22] Therefore there have been many efforts to reduce computational cost and remove its conditionally convergent behavior.

1.3.1 Ewald Method

The Ewald method was originally proposed by Ewald in 1921 to evaluate electrostatic interactions in PBC. In this method, the electrostatic interaction can be divided into two rapidly converging real and reciprocal space sums as well as a constant self-term. [23] Since $\text{erf}(x) + \text{erfc}(x) = 1$ we can write Eq. (1.6) as,

$$U = \frac{1}{2} \sum_n' \sum_{i=1}^N \sum_{j=1}^N q_i q_j \frac{\text{erfc}(\alpha r_{ij,n}) + \text{erf}(\alpha r_{ij,n})}{r_{ij,n}}. \quad (1.7)$$

The real-space term 1.8a in Ewald method is obtained by taking complementary error function term in the Eq. (1.7). Similarly reciprocal-space part 1.8b can be obtained by taking Fourier transform of the error function term in Eq. (1.7). The self-term present in the equation removes artificial interactions of the charge with its own images located in the periodic replicas.

$$U_{real} = \frac{1}{2} \sum_{i,j}^N \sum_n' q_i q_j \frac{\text{erfc}(\alpha r_{ij,n})}{r_{ij,n}}, \quad (1.8a)$$

$$U_{reciprocal} = \frac{1}{2\pi V} \sum_{i,j}^N \sum_{\mathbf{m} \neq 0} \frac{\exp(-(\pi \mathbf{m}/\alpha)^2 + 2\pi i \mathbf{m} \cdot \mathbf{r}_{ij})}{\mathbf{m}^2}, \quad (1.8b)$$

$$U_{self} = -\frac{\alpha}{\sqrt{\pi}} \sum_{i=1}^N q_i^2, \quad (1.8c)$$

where V is the volume of the simulation box, \mathbf{m} is a reciprocal-space vector, and α is a damping parameter which determines the rate of convergence in the real and reciprocal space.

Physically each point charge in the system can be assumed to be surrounded by a Gaussian distribution of equal magnitude but oppositely-signed charge (see

Fig. 1.4) with density,

$$\rho_i(r) = q_i \left(\frac{\alpha}{\sqrt{\pi}} \right)^3 \exp(-\alpha^2 r^2), \quad (1.9)$$

where α is a damping parameter determines the distribution of the charge, and r is the distance from the center of distribution. The imposed charge distribution around a charge screens the interactions between the charges making the effective interaction short ranged and therefore converges rapidly with distance. These Gaussian distributions are counteracted by other Gaussian distributions of charge having same magnitude but opposite sign as shown in Fig. 1.4. [23] The sum of potential energy due to second type of charge distributions converges in reciprocal space.

In the minimum image convention scheme, each particle can interact with its nearest particles or their image, the total number of interactions is $\frac{1}{2}N(N-1)$ in Ewald method. Therefore the algorithmic complexity for the Ewald method is $O(N^2)$. Recerz and Jacobs suggested that by choosing proper simulation parameters and minimum image convention schemes we can make reciprocal potential very small as compared to real-space potential so that can be ignored.[24] However this method is only applicable for a larger system but contribution of the reciprocal-space sum might not small for all systems, therefore is not recommended for general MD simulations. Perram *et al.* subdivided each simulation box into $m \times m \times m$ sub-boxes and selected damping parameter $\alpha = m\sqrt{-\log(\delta)}$, where δ is the relative error constant for neglecting the maximum term in the real-space sum, and using this technique they were able to reduce computational time to $O(N^{3/2})$.

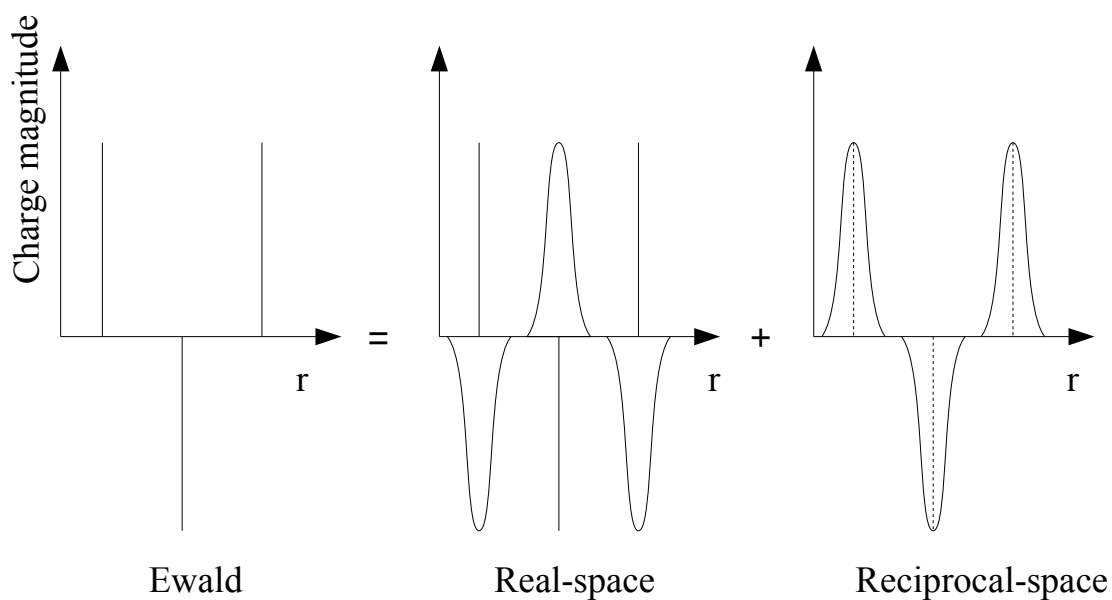


Figure 1.4. In the Ewald method each point charge is surrounded by a Gaussian distribution of equal and oppositely-signed charge, evaluated in real-space. These Gaussian distributions are compensated by the opposite-signed Gaussian distribution of the charges calculated in reciprocal-space

1.3.2 Fourier-based Ewald Methods

The Ewald method has been further modified using Fast Fourier transforms (FFT) to reduce complexity to $O(N \log(N))$. In these methods, charges are interpolated onto a 3D grid and the reciprocal sum is evaluated using FFTs. The particle-particle particle-mesh Ewald (PPPME) and particle-mesh Ewald (PME) methods are two widely-used Fourier-based Ewald methods.

1.3.2.1 Particle-Particle Particle-Mesh Ewald (PPPME)

The PPPME method was originally developed by Hockmney and Eastwood [25] and extended by Luty *et al.* [26] and Rajagopal *et al.* [27]. In this method, the electrostatic interaction is divided into short-ranged real-space and long-ranged reciprocal-space sums. The charges in the system are approximated as uniformly decreasing spherical charge density. The short-ranged potential within the cutoff radius $r < r_{cut}$ is calculated using electrostatic interactions between charge distributions. To calculate the long-ranged potential, first of all charges are assigned to the 3D grid as shown in Fig. 1.5 and transformed to the Fourier space for evaluating electrostatic potential. Since charges are assigned to the grid, it is very efficient to calculate electrostatic interactions in reciprocal space. Once the potential energy is evaluated, an inverse Fourier transformation is applied to calculate energy in real-space and it is numerically differentiated to get the force acting on the grid. Finally the electrostatic force (or energy) can be interpolated from the grid onto the particle locations to obtain actual force acting on the particle.

Although PPPME has complexity of $O(N \log N)$, for computational accuracy, we either need to refine the mesh or use better interpolation techniques, both of which are computationally expensive. In addition to this, using numerical differ-

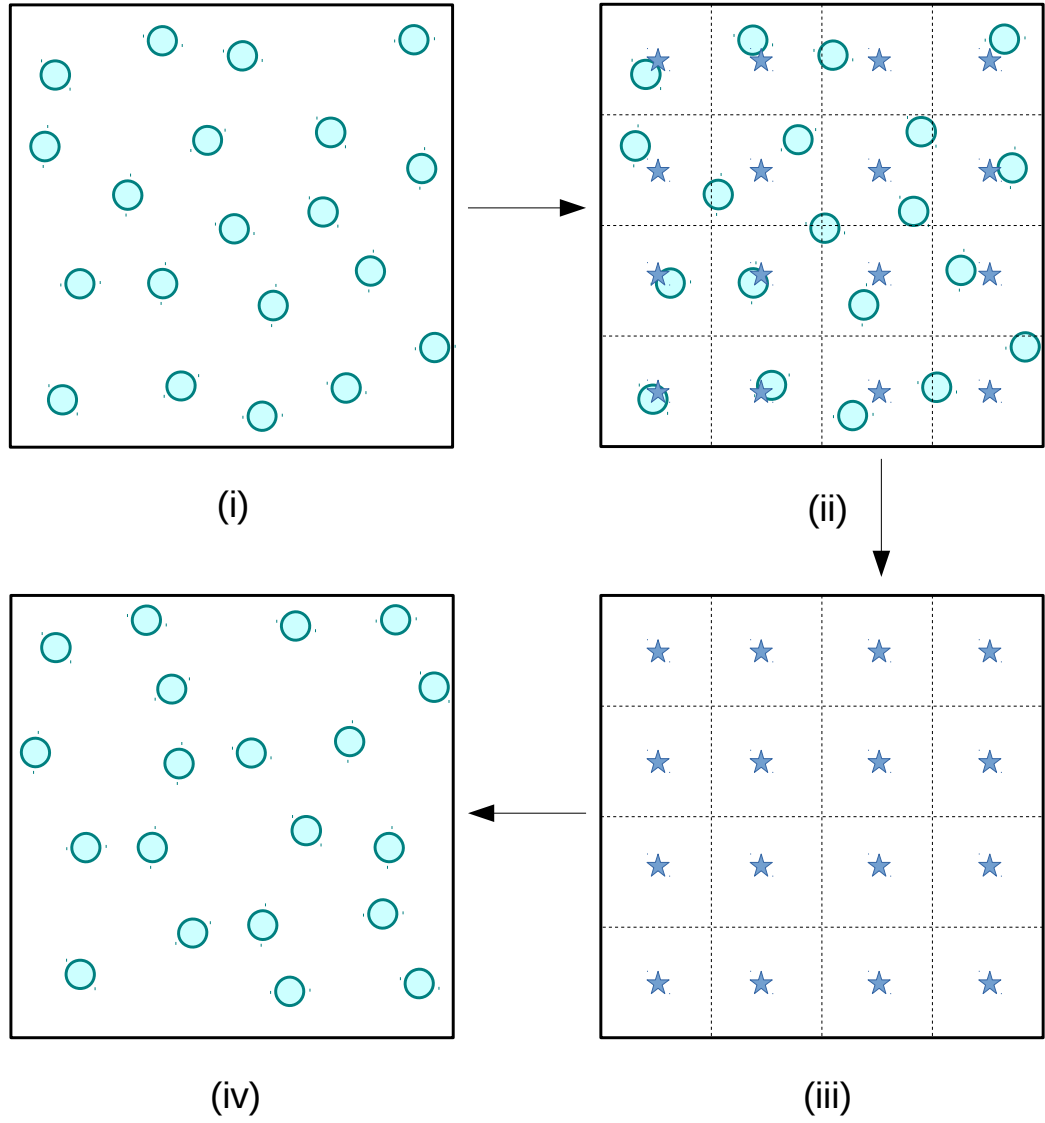


Figure 1.5. Schematic diagram for Fourier-based Ewald methods where green circle represents charge and blue star denotes grid point. In the Figs., (i) a system of charges, (ii) charges mapped with grid points, (iii) force evaluated at the grid points, and (iv) force mapped back to the particles and their positions and velocities are updated.

entiation to calculate forces may introduce errors in the calculation. Therefore higher order differentiation schemes are often used in force calculations. In order to get optimal performance, all of the parameters; charge-distribution, interpolation technique, and differentiation schemes must be properly selected for a given system making parameter choices system specific. [23]

1.3.2.2 Particle-Mesh Ewald (PME)

This method is the modification of the PPPME method, in which the potential energy is divided into real-space and reciprocal-space sums. The charge is represented by the Gaussian distributions of charge. In this method, the real-space sum within the cutoff sphere is evaluated using actual electrostatic interactions between charges whereas the reciprocal sum is calculated in Fourier space using the idea of 3D grid as explained in the PPPME method. Unlike PPPME, this method evaluates force analytically, differentiating electrostatic energy at a given grid point reducing memory requirement significantly. This method also has $O(N\log N)$ algorithmic complexity and uses interpolation to map back electrostatic force from grid to the particle's location. Therefore users of this method need to discover optimal interpolation schemes to obtain excellent speed and accuracy for a simulation, making this method system dependent.

1.3.3 Real Space Methods

Before discussing the real space methods, the fundamental property of the electrostatic interactions in condensed phase environments should be considered. The electrostatic interaction between two charged particles decays as $1/r$. But molecular systems are usually composed of an equal number of positive and neg-

ative charges. Thus the range of interaction between a particular charge and rest of the charges in the system are different than the interaction between two bare charges. Consider a one dimensional (1D) crystal lattice composed of positive and negative charges. The potential energy of a particular ion can be considered as a sum of interactions with positive and negative ion pairs as shown in Fig. 4.1(a). Mathematically the potential energy for 1D crystal with alternating charges is given by a Madelung sum,

$$\begin{aligned}
U^{Mad} &= -2q_i q_j \left(\frac{1}{a} - \frac{1}{2a} \right) - 2q_i q_j \left(\frac{1}{3a} - \frac{1}{4a} \right) - 2q_i q_j \left(\frac{1}{5a} - \frac{1}{6a} \right) + \dots \\
&= - \left(\frac{2q_i q_j}{(1.414)^2 a} \right) - \left(\frac{2q_i q_j}{(3.464)^2 a} \right) - \left(\frac{2q_i q_j}{(5.477)^2 a} \right) + \dots
\end{aligned} \tag{1.10}$$

If we consider all 3 terms in the Eq. (1.10) and compare their distances with the distance between central ion and group of ions as shown in Fig. 4.1(a), we clearly see that the interaction energy of a single ion with the pairs converges faster than $(1/r)$. Similarly, in a two dimensional (2D) lattice, the potential energy of an ion can be described as a sum of positive and negative four body groups as seen in Fig. 4.1(b). The interaction energy between an ion and group of four ions decays much faster than the charge-charge interaction. For a three-dimensional (3D) crystal, the potential energy of an ion can be considered as due to its interaction with the group of eight ions forming a cube. From this generalization, we can conclude that the electrostatic interaction energy for an ion in the crystalline system is a short-ranged as compared to charge-charge interaction. Therefore, even the relatively small systems should be able to represent bulk long-ranged interactions.

In order to reduce the computational expense of a molecular dynamics sim-

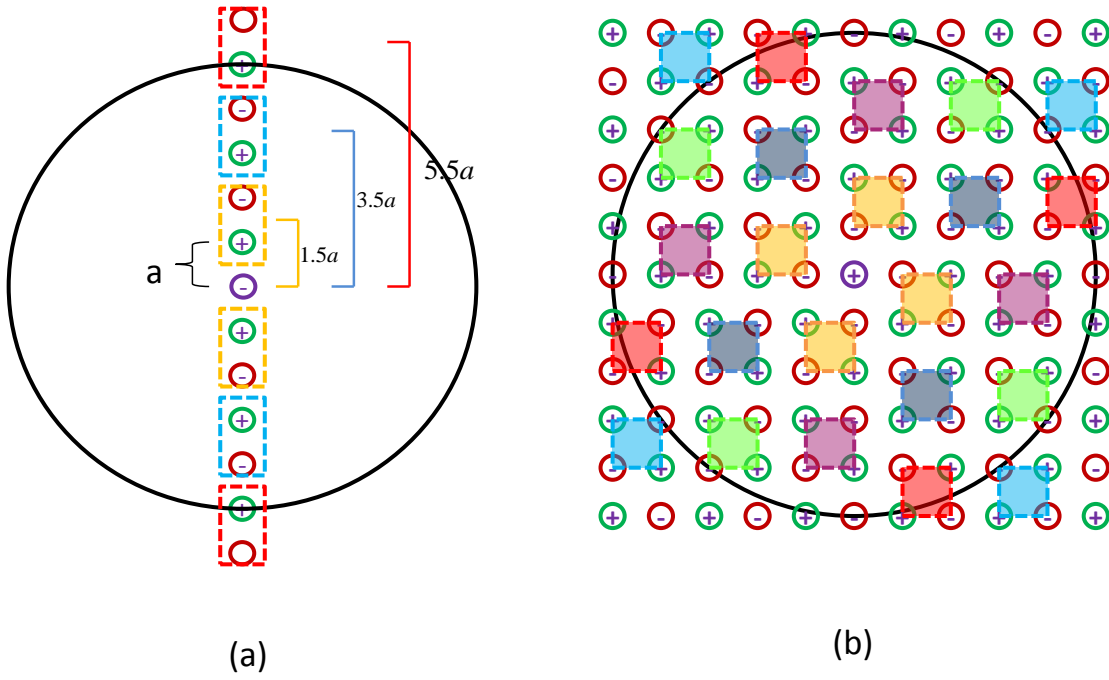


Figure 1.6. Schematic diagram showing grouping of ions in (a) 1D (b) 2D crystals. The interaction of the central ion with the group of ions decays faster than $1/r$. The direct spherical truncation breaks the ordering of the ions at the cut off sphere providing a net charge within the cutoff sphere. The breaking of the charge ordering increases with the crystal dimension resulting in a large net charge in the higher dimensional crystal.

ulation, interactions between particles are only considered if the particles exist within a cutoff distance r_c , of one another. We first consider how the energy of a system behaves if we truncate the interactions at the cutoff radius. Fig. 1.7 shows (black line) that the electrostatic potential energy does not converge to the Madelung energy upon increasing the cutoff radius for the direct truncation. On the other hand the energy is found to be closer to the Madelung constant when the net charge within the cutoff radius is zero (Fig. 1.8). This oscillation in the potential energy is due to the breaking in charge ordering on the surface of the cutoff sphere which results in a net charge within the cutoff sphere. The size of the net charge is proportional to the dimension of the crystal. Although the interaction energy is short ranged, the direct truncation results in severe oscillation in energy for 3D crystal as shown in Fig. 1.7. Dipolar (or quadrupolar) crystals are also formed by ordering of the dipolar (or quadrupolar) molecules. Therefore similar oscillatory behaviour in the potential energy is due to the breaking of the ordering of dipoles (or quadrupoles) on the surface of the truncated sphere. Even in liquids there is local ordering of the molecules due to electrostatic interaction and similar oscillatory behaviour in the electrostatic potential has been seen in direct truncation approaches.

Wolf *et al* [16] proposed the idea of placing an image charge on the surface of cutoff sphere for every charge found within the sphere. The image charges should have opposite charge of those found within the sphere guaranteeing charge neutralization within the cutoff sphere.[16] This charge neutralization converges the potential energy to the correct Madelung energy as shown in Fig. 1.7 (orange line). In molecular dynamics (MD) simulations, the energy, force and torque should approach zero as the distance between molecules approaches the cutoff ra-

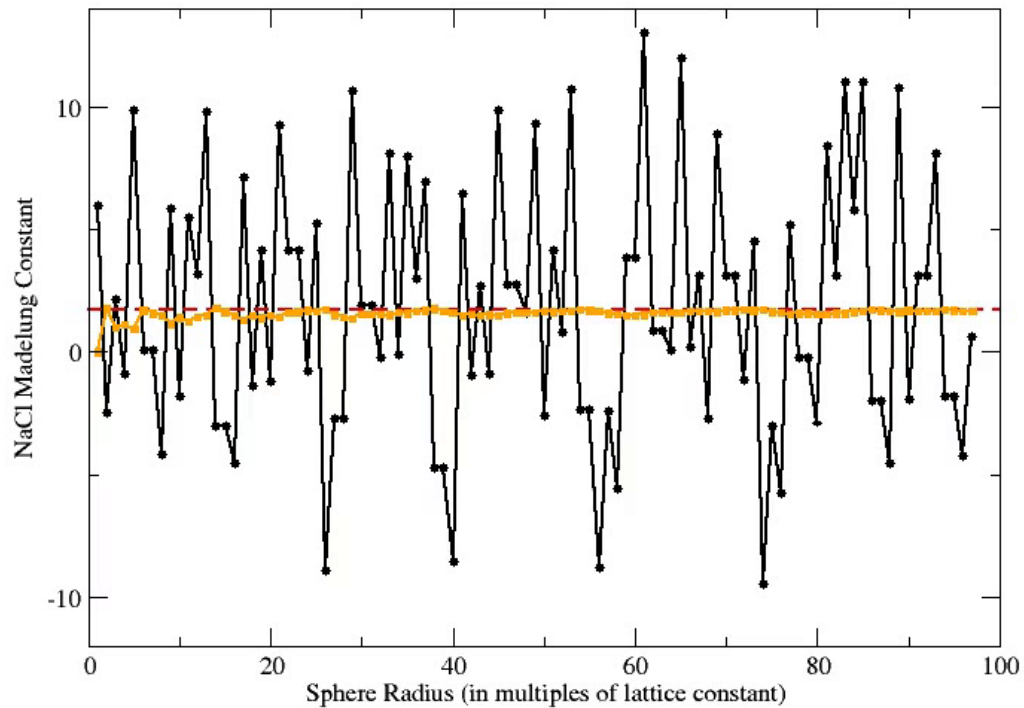


Figure 1.7. Convergence of the lattice energy constants for a 3D NaCl crystal as a function of cutoff radius for the direct (hard) cutoff method (black line). The orange line in the figure is for charge neutralized cutoff sphere (when image charge placed on the surface of the cutoff sphere). The red dotted line represents Madelung energy for NaCl crystal

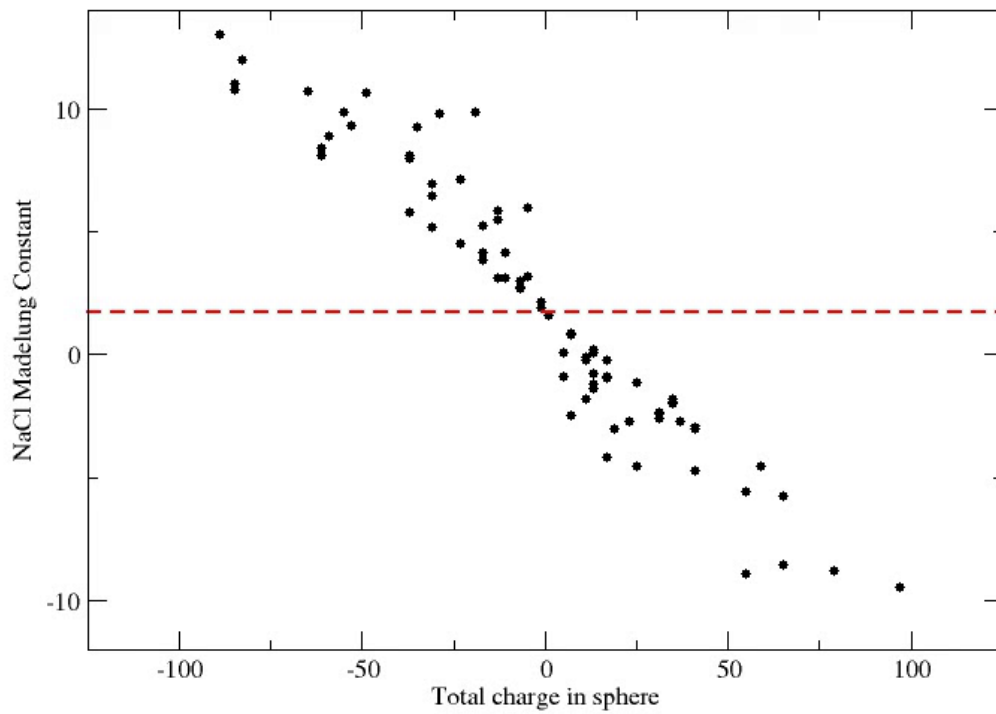


Figure 1.8. Convergence of the lattice energy constants for the NaCl crystal as a function of net charge within a cutoff sphere. The red dotted line represents Madelung energy for NaCl crystal

dus in order to conserve total energy. However Wolf's forces and torques derived from the potential do not go to zero at the cutoff radius, which makes it inappropriate to use in MD simulations. More recently, Zahn *et al.* and Fennell and Gezelter proposed the damped shifted force (DSF) potential, which incorporates Wolf's approach of image charges while ensuring the forces and torques approach zero at the cutoff radius.[15, 17] Fukuda has also recently been successful with the neutralization of higher order moments in a system of point charges.[28]

Real-space methods scale linearly with system size, are system-independent, and applicable a variety of condensed phase environments. Therefore we selected real-space methods for extending to higher-order charge-multipoles. In our research, we have generalized Wolf's shifted potential (SP) to the higher order electrostatic multipoles. We have also developed the gradient shifted force (GSF) and Taylor shifted force (TSF) potentials which are the natural extension of the damped shifted force (DSF) for higher order charge-multipoles. In the following chapter 2, I will discuss the development of the SP, GSF, and TSF methods and evaluate the energy constants for various dipolar and quadrupolar crystals using newly developed methods and compare with analytical results.[29]

CHAPTER 2

DEVELOPMENT OF METHODS

This chapter describes the detailed mathematical development of the three real-space methods: Shifted Potential (SP), Gradient Shifted Force (GSF), and Taylor Shifted Force (TSF) for computing electrostatic interactions between point multipoles in molecular simulations. We generalize Wolf's shifted potential for charge-charge interaction to develop multipolar SP method for dipoles and quadrupoles. We also extend original Damped Shifted Force (DSF) method for charge-charge interaction to develop Gradient Shifted Force (GSF) and Taylor Shifted Force (TSF) methods for higher order multipoles. Finally I report the lattice energy constants for different dipolar and quadrupolar crystals evaluated using the newly developed real-space methods and compare with analytical result.

2.1 Introduction

There has been increasing interest in real-space methods for calculating electrostatic interactions in computer simulations of condensed molecular systems [15–17, 30–37] The simplest of these techniques was developed by Wolf *et al.* in their work towards an $\mathcal{O}(N)$ Coulombic sum.[16] For systems of point charges, Zahn *et al.* extended the Wolf approach by adding a force-shifting term to the enhanced damped Coulomb potential.[17, 30] Fennell and Gezelter showed that the simple

damped shifted force (DSF) potential can give nearly quantitative agreement with smooth particle mesh Ewald (SPME)[8] configurational energy differences as well as atomic force and molecular torque vectors.[15]

The computational efficiency and the accuracy of the DSF method are surprisingly good, particularly for systems with uniform charge density. Additionally, dielectric constants obtained using DSF and similar methods where the force vanishes at r_c are essentially quantitative.[37] The DSF and other related methods have now been widely investigated,[38] and DSF is now used routinely in a diverse set of chemical environments.[39–45] DSF electrostatics provides a compromise between the computational speed of real-space cutoffs and the accuracy of fully-periodic Ewald treatments.

One common feature of many coarse-graining approaches, which treat entire molecular subsystems as a single rigid body, is simplification of the electrostatic interactions between these bodies so that fewer site-site interactions are required to compute configurational energies. To do this, the interactions between coarse-grained sites are typically taken to be point multipoles.[46–48]

Water, in particular, has been modeled recently with point multipoles up to octupolar order.[49–52] For maximum efficiency, these models require the use of an approximate multipole expansion as the exact multipole expansion can become quite expensive (particularly when handled via the Ewald sum).[53] Point multipoles and multipole polarizability have also been utilized in the AMOEBA water model and related force fields.[54–56]

Higher-order multipoles present a peculiar issue for molecular dynamics. Multipolar interactions are inherently short-ranged, and should not need the relatively expensive Ewald treatment. However, real-space cutoff methods are normally ap-

plied in an orientation-blind fashion so multipoles which leave and then re-enter a cutoff sphere in a different orientation can cause energy discontinuities.

This chapter outlines an extension of the original DSF electrostatic kernel to point multipoles. We describe three distinct real-space interaction models for higher-order multipoles based on truncated Taylor expansions that are carried out at the cutoff radius. We are calling these models **Taylor-shifted** (TSF), **gradient-shifted** (GSF) and **shifted potential** (SP) electrostatics. Because of differences in the initial assumptions, the two methods yield related, but distinct expressions for energies, forces, and torques.

In this chapter we outline the new methodology and give functional forms for the energies, forces, and torques up to quadrupole-quadrupole order. We also compare the new methods to analytic energy constants for periodic arrays of point multipoles. In the following chapter, we provide numerical comparisons to Ewald-based electrostatics in common simulation environments.

2.2 Methodology

An efficient real-space electrostatic method involves the use of a pair-wise functional form,

$$U = \sum_i \sum_{j>i} U_{\text{pair}}(\mathbf{r}_{ij}, \mathbf{A}_i, \mathbf{B}_j) + \sum_i U_i^{\text{self}} \quad (2.1)$$

that is short-ranged and easily truncated at a cutoff radius,

$$U_{\text{pair}}(\mathbf{r}_{ij}, \mathbf{A}_i, \mathbf{B}_j) = \begin{cases} U_{\text{approx}}(\mathbf{r}_{ij}, \mathbf{A}_i, \mathbf{B}_j) & |\mathbf{r}_{ij}| \leq r_c \\ 0 & |\mathbf{r}_{ij}| > r_c, \end{cases} \quad (2.2)$$

along with an easily computed self-interaction term ($\sum_i U_i^{\text{self}}$) which scales linearly with the number of particles. Here \mathbf{A}_i and \mathbf{B}_j represent orientational coordinates of the two sites (expressed as rotation matrices), and \mathbf{r}_{ij} is the vector between the two sites. The computational efficiency, energy conservation, and even some physical properties of a simulation can depend dramatically on how the U_{approx} function behaves at the cutoff radius. The goal of any approximation method should be to mimic the real behavior of the electrostatic interactions as closely as possible without sacrificing the near-linear scaling of a cutoff method.

2.2.1 Self-neutralization, damping, and force-shifting

The DSF and Wolf methods operate by neutralizing the total charge contained within the cutoff sphere surrounding each particle. This is accomplished by shifting the potential functions to generate image charges on the surface of the cutoff sphere for each pair interaction computed within r_c . Damping using a complementary error function is applied to the potential to accelerate convergence. The interaction for a pair of charges (C_i and C_j) in the DSF method,

$$U_{\text{DSF}}(r_{ij}) = C_i C_j \left[\frac{\text{erfc}(\alpha r_{ij})}{r_{ij}} - \frac{\text{erfc}(\alpha r_c)}{r_c} + \left(\frac{\text{erfc}(\alpha r_c)}{r_c^2} + \frac{2\alpha}{\pi^{1/2}} \frac{\exp(-\alpha^2 r_c^2)}{r_c} \right) (r_{ij} - r_c) \right] \quad (2.3)$$

where α is the adjustable damping parameter. Note that in this potential and in all electrostatic quantities that follow, the standard $1/4\pi\epsilon_0$ has been omitted for clarity.

To insure net charge neutrality within each cutoff sphere, an additional “self” term is added to the potential. This term is constant (as long as the charges and

cutoff radius do not change), and exists outside the normal pair-loop for molecular simulations. It can be thought of as a contribution from a charge opposite in sign, but equal in magnitude, to the central charge, which has been spread out over the surface of the cutoff sphere. A portion of the self term is identical to the self term in the Ewald summation, and comes from the utilization of the complimentary error function for electrostatic damping.[16, 57] There have also been recent efforts to extend the Wolf self-neutralization method to zero out the dipole and higher order multipoles contained within the cutoff sphere.[28, 58, 59]

In this work, we extend the idea of self-neutralization for the point multipoles by insuring net charge-neutrality and net-zero moments within each cutoff sphere. In Figure 2.1, point dipole \mathbf{D}_i at the center site i is interacting with point dipole \mathbf{D}_j and point quadrupole \mathbf{Q}_k . The self-neutralization scheme for point multipoles involves projecting opposing multipoles for sites j and k on the surface of the cutoff sphere. There are also significant modifications made to make the forces and torques go smoothly to zero at the cutoff distance.

As in the point-charge approach, there is an additional contribution from self-neutralization of site i . The self term for multipoles is described in section 2.2.9.

2.2.2 The multipole expansion

Consider two discrete rigid collections of point charges, denoted as objects a and b . In the following, we assume that the two objects interact via electrostatics only and describe those interactions in terms of a standard multipole expansion. Putting the origin of the coordinate system at the center of mass of a , we use vectors \mathbf{r}_k to denote the positions of all charges q_k in a . Then the electrostatic

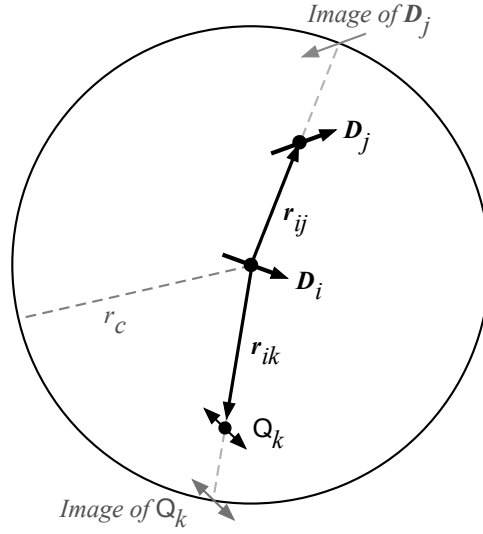


Figure 2.1. Reversed multipoles are projected onto the surface of the cutoff sphere. The forces, torques, and potential are then smoothly shifted to zero as the sites leave the cutoff region.

potential of object a at \mathbf{r} is given by

$$\phi_a(\mathbf{r}) = \sum_{k \text{ in } a} \frac{q_k}{|\mathbf{r} - \mathbf{r}_k|}. \quad (2.4)$$

The Taylor expansion in r can be written using an implied summation notation. Here Greek indices are used to indicate space coordinates (x, y, z) and the subscripts k and j are reserved for labeling specific sites for charges in a and b respectively. The Taylor expansion,

$$\frac{1}{|\mathbf{r} - \mathbf{r}_k|} = \left(1 - r_{k\alpha} \frac{\partial}{\partial r_\alpha} + \frac{1}{2} r_{k\alpha} r_{k\beta} \frac{\partial^2}{\partial r_\alpha \partial r_\beta} + \dots \right) \frac{1}{r}, \quad (2.5)$$

can then be used to express the electrostatic potential on a in terms of multipole operators,

$$\phi_a(\mathbf{r}) = M_a \frac{1}{r} \quad (2.6)$$

where

$$M_a = C_a - D_{a\alpha} \frac{\partial}{\partial r_\alpha} + Q_{a\alpha\beta} \frac{\partial^2}{\partial r_\alpha \partial r_\beta} + \dots \quad (2.7)$$

Here, the point charge, dipole, and quadrupole for object a are given by C_a , \mathbf{D}_a , and \mathbf{Q}_a , respectively. These are the primitive multipoles which can be expressed as a distribution of charges,

$$C_a = \sum_{k \text{ in } a} q_k, \quad (2.8)$$

$$D_{a\alpha} = \sum_{k \text{ in } a} q_k r_{k\alpha}, \quad (2.9)$$

$$Q_{a\alpha\beta} = \frac{1}{2} \sum_{k \text{ in } a} q_k r_{k\alpha} r_{k\beta}. \quad (2.10)$$

Note that the definition of the primitive quadrupole here differs from the standard traceless form, and contains an additional Taylor-series based factor of $1/2$. We are essentially treating the mass distribution with higher priority; the moment of inertia tensor, \mathbf{I} , is diagonalized to obtain body-fixed axes, and the charge distribution may result in a quadrupole tensor that is not necessarily diagonal in the body frame. Additional reasons for utilizing the primitive quadrupole are discussed in section 2.2.3.

It is convenient to locate charges q_j relative to the center of mass of b . Then with \mathbf{r} pointing from the center of mass of a to the center of mass of b ($\mathbf{r} = \mathbf{r}_b - \mathbf{r}_a$),

the interaction energy is given by

$$U_{ab}(r) = M_a \sum_{j \text{ in } b} \frac{q_j}{|\mathbf{r} + \mathbf{r}_j|}. \quad (2.11)$$

This can also be expanded as a Taylor series in r . Using a notation similar to before to define the multipoles in object b ,

$$M_b = C_b + D_{b\alpha} \frac{\partial}{\partial r_\alpha} + Q_{b\alpha\beta} \frac{\partial^2}{\partial r_\alpha \partial r_\beta} + \dots \quad (2.12)$$

we arrive at the multipole expression for the total interaction energy.

$$U_{ab}(r) = M_a M_b \frac{1}{r}. \quad (2.13)$$

This form has the benefit of separating out the energies of interaction into contributions from the charge, dipole, and quadrupole of a interacting with the same types of multipoles in b .

2.2.3 Damped Coulomb interactions

In the standard multipole expansion, one typically uses the bare Coulomb potential, with radial dependence $1/r$, as shown in Eq. (2.13). It is also quite common to use a damped Coulomb interaction, which results from replacing point charges with Gaussian distributions of charge with width α . In damped multipole electrostatics, the kernel $(1/r)$ of the expansion is replaced with the function:

$$B_0(r) = \frac{\text{erfc}(\alpha r)}{r} = \frac{2}{\sqrt{\pi} r} \int_{\alpha r}^{\infty} e^{-s^2} ds. \quad (2.14)$$

We develop equations below using the function $f(r)$ to represent either $1/r$ or $B_0(r)$, and all of the techniques can be applied to bare or damped Coulomb kernels (or any other function) as long as derivatives of these functions are known. Smith's convenient functions $B_l(r)$, which are used for derivatives of the damped kernel, are summarized in Appendix A.1 (N.B. there is one important distinction between the two kernels, which is the behavior of $\nabla^2 \frac{1}{r}$ compared with $\nabla^2 B_0(r)$. The former is zero everywhere except for a delta function evaluated at the origin. The latter also has delta function behavior, but is non-zero for $r \neq 0$. Thus the standard justification for using a traceless quadrupole tensor fails for the damped case.)

The main goal of this work is to smoothly cut off the interaction energy as well as forces and torques as $r \rightarrow r_c$. To describe how this goal may be met, we use two examples, charge-charge and charge-dipole, using the bare Coulomb kernel, $f(r) = 1/r$, to explain the idea.

2.2.4 Shifted-force methods

In the shifted-force approximation, the interaction energy for two charges C_a and C_b separated by a distance r is written:

$$U_{C_a C_b}(r) = C_a C_b \left(\frac{1}{r} - \frac{1}{r_c} + (r - r_c) \frac{1}{r_c^2} \right). \quad (2.15)$$

Two shifting terms appear in this equations, one from the neutralization procedure ($-1/r_c$), and one that causes the first derivative to vanish at the cutoff radius.

Since one derivative of the interaction energy is needed for the force, the minimal perturbation is a term linear in $(r - r_c)$ in the interaction energy, that is:

$$\frac{d}{dr} \left(\frac{1}{r} - \frac{1}{r_c} + (r - r_c) \frac{1}{r_c^2} \right) = \left(-\frac{1}{r^2} + \frac{1}{r_c^2} \right). \quad (2.16)$$

which clearly vanishes as the r approaches the cutoff radius. There are a number of ways to generalize this derivative shift for higher-order multipoles. Below, we present two methods, one based on higher-order Taylor series for r near r_c , and the other based on linear shift of the kernel gradients at the cutoff itself.

2.2.5 Taylor-shifted force (TSF) electrostatics

In the Taylor-shifted force (TSF) method, the procedure that we follow is based on a Taylor expansion containing the same number of derivatives required for each force term to vanish at the cutoff. For example, the quadrupole-quadrupole interaction energy requires four derivatives of the kernel, and the force requires one additional derivative. For quadrupole-quadrupole interactions, we therefore require shifted energy expressions that include up to $(r - r_c)^5$ so that all energies, forces, and torques are zero as $r \rightarrow r_c$. In each case, we subtract off a function $f_n^{\text{shift}}(r)$ from the kernel $f(r) = 1/r$. The subscript n indicates the number of derivatives to be taken when deriving a given multipole energy. We choose a function with guaranteed smooth derivatives – a truncated Taylor series of the function $f(r)$, e.g.,

$$f_n^{\text{shift}}(r) = \sum_{m=0}^{n+1} \frac{(r - r_c)^m}{m!} f^{(m)}(r_c). \quad (2.17)$$

The combination of $f(r)$ with the shifted function is denoted $f_n(r) = f(r) - f_n^{\text{shift}}(r)$. Thus, for $f(r) = 1/r$, we find

$$f_1(r) = \frac{1}{r} - \frac{1}{r_c} + (r - r_c) \frac{1}{r_c^2} - \frac{(r - r_c)^2}{r_c^3}. \quad (2.18)$$

Continuing with the example of a charge a interacting with a dipole b , we write

$$U_{C_a \mathbf{D}_b}(r) = C_a D_{b\alpha} \frac{\partial f_1(r)}{\partial r_\alpha} = C_a D_{b\alpha} \frac{r_\alpha}{r} \frac{\partial f_1(r)}{\partial r}. \quad (2.19)$$

The force that dipole b exerts on charge a is

$$F_{C_a \mathbf{D}_b \beta} = C_a D_{b\alpha} \left[\frac{\delta_{\alpha\beta}}{r} \frac{\partial}{\partial r} + \frac{r_\alpha r_\beta}{r^2} \left(-\frac{1}{r} \frac{\partial}{\partial r} + \frac{\partial^2}{\partial r^2} \right) \right] f_1(r). \quad (2.20)$$

For undamped coulombic interactions, $f(r) = 1/r$, we find

$$F_{C_a \mathbf{D}_b \beta} = \frac{C_a D_{b\beta}}{r} \left[-\frac{1}{r^2} + \frac{1}{r_c^2} - \frac{2(r - r_c)}{r_c^3} \right] + C_a D_{b\alpha} r_\alpha r_\beta \left[\frac{3}{r^5} - \frac{3}{r^3 r_c^2} \right]. \quad (2.21)$$

This expansion shows the expected $1/r^3$ dependence of the force.

In general, we can write

$$U^{\text{TSF}} = (\text{prefactor})(\text{derivatives})f_n(r) \quad (2.22)$$

with $n = 0$ for charge-charge, $n = 1$ for charge-dipole, $n = 2$ for charge-quadrupole and dipole-dipole, $n = 3$ for dipole-quadrupole, and $n = 4$ for quadrupole-quadrupole. For example, in quadrupole-quadrupole interactions for which the prefactor is $Q_{a\alpha\beta}Q_{b\gamma\delta}$, the derivatives are $\partial^4/\partial r_\alpha \partial r_\beta \partial r_\gamma \partial r_\delta$, with implied summation combining the space indices. Appendix A.2 contains details on the radial functions.

In the formulas presented in the tables below, the placeholder function $f(r)$ is used to represent the electrostatic kernel (either damped or undamped). The main functions that go into the force and torque terms, $g_n(r)$, $h_n(r)$, $s_n(r)$, and $t_n(r)$ are successive derivatives of the shifted electrostatic kernel, $f_n(r)$ of the same index

n . The algebra required to evaluate energies, forces and torques is somewhat tedious, so only the final forms are presented in Tables 2.2 and 2.3. One of the principal findings of our work is that the individual orientational contributions to the various multipole-multipole interactions must be treated with distinct radial functions, but each of these contributions is independently force shifted at the cutoff radius.

2.2.6 Gradient-shifted force (GSF) electrostatics

The second, and conceptually simpler approach to force-shifting maintains only the linear $(r - r_c)$ term in the truncated Taylor expansion, and has a similar interaction energy for all multipole orders:

$$U^{\text{GSF}} = \sum [U(\mathbf{r}, \mathbf{A}, \mathbf{B}) - U(r_c \hat{\mathbf{r}}, \mathbf{A}, \mathbf{B}) - (r - r_c) \hat{\mathbf{r}} \cdot \nabla U(r_c \hat{\mathbf{r}}, \mathbf{A}, \mathbf{B})] \quad (2.23)$$

where $\hat{\mathbf{r}}$ is the unit vector pointing between the two multipoles, and the sum describes a separate force-shifting that is applied to each orientational contribution to the energy. Both the potential and the gradient for force shifting are evaluated for an image multipole projected onto the surface of the cutoff sphere (see fig 2.1). The image multipole retains the orientation (rotation matrix \mathbf{B}) of the interacting multipole. No higher order terms $(r - r_c)^n$ appear. The primary difference between the TSF and GSF methods is the stage at which the Taylor Series is applied; in the Taylor-shifted approach, it is applied to the kernel itself. In the Gradient-shifted approach, it is applied to individual radial interaction terms in the multipole expansion. Energies from this method thus have the general form:

$$U = \sum (\text{angular factor})(\text{radial factor}). \quad (2.24)$$

Functional forms for both methods (TSF and GSF) can both be summarized using the form of Eq. (2.24). The basic forms for the energy, force, and torque expressions are tabulated for both shifting approaches below – for each separate orientational contribution, only the radial factors differ between the two methods.

2.2.7 Generalization of the Wolf shifted potential (SP)

It is also possible to formulate an extension of the Wolf approach for multipoles by simply projecting the image multipole onto the surface of the cutoff sphere, and including the interactions with the central multipole and the image. This effectively shifts the pair potential to zero at the cutoff radius,

$$U^{\text{SP}} = \sum [U(\mathbf{r}, \mathbf{A}, \mathbf{B}) - U(r_c \hat{\mathbf{r}}, \mathbf{A}, \mathbf{B})] \quad (2.25)$$

independent of the orientations of the two multipoles. The sum again describes separate potential shifting that is applied to each orientational contribution to the energy.

The shifted potential (SP) method is a simple truncation of the GSF method for each orientational contribution, leaving out the $(r - r_c)$ terms that multiply the gradient. Functional forms for the shifted-potential (SP) method can also be summarized using the form of Eq. 2.24. The energy, force, and torque expressions are tabulated below for all three methods. As in the GSF and TSF methods, for each separate orientational contribution, only the radial factors differ between the SP, GSF, and TSF methods.

2.2.8 Body and space axes

Although objects a and b rotate during a molecular dynamics (MD) simulation, their multipole tensors remain fixed in body-frame coordinates. While deriving force and torque expressions, it is therefore convenient to write the energies, forces, and torques in intermediate forms involving the vectors of the rotation matrices. We denote body axes for objects a and b using unit vectors $\hat{\mathbf{A}}_m$ and $\hat{\mathbf{B}}_m$, respectively, with the index $m = (123)$. In a typical simulation, the initial axes are obtained by diagonalizing the moment of inertia tensors for the objects. (N.B., the body axes are generally *not* the same as those for which the quadrupole moment is diagonal.) The rotation matrices are then propagated during the simulation.

The rotation matrices \mathbf{A} and \mathbf{B} can be expressed using these unit vectors:

$$\mathbf{A} = \begin{pmatrix} \hat{\mathbf{A}}_1 \\ \hat{\mathbf{A}}_2 \\ \hat{\mathbf{A}}_3 \end{pmatrix}, \quad \mathbf{B} = \begin{pmatrix} \hat{\mathbf{B}}_1 \\ \hat{\mathbf{B}}_2 \\ \hat{\mathbf{B}}_3 \end{pmatrix} \quad (2.26)$$

These matrices convert from space-fixed (xyz) to body-fixed (123) coordinates.

Allen and Germano,[60] following earlier work by Price *et al.*,[61] showed that if the interaction energies are written explicitly in terms of $\hat{\mathbf{r}}$ and the body axes $(\hat{\mathbf{A}}_m, \hat{\mathbf{B}}_n)$:

$$U(r, \{\hat{\mathbf{A}}_m \cdot \hat{\mathbf{r}}\}, \{\hat{\mathbf{B}}_n \cdot \hat{\mathbf{r}}\}, \{\hat{\mathbf{A}}_m \cdot \hat{\mathbf{B}}_n\}). \quad (2.27)$$

the forces come out relatively cleanly,

$$\begin{aligned} \mathbf{F}_a &= -\mathbf{F}_b = \nabla U = \frac{\partial U}{\partial \mathbf{r}} \\ &= \frac{\partial U}{\partial r} \hat{\mathbf{r}} + \sum_m \left[\frac{\partial U}{\partial(\hat{\mathbf{A}}_m \cdot \hat{\mathbf{r}})} \frac{\partial(\hat{\mathbf{A}}_m \cdot \hat{\mathbf{r}})}{\partial \mathbf{r}} + \frac{\partial U}{\partial(\hat{\mathbf{B}}_m \cdot \hat{\mathbf{r}})} \frac{\partial(\hat{\mathbf{B}}_m \cdot \hat{\mathbf{r}})}{\partial \mathbf{r}} \right]. \end{aligned} \quad (2.28)$$

The torques can also be found in a relatively similar manner,

$$\tau_a = \sum_m \frac{\partial U}{\partial(\hat{\mathbf{A}}_m \cdot \hat{\mathbf{r}})} (\hat{\mathbf{r}} \times \hat{\mathbf{A}}_m) - \sum_{mn} \frac{\partial U}{\partial(\hat{\mathbf{A}}_m \cdot \hat{\mathbf{B}}_n)} (\hat{\mathbf{A}}_m \times \hat{\mathbf{B}}_n) \quad (2.29)$$

$$\tau_b = \sum_m \frac{\partial U}{\partial(\hat{\mathbf{B}}_m \cdot \hat{\mathbf{r}})} (\hat{\mathbf{r}} \times \hat{\mathbf{B}}_m) + \sum_{mn} \frac{\partial U}{\partial(\hat{\mathbf{A}}_m \cdot \hat{\mathbf{B}}_n)} (\hat{\mathbf{A}}_m \times \hat{\mathbf{B}}_n). \quad (2.30)$$

Note that our definition of $\mathbf{r} = \mathbf{r}_b - \mathbf{r}_a$ is opposite in sign to that of Allen and Germano.[60] We also made use of the identities,

$$\frac{\partial(\hat{\mathbf{A}}_m \cdot \hat{\mathbf{r}})}{\partial \mathbf{r}} = \frac{1}{r} \left(\hat{\mathbf{A}}_m - (\hat{\mathbf{A}}_m \cdot \hat{\mathbf{r}}) \hat{\mathbf{r}} \right) \quad (2.31)$$

$$\frac{\partial(\hat{\mathbf{B}}_m \cdot \hat{\mathbf{r}})}{\partial \mathbf{r}} = \frac{1}{r} \left(\hat{\mathbf{B}}_m - (\hat{\mathbf{B}}_m \cdot \hat{\mathbf{r}}) \hat{\mathbf{r}} \right). \quad (2.32)$$

Many of the multipole contractions required can be written in one of three equivalent forms using the unit vectors $\hat{\mathbf{r}}$, $\hat{\mathbf{A}}_m$, and $\hat{\mathbf{B}}_n$. In the torque expressions, it is useful to have the angular-dependent terms available in all three fashions, e.g. for the dipole-dipole contraction:

$$\mathbf{D}_a \cdot \mathbf{D}_b = D_{a\alpha} D_{b\alpha} = \sum_{mn} D_{am} \hat{\mathbf{A}}_m \cdot \hat{\mathbf{B}}_n D_{bn}. \quad (2.33)$$

The first two forms are written using space coordinates. The first form is standard in the chemistry literature, while the second is expressed using implied summation notation. The third form shows explicit sums over body indices and the dot products now indicate contractions using space indices.

In computing our force and torque expressions, we carried out most of the work in body coordinates, and have transformed the expressions back to space-frame coordinates, which are reported below. Interested readers may consult supplemental information of the Ref. [62] for the intermediate body-frame expressions.

2.2.9 The Self-Interaction

In addition to cutoff-sphere neutralization, the Wolf summation [16] and the damped shifted force (DSF) extension [15] also include self-interactions that are handled separately from the pairwise interactions between sites. The self-term is normally calculated via a single loop over all sites in the system, and is relatively cheap to evaluate. The self-interaction has contributions from two sources.

First, the neutralization procedure within the cutoff radius requires a contribution from a charge opposite in sign, but equal in magnitude, to the central charge, which has been spread out over the surface of the cutoff sphere. For a system of undamped charges, the total self-term is

$$U_{\text{self}} = -\frac{1}{r_c} \sum_{a=1}^N C_a^2. \quad (2.34)$$

The extension of DSF electrostatics to point multipoles requires treatment of the self-neutralization *and* reciprocal contributions to the self-interaction for higher order multipoles. In this section we give formulae for these interactions up to quadrupolar order.

The self-neutralization term is computed by taking the *non-shifted* kernel for each interaction, placing a multipole of equal magnitude (but opposite in polarization) on the surface of the cutoff sphere, and averaging over the surface of the cutoff sphere. Because the self term is carried out as a single sum over sites, the reciprocal-space portion is identical to half of the self-term obtained by Smith, and also by Aguado and Madden for the application of the Ewald sum to multipoles.[63–65] For a given site which possesses a charge, dipole, and quadrupole, both types of contribution are given in Table 2.1.

For sites which simultaneously contain charges and quadrupoles, the self-

TABLE 2.1: Self-interaction contributions for site (a) that has a charge (C_a), dipole (\mathbf{D}_a), and quadrupole (\mathbf{Q}_a)

Multipole order	Summed Quantity	Self-neutralization	Reciprocal
Charge	C_a^2	$-f(r_c)$	$-\frac{\alpha}{\sqrt{\pi}}$
Dipole	$ \mathbf{D}_a ^2$	$\frac{1}{3} \left(h(r_c) + \frac{2g(r_c)}{r_c} \right)$	$-\frac{2\alpha^3}{3\sqrt{\pi}}$
Quadrupole	$2\mathbf{Q}_a : \mathbf{Q}_a + \text{Tr}(\mathbf{Q}_a)^2$	$-\frac{1}{15} \left(t(r_c) + \frac{4s(r_c)}{r_c} \right)$	$-\frac{4\alpha^5}{5\sqrt{\pi}}$
Charge-Quadrupole	$-2C_a \text{Tr}(\mathbf{Q}_a)$	$\frac{1}{3} \left(h(r_c) + \frac{2g(r_c)}{r_c} \right)$	$-\frac{2\alpha^3}{3\sqrt{\pi}}$

interaction includes a cross-interaction between these two multipole orders. Symmetry prevents the charge-dipole and dipole-quadrupole interactions from contributing to the self-interaction. The functions that go into the self-neutralization terms, $g(r)$, $h(r)$, $s(r)$, and $t(r)$ are successive derivatives of the electrostatic kernel, $f(r)$ (either the undamped $1/r$ or the damped $B_0(r) = \text{erfc}(\alpha r)/r$ function) that have been evaluated at the cutoff distance. For undamped interactions, $f(r_c) = 1/r_c$, $g(r_c) = -1/r_c^2$, and so on. For damped interactions, $f(r_c) = B_0(r_c)$, $g(r_c) = B'_0(r_c)$, and so on. Appendix A.1 contains recursion relations that allow rapid evaluation of these derivatives.

2.3 Interaction energies, forces, and torques

The main result of this chapter is a set of expressions for the energies, forces and torques (up to quadrupole-quadrupole order) that work for the Taylor-shifted, gradient-shifted, and shifted potential approximations. These expressions were derived using a set of generic radial functions. Without using the shifting approximations mentioned above, some of these radial functions would be identical, and the expressions coalesce into the familiar forms for unmodified multipole-multipole interactions. Table 2.2 maps between the generic functions and the

radial functions derived for the three methods. The energy equations are written in terms of lab-frame representations of the dipoles, quadrupoles, and the unit vector connecting the two objects,

$$U_{C_a C_b}(r) = C_a C_b v_{01}(r) \quad (2.35)$$

$$U_{C_a \mathbf{D}_b}(r) = C_a (\mathbf{D}_b \cdot \hat{\mathbf{r}}) v_{11}(r) \quad (2.36)$$

$$U_{C_a \mathbf{Q}_b}(r) = C_a \left[\text{Tr} \mathbf{Q}_b v_{21}(r) + (\hat{\mathbf{r}} \cdot \mathbf{Q}_b \cdot \hat{\mathbf{r}}) v_{22}(r) \right] \quad (2.37)$$

$$U_{\mathbf{D}_a \mathbf{D}_b}(r) = - \left[(\mathbf{D}_a \cdot \mathbf{D}_b) v_{21}(r) + (\mathbf{D}_a \cdot \hat{\mathbf{r}}) (\mathbf{D}_b \cdot \hat{\mathbf{r}}) v_{22}(r) \right] \quad (2.38)$$

$$\begin{aligned} U_{\mathbf{D}_a \mathbf{Q}_b}(r) = & - \left[\text{Tr} \mathbf{Q}_b (\mathbf{D}_a \cdot \hat{\mathbf{r}}) + 2(\mathbf{D}_a \cdot \mathbf{Q}_b \cdot \hat{\mathbf{r}}) \right] v_{31}(r) \\ & - (\mathbf{D}_a \cdot \hat{\mathbf{r}}) (\hat{\mathbf{r}} \cdot \mathbf{Q}_b \cdot \hat{\mathbf{r}}) v_{32}(r) \end{aligned} \quad (2.39)$$

$$\begin{aligned} U_{\mathbf{Q}_a \mathbf{Q}_b}(r) = & \left[\text{Tr} \mathbf{Q}_a \text{Tr} \mathbf{Q}_b + 2\mathbf{Q}_a : \mathbf{Q}_b \right] v_{41}(r) \\ & + \left[\text{Tr} \mathbf{Q}_a (\hat{\mathbf{r}} \cdot \mathbf{Q}_b \cdot \hat{\mathbf{r}}) + \text{Tr} \mathbf{Q}_b (\hat{\mathbf{r}} \cdot \mathbf{Q}_a \cdot \hat{\mathbf{r}}) + 4(\hat{\mathbf{r}} \cdot \mathbf{Q}_a \cdot \mathbf{Q}_b \cdot \hat{\mathbf{r}}) \right] v_{42}(r) \\ & + (\hat{\mathbf{r}} \cdot \mathbf{Q}_a \cdot \hat{\mathbf{r}}) (\hat{\mathbf{r}} \cdot \mathbf{Q}_b \cdot \hat{\mathbf{r}}) v_{43}(r). \end{aligned} \quad (2.40)$$

Note that the energies of multipoles on site b interacting with those on site a can be obtained by swapping indices along with the sign of the intersite vector, $\hat{\mathbf{r}}$.

2.3.1 Forces

The force on object a , \mathbf{F}_a , due to object b is the negative of the force on b due to a . For a simple charge-charge interaction, these forces will point along the $\pm \hat{\mathbf{r}}$ directions, where $\mathbf{r} = \mathbf{r}_b - \mathbf{r}_a$. Thus

$$F_{a\alpha} = \hat{r}_\alpha \frac{\partial U_{C_a C_b}}{\partial r} \quad \text{and} \quad F_{b\alpha} = -\hat{r}_\alpha \frac{\partial U_{C_a C_b}}{\partial r}. \quad (2.41)$$

TABLE 2.2: Radial functions used in the energy and torque equations. The f, g, h, s, t , and u functions used in this table are defined in Appendices A.2 and A.3. The gradient shifted (GSF) functions include the shifted potential (SP) contributions (*cf.* Eqs. 2.23 and 2.25).

Generic	Bare Coulomb	Taylor-Shifted (TSF)	Shifted Potential (SP)	Gradient-Shifted (GSF)
$v_{01}(r)$	$\frac{1}{r}$	$f_0(r)$	$f(r) - f(r_c)$	$\text{SP} - (r - r_c)g(r_c)$
$v_{11}(r)$	$-\frac{1}{r^2}$	$g_1(r)$	$g(r) - g(r_c)$	$\text{SP} - (r - r_c)h(r_c)$
$v_{21}(r)$	$-\frac{1}{r^3}$	$\frac{g_2(r)}{r}$	$\frac{g(r) - g(r_c)}{r - r_c}$	$\text{SP} - (r - r_c)\left(-\frac{g(r_c)}{r_c^2} + \frac{h(r_c)}{r_c}\right)$
$v_{22}(r)$	$\frac{3}{r^3}$	$\left(-\frac{g_2(r)}{r} + h_2(r)\right)$	$\left(-\frac{g(r)}{r} + h(r)\right) - \left(-\frac{g(r_c)}{r_c} + h(r_c)\right)$	$\text{SP} - (r - r_c)\left(\frac{g(r_c)}{r_c^2} - \frac{h(r_c)}{r_c} + s(r_c)\right)$
$v_{31}(r)$	$\frac{3}{r^4}$	$\left(-\frac{g_3(r)}{r^2} + \frac{h_3(r)}{r}\right)$	$\left(-\frac{g(r)}{r^2} + \frac{h(r)}{r}\right) - \left(-\frac{g(r_c)}{r_c^2} + \frac{h(r_c)}{r_c}\right)$	$\text{SP} - (r - r_c)\left(\frac{2g(r_c)}{r_c^3} - \frac{2h(r_c)}{r_c^2} + \frac{s(r_c)}{r_c}\right)$
$v_{32}(r)$	$-\frac{15}{r^4}$	$\left(\frac{3g_3(r)}{r^2} - \frac{3h_3(r)}{r} + s_3(r)\right)$	$\left(\frac{3g(r)}{r^2} - \frac{3h(r)}{r} + s(r)\right) - \left(\frac{3g(r_c)}{r_c^2} - \frac{3h(r_c)}{r_c} + s(r_c)\right)$	$\text{SP} - (r - r_c)\left(\frac{-6g(r_c)}{r_c^3} + \frac{6h(r_c)}{r_c^2} - \frac{6s(r_c)}{r_c}\right)$
$v_{41}(r)$	$\frac{3}{r^5}$	$\left(-\frac{g_4(r)}{r^3} + \frac{h_4(r)}{r^2}\right)$	$\left(-\frac{g(r)}{r^3} + \frac{h(r)}{r^2}\right) - \left(-\frac{g(r_c)}{r_c^3} + \frac{h(r_c)}{r_c^2}\right)$	$\text{SP} - (r - r_c)\left(\frac{3g(r_c)}{r_c^4} - \frac{3h(r_c)}{r_c^3} + \frac{s(r_c)}{r_c^2}\right)$
$v_{42}(r)$	$-\frac{15}{r^5}$	$\left(\frac{3g_4(r)}{r^3} - \frac{3h_4(r)}{r^2} + \frac{s_4(r)}{r}\right)$	$\left(\frac{3g(r)}{r^3} - \frac{3h(r)}{r^2} + \frac{s(r)}{r}\right) - \left(\frac{3g(r_c)}{r_c^3} - \frac{3h(r_c)}{r_c^2} + \frac{s(r_c)}{r_c}\right)$	$\text{SP} - (r - r_c)\left(-\frac{9g(r_c)}{r_c^4} + \frac{9h(r_c)}{r_c^3} - \frac{4s(r_c)}{r_c^2} + \frac{t(r_c)}{r_c}\right)$
$v_{43}(r)$	$\frac{105}{r^5}$	$\left(-\frac{15g_4(r)}{r^3} + \frac{15h_4(r)}{r^2} - \frac{6s_4(r)}{r} + t_4(r)\right)$	$\left(-\frac{15g(r)}{r^3} + \frac{15h(r)}{r^2} - \frac{6s(r)}{r} + t(r)\right) - \left(-\frac{15g(r_c)}{r_c^3} + \frac{15h(r_c)}{r_c^2} - \frac{6s(r_c)}{r_c} + t(r_c)\right)$	$\text{SP} - (r - r_c)\left(\frac{45g(r_c)}{r_c^4} - \frac{45h(r_c)}{r_c^3} + \frac{21s(r_c)}{r_c^2} - \frac{6t(r_c)}{r_c} + u(r_c)\right)$

TABLE 2.3: Radial functions used in the force equations. Gradient shifted (GSF) functions are constructed using the shifted potential (SP) functions. Some of these functions are simple modifications of the functions found in Table 2.2

Function	Definition	Taylor-Shifted (TSF)	Shifted Potential (SP)	Gradient-Shifted (GSF)
$w_a(r)$	$\frac{dv_{01}}{dr}$	$g_0(r)$	$g(r)$	$SP - g(r_c)$
$w_b(r)$	$\frac{dv_{11}}{dr} - \frac{v_{11}(r)}{r}$	$\left(-\frac{g_1(r)}{r} + h_1(r)\right)$	$h(r) - \frac{v_{11}(r)}{r}$	$SP - h(r_c)$
$w_c(r)$	$\frac{v_{11}(r)}{r}$	$\frac{g_1(r)}{r}$	$\frac{v_{11}(r)}{r}$	$\frac{v_{11}(r)}{r}$
$w_d(r)$	$\frac{dv_{21}}{dr}$	$\left(-\frac{g_2(r)}{r^2} + \frac{h_2(r)}{r}\right)$	$\left(-\frac{g(r)}{r^2} + \frac{h(r)}{r}\right)$	$SP - \left(-\frac{g(r_c)}{r_c^2} + \frac{h(r_c)}{r_c}\right)$
$w_e(r)$	$\frac{v_{22}(r)}{r}$	$\left(-\frac{g_2(r)}{r^2} + \frac{h_2(r)}{r}\right)$	$\frac{v_{22}(r)}{r}$	$\frac{v_{22}(r)}{r}$
$w_f(r)$	$\frac{dv_{22}}{dr} - \frac{2v_{22}(r)}{r}$	$\left(\frac{3g_2(r)}{r^2} - \frac{3h_2(r)}{r} + s_2(r)\right)$	$\left(\frac{g(r)}{r^2} - \frac{h(r)}{r} + s(r)\right) - \frac{2v_{22}(r)}{r}$	$SP - \left(\frac{g(r_c)}{r_c^2} - \frac{h(r_c)}{r_c} + s(r_c)\right)$
$w_g(r)$	$\frac{v_{31}(r)}{r}$	$\left(-\frac{g_3(r)}{r^3} + \frac{h_3(r)}{r^2}\right)$	$\frac{v_{31}(r)}{r}$	$\frac{v_{31}(r)}{r}$
$w_h(r)$	$\frac{dv_{31}}{dr} - \frac{v_{31}(r)}{r}$	$\left(\frac{3g_3(r)}{r^3} - \frac{3h_3(r)}{r^2} + \frac{s_3(r)}{r}\right)$	$\left(\frac{2g(r)}{r^3} - \frac{2h(r)}{r^2} + \frac{s(r)}{r}\right) - \frac{v_{31}(r)}{r}$	$SP - \left(\frac{2g(r_c)}{r_c^3} - \frac{2h(r_c)}{r_c^2} + \frac{s(r_c)}{r_c}\right)$
$w_i(r)$	$\frac{v_{32}(r)}{r}$	$\left(\frac{3g_3(r)}{r^3} - \frac{3h_3(r)}{r^2} + \frac{s_3(r)}{r}\right)$	$\frac{v_{32}(r)}{r}$	$\frac{v_{32}(r)}{r}$
$w_j(r)$	$\frac{dv_{32}}{dr} - \frac{3v_{32}}{r}$	$\left(-\frac{15g_3(r)}{r^3} + \frac{15h_3(r)}{r^2} - \frac{6s_3(r)}{r} + t_3(r)\right)$	$\left(-\frac{6g(r)}{r^3} + \frac{6h(r)}{r^2} - \frac{3s(r)}{r} + t(r)\right) - \frac{3v_{32}}{r}$	$SP - \left(-\frac{6g(r_c)}{r_c^3} + \frac{6h(r_c)}{r_c^2} - \frac{3s(r_c)}{r_c} + t(r_c)\right)$
$w_k(r)$	$\frac{dv_{41}}{dr}$	$\left(\frac{3g_4(r)}{r^4} - \frac{3h_4(r)}{r^3} + \frac{s_4(r)}{r^2}\right)$	$\left(\frac{3g(r)}{r^4} - \frac{3h(r)}{r^3} + \frac{s(r)}{r^2}\right)$	$SP - \left(\frac{3g(r_c)}{r_c^4} - \frac{3h(r_c)}{r_c^3} + \frac{s(r_c)}{r_c^2}\right)$
$w_l(r)$	$\frac{dv_{42}}{dr} - \frac{2v_{42}(r)}{r}$	$\left(-\frac{15g_4(r)}{r^4} + \frac{15h_4(r)}{r^3} - \frac{6s_4(r)}{r^2} + \frac{t_4(r)}{r}\right)$	$\left(-\frac{9g(r)}{r^4} + \frac{9h(r)}{r^3} - \frac{4s(r)}{r^2} + \frac{t(r)}{r}\right) - \frac{2v_{42}(r)}{r}$	$SP - \left(-\frac{9g(r_c)}{r_c^4} + \frac{9h(r_c)}{r_c^3} - \frac{4s(r_c)}{r_c^2} + \frac{t(r_c)}{r_c}\right)$
$w_m(r)$	$\frac{dv_{43}}{dr} - \frac{4v_{43}(r)}{r}$	$\left(\frac{105g_4(r)}{r^4} - \frac{105h_4(r)}{r^3} + \frac{45s_4(r)}{r^2} - \frac{21t_4(r)}{r}\right)$	$\left(\frac{45g(r)}{r^4} - \frac{45h(r)}{r^3} + \frac{21s(r)}{r^2} - \frac{21t(r)}{r}\right)$	$SP - \left(\frac{45g(r_c)}{r_c^4} - \frac{45h(r_c)}{r_c^3} + \frac{21s(r_c)}{r_c^2} - \frac{21t(r_c)}{r_c}\right)$
$w_n(r)$	$\frac{v_{42}(r)}{r}$	$\left(\frac{3g_4(r)}{r^4} - \frac{3h_4(r)}{r^3} + \frac{s_4(r)}{r^2}\right)$	$-\frac{6t(r)}{r} + u(r) - \frac{4v_{43}(r)}{r}$	$+\frac{21s(r_c)}{r_c^2} - \frac{6t(r_c)}{r_c} + u(r_c)$
$w_o(r)$	$\frac{v_{43}(r)}{r}$	$\left(-\frac{15g_4(r)}{r^4} + \frac{15h_4(r)}{r^3} - \frac{6s_4(r)}{r^2} + \frac{t_4(r)}{r}\right)$	$\frac{v_{42}(r)}{r}$	$\frac{v_{42}(r)}{r}$
			$\frac{v_{43}(r)}{r}$	$\frac{v_{43}(r)}{r}$

We list below the force equations written in terms of lab-frame coordinates. The radial functions used in the three methods are listed in Table 2.3

$$\mathbf{F}_{aC_aC_b} = C_a C_b w_a(r) \hat{\mathbf{r}} \quad (2.42)$$

$$\mathbf{F}_{aC_a\mathbf{D}_b} = C_a \left[(\hat{\mathbf{r}} \cdot \mathbf{D}_b) w_b(r) \hat{\mathbf{r}} + \mathbf{D}_b w_c(r) \right] \quad (2.43)$$

$$\mathbf{F}_{aC_a\mathbf{Q}_b} = C_a \left[\text{Tr} \mathbf{Q}_b w_d(r) \hat{\mathbf{r}} + 2 \mathbf{Q}_b \cdot \hat{\mathbf{r}} w_e(r) + (\hat{\mathbf{r}} \cdot \mathbf{Q}_b \cdot \hat{\mathbf{r}}) w_f(r) \hat{\mathbf{r}} \right] \quad (2.44)$$

$$\begin{aligned} \mathbf{F}_{a\mathbf{D}_a\mathbf{D}_b} = & -\mathbf{D}_a \cdot \mathbf{D}_b w_d(r) \hat{\mathbf{r}} + (\mathbf{D}_a (\mathbf{D}_b \cdot \hat{\mathbf{r}}) + \mathbf{D}_b (\mathbf{D}_a \cdot \hat{\mathbf{r}})) w_e(r) \\ & - (\hat{\mathbf{r}} \cdot \mathbf{D}_a) (\hat{\mathbf{r}} \cdot \mathbf{D}_b) w_f(r) \hat{\mathbf{r}} \end{aligned} \quad (2.45)$$

$$\begin{aligned} \mathbf{F}_{a\mathbf{D}_a\mathbf{Q}_b} = & - \left[\text{Tr} \mathbf{Q}_b \mathbf{D}_a + 2 \mathbf{D}_a \cdot \mathbf{Q}_b \right] w_g(r) - \left[\text{Tr} \mathbf{Q}_b (\hat{\mathbf{r}} \cdot \mathbf{D}_a) + 2 (\mathbf{D}_a \cdot \mathbf{Q}_b \cdot \hat{\mathbf{r}}) \right] w_h(r) \hat{\mathbf{r}} \\ & - \left[\mathbf{D}_a (\hat{\mathbf{r}} \cdot \mathbf{Q}_b \cdot \hat{\mathbf{r}}) + 2 (\hat{\mathbf{r}} \cdot \mathbf{D}_a) (\hat{\mathbf{r}} \cdot \mathbf{Q}_b) \right] w_i(r) - (\hat{\mathbf{r}} \cdot \mathbf{D}_a) (\hat{\mathbf{r}} \cdot \mathbf{Q}_b \cdot \hat{\mathbf{r}}) w_j(r) \hat{\mathbf{r}} \end{aligned} \quad (2.46)$$

$$\begin{aligned} \mathbf{F}_{a\mathbf{Q}_a\mathbf{Q}_b} = & \left[\text{Tr} \mathbf{Q}_a \text{Tr} \mathbf{Q}_b + 2 \mathbf{Q}_a : \mathbf{Q}_b \right] w_k(r) \hat{\mathbf{r}} \\ & + \left[2 \text{Tr} \mathbf{Q}_b (\hat{\mathbf{r}} \cdot \mathbf{Q}_a) + 2 \text{Tr} \mathbf{Q}_a (\hat{\mathbf{r}} \cdot \mathbf{Q}_b) + 4 (\mathbf{Q}_a \cdot \mathbf{Q}_b \cdot \hat{\mathbf{r}}) + 4 (\hat{\mathbf{r}} \cdot \mathbf{Q}_a \cdot \mathbf{Q}_b) \right] w_n(r) \\ & + \left[\text{Tr} \mathbf{Q}_a (\hat{\mathbf{r}} \cdot \mathbf{Q}_b \cdot \hat{\mathbf{r}}) + \text{Tr} \mathbf{Q}_b (\hat{\mathbf{r}} \cdot \mathbf{Q}_a \cdot \hat{\mathbf{r}}) + 4 (\hat{\mathbf{r}} \cdot \mathbf{Q}_a \cdot \mathbf{Q}_b \cdot \hat{\mathbf{r}}) \right] w_l(r) \hat{\mathbf{r}} \\ & + \left[+2 (\hat{\mathbf{r}} \cdot \mathbf{Q}_a) (\hat{\mathbf{r}} \cdot \mathbf{Q}_b \cdot \hat{\mathbf{r}}) + 2 (\hat{\mathbf{r}} \cdot \mathbf{Q}_a \cdot \hat{\mathbf{r}}) (\hat{\mathbf{r}} \cdot \mathbf{Q}_b) \right] w_o(r) \\ & + (\hat{\mathbf{r}} \cdot \mathbf{Q}_a \cdot \hat{\mathbf{r}}) (\hat{\mathbf{r}} \cdot \mathbf{Q}_b \cdot \hat{\mathbf{r}}) w_m(r) \hat{\mathbf{r}} \end{aligned} \quad (2.47)$$

Note that the forces for higher multipoles on site a interacting with those of lower order on site b can be obtained by swapping indices in the expressions above.

2.3.2 Torques

The torques for the three methods are given in space-frame coordinates:

$$\tau_{bC_a\mathbf{D}_b} = C_a(\hat{\mathbf{r}} \times \mathbf{D}_b)v_{11}(r) \quad (2.48)$$

$$\tau_{bC_a\mathbf{Q}_b} = 2C_a\hat{\mathbf{r}} \times (\mathbf{Q}_b \cdot \hat{\mathbf{r}})v_{22}(r) \quad (2.49)$$

$$\tau_{a\mathbf{D}_a\mathbf{D}_b} = \mathbf{D}_a \times \mathbf{D}_b v_{21}(r) - (\hat{\mathbf{r}} \times \mathbf{D}_a)(\hat{\mathbf{r}} \cdot \mathbf{D}_b)v_{22}(r) \quad (2.50)$$

$$\tau_{a\mathbf{D}_a\mathbf{Q}_b} = \left[-\text{Tr}\mathbf{Q}_b(\hat{\mathbf{r}} \times \mathbf{D}_a) + 2\mathbf{D}_a \times (\mathbf{Q}_b \cdot \hat{\mathbf{r}}) \right] v_{31}(r) - (\hat{\mathbf{r}} \times \mathbf{D}_a)(\hat{\mathbf{r}} \cdot \mathbf{Q}_b \cdot \hat{\mathbf{r}})v_{32}(r) \quad (2.51)$$

$$\tau_{b\mathbf{D}_a\mathbf{Q}_b} = \left[+2(\mathbf{D}_a \cdot \mathbf{Q}_b) \times \hat{\mathbf{r}} - 2\mathbf{D}_a \times (\mathbf{Q}_b \cdot \hat{\mathbf{r}}) \right] v_{31}(r) + (\hat{\mathbf{r}} \cdot \mathbf{D}_a)(\hat{\mathbf{r}} \cdot \mathbf{Q}_b) \times \hat{\mathbf{r}} v_{32}(r) \quad (2.52)$$

$$\begin{aligned} \tau_{a\mathbf{Q}_a\mathbf{Q}_b} = & -4\mathbf{Q}_a \times \mathbf{Q}_b v_{41}(r) \\ & + \left[-2\text{Tr}\mathbf{Q}_b(\hat{\mathbf{r}} \cdot \mathbf{Q}_a) \times \hat{\mathbf{r}} + 4\hat{\mathbf{r}} \times (\mathbf{Q}_a \cdot \mathbf{Q}_b \cdot \hat{\mathbf{r}}) - 4(\hat{\mathbf{r}} \cdot \mathbf{Q}_a) \times (\mathbf{Q}_b \cdot \hat{\mathbf{r}}) \right] v_{42}(r) \\ & + 2\hat{\mathbf{r}} \times (\mathbf{Q}_a \cdot \hat{\mathbf{r}})(\hat{\mathbf{r}} \cdot \mathbf{Q}_b \cdot \hat{\mathbf{r}})v_{43}(r) \end{aligned} \quad (2.53)$$

$$\begin{aligned} \tau_{b\mathbf{Q}_a\mathbf{Q}_b} = & 4\mathbf{Q}_a \times \mathbf{Q}_b v_{41}(r) \\ & + \left[-2\text{Tr}\mathbf{Q}_a(\hat{\mathbf{r}} \cdot \mathbf{Q}_b) \times \hat{\mathbf{r}} - 4(\hat{\mathbf{r}} \cdot \mathbf{Q}_a \cdot \mathbf{Q}_b) \times \hat{\mathbf{r}} + 4(\hat{\mathbf{r}} \cdot \mathbf{Q}_a) \times (\mathbf{Q}_b \cdot \hat{\mathbf{r}}) \right] v_{42}(r) \\ & + 2(\hat{\mathbf{r}} \cdot \mathbf{Q}_a \cdot \hat{\mathbf{r}})\hat{\mathbf{r}} \times (\mathbf{Q}_b \cdot \hat{\mathbf{r}})v_{43}(r) \end{aligned} \quad (2.54)$$

Here, we have defined the matrix cross product in an identical form as in Ref. [64]:

$$[\mathbf{A} \times \mathbf{B}]_{\alpha} = \sum_{\beta} [\mathbf{A}_{\alpha+1,\beta} \mathbf{B}_{\alpha+2,\beta} - \mathbf{A}_{\alpha+2,\beta} \mathbf{B}_{\alpha+1,\beta}] \quad (2.55)$$

where $\alpha + 1$ and $\alpha + 2$ are regarded as cyclic permutations of the matrix indices.

All of the radial functions required for torques are identical with the radial

functions previously computed for the interaction energies. These are tabulated for all three methods in Table 2.2. The torques for higher multipoles on site a interacting with those of lower order on site b can be obtained by swapping indices in the expressions above.

2.4 Comparison to known multipolar energies

To understand how these new real-space multipole methods behave in computer simulations, it is vital to test against established methods for computing electrostatic interactions in periodic systems, and to evaluate the size and sources of any errors that arise from the real-space cutoffs. In this chapter we test SP, TSF, and GSF electrostatics against analytical methods for computing the energies of ordered multipolar arrays. In the following chapter, we test the new methods against the multipolar Ewald sum for computing the energies, forces and torques for a wide range of typical condensed-phase (disordered) systems.

Because long-range electrostatic effects can be significant in crystalline materials, ordered multipolar arrays present one of the biggest challenges for real-space cutoff methods. The dipolar analogues to the Madelung constants were first worked out by Sauer, who computed the energies of ordered dipole arrays of zero magnetization and obtained a number of these constants.[66] This theory was developed more completely by Luttinger and Tisza[67, 68] who tabulated energy constants for the Sauer arrays and other periodic structures.

To test the new electrostatic methods, we have constructed very large, $N = 16,000$ (bcc) arrays of dipoles in the orientations described in Ref. [67]. These structures include “A” lattices with nearest neighbor chains of antiparallel dipoles, as well as “B” lattices with nearest neighbor strings of antiparallel dipoles if the

dipoles are contained in a plane perpendicular to the dipole direction that passes through the dipole. We have also studied the minimum energy structure for the BCC lattice that was found by Luttinger & Tisza. The total electrostatic energy density for any of the arrays is given by:

$$E = CN^2\mu^2 \quad (2.56)$$

where C is the energy constant (equivalent to the Madelung constant), N is the number of dipoles per unit volume, and μ is the strength of the dipole. Energy constants (converged to 1 part in 10^9) are given in the supplemental information Ref. [62].

For the purposes of testing the energy expressions and the self-neutralization schemes, the primary quantity of interest is the analytic energy constant for the perfect arrays. Convergence to these constants are shown as a function of the cutoff radius, r_c , for three different values of the damping coefficient, α in Fig.2.2. We have simultaneously tested a hard cutoff (where the kernel is simply truncated at the cutoff radius) in addition to the three new methods.

The hard cutoff exhibits oscillations around the analytic energy constants, and converges to incorrect energies when the complementary error function damping kernel is used. The shifted potential (SP) converges to the correct energy smoothly by $r_c = 4.5a$ even for the undamped case. This indicates that the shifting and the correction provided by the self term are required for obtaining accurate energies. The Taylor-shifted force (TSF) approximation appears to perturb the potential too much inside the cutoff region to provide accurate measures of the energy constants. GSF is a compromise, converging to the correct energies within $r_c = 6a$.

Quadrupolar analogues to the Madelung constants were first worked out by

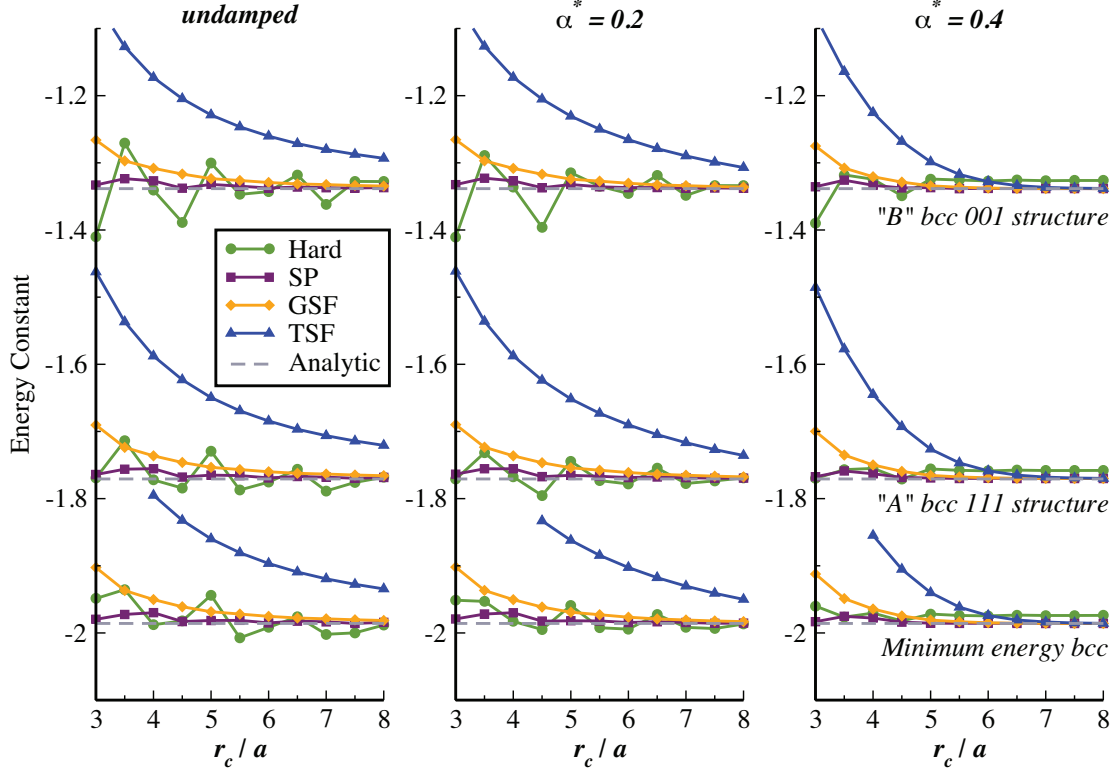


Figure 2.2. Convergence of the lattice energy constants as a function of cutoff radius (normalized by the lattice constant, a) for the new real-space methods. Three dipolar crystal structures were sampled, and the analytic energy constants for the three lattices are indicated with grey dashed lines. The left panel shows results for the undamped kernel ($1/r$), while the damped kernel, $B_0(r)$ was used in the center and right panels.

Nagai and Nakamura who computed the energies of selected quadrupole arrays based on extensions to the Luttinger and Tisza approach.[69, 70]

In analogy to the dipolar arrays, the total electrostatic energy for the quadrupolar arrays is:

$$E = CN \frac{3\bar{Q}^2}{4a^5} \quad (2.57)$$

where a is the lattice parameter, and \bar{Q} is the effective quadrupole moment,

$$\bar{Q}^2 = 2 (3\mathbf{Q} : \mathbf{Q} - (\text{Tr}\mathbf{Q})^2) \quad (2.58)$$

for the primitive quadrupole as defined in Eq. B.24. (For the traceless quadrupole tensor, $\Theta = 3\mathbf{Q} - \text{Tr}\mathbf{Q}$, the effective moment, $\bar{Q}^2 = \frac{2}{3}\Theta : \Theta$.)

To test the new electrostatic methods for quadrupoles, we have constructed very large, $N = 8,000$ (sc), 16,000 (bcc), and 32,000 (fcc) arrays of linear quadrupoles in the orientations described in Ref. [69]. We have compared the energy constants for these low-energy configurations for linear quadrupoles. Convergence to these constants are shown as a function of the cutoff radius, r_c , for three different values of the damping parameter, α in Fig. 2.3.

Again, we find that the hard cutoff exhibits oscillations around the analytic energy constants. The shifted potential (SP) approximation converges to the correct energy smoothly by $r_c = 3a$ even for the undamped case. The Taylor-shifted force (TSF) approximation again appears to perturb the potential too much inside the cutoff region to provide accurate measures of the energy constants. GSF again provides a compromise between the two methods – energies are converged by $r_c = 4.5a$, and the approximation is not as perturbative at short range as TSF.

It is also useful to understand the behavior of the lattice energy constants

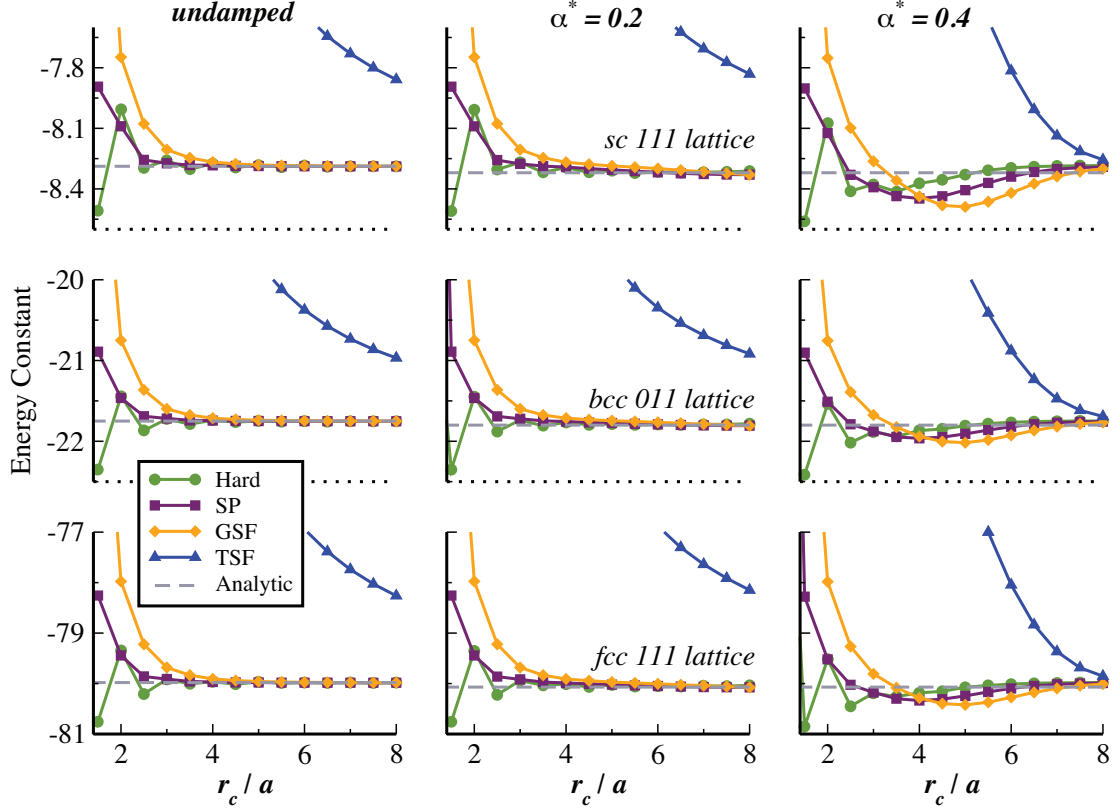


Figure 2.3. Convergence of the lattice energy constants as a function of cutoff radius (normalized by the lattice constant, a) for the new real-space methods. Three quadrupolar crystal structures were sampled, and the analytic energy constants for the three lattices are indicated with grey dashed lines. The left panel shows results for the undamped kernel ($1/r$), while the damped kernel, $B_0(r)$ was used in the center and right panels. Note that for quadrupoles, $\alpha^* = 0.4$ overdamps contributions from repulsive orientations in the perfect crystal.

for different values of the reduced damping parameter ($\alpha^* = \alpha a$) for the real-space methods. All of the methods (except for TSF) have excellent behavior for the undamped or weakly-damped cases. Overdamping can cause problems in perfect crystals for the quadrupoles in particular (*cf.* the right panel in Fig. 2.3). In the perfect crystals, only a few orientations are being sampled. E.g. in the simple cubic (SC) lattice of linear quadrupoles aligned in the 111 direction, the nearest-neighbor quadrupoles only sample 3 distinct orientations relative to the vector between the sites. The damping alters the radial function for the direct quadrupolar contraction, $v_{41}(r)$, differently than the radial functions for the terms involving the product of the separation vector with the quadrupoles, $v_{42}(r)$ and $v_{43}(r)$. Because these terms are altered by different amounts by the complementary error function damping, the effect of damping is non-spherical for multipoles, and the balance between attractive and repulsive interactions in the crystal is therefore altered significantly in overdamped situations.

In the chapter 3, we discuss how large values of α can perturb the force and torque vectors, but weakly-damped electrostatics appear to generate reasonable values for the total electrostatic energies under both the SP and GSF approximations. We also discuss the effects that α can have on convergence to the average electrostatic energies in liquids (which sample a much wider range of local orientations).

2.5 Summary

We have presented three efficient real-space methods for computing the interactions between point multipoles. One of these (SP) is a multipolar generalization of Wolf's method that smoothly shifts electrostatic energies to zero at the cutoff

radius. Two of these methods (GSF and TSF) also smoothly truncate the forces and torques (in addition to the energies) at the cutoff radius, making them attractive for both molecular dynamics and Monte Carlo simulations. We find that the Gradient-Shifted Force (GSF) and the Shifted-Potential (SP) methods converge rapidly to the correct lattice energies for ordered dipolar and quadrupolar arrays, while the Taylor-Shifted Force (TSF) is too severe an approximation to provide convergence to lattice energies within reasonable cutoff radii.

Although the TSF method appears to perform poorly for the analytical energy constants, the structure of the radial functions used in the force and torque expressions in the other two methods would not have been revealed without first developing the TSF approach. TSF also generates a set of electrostatic kernels that have multiple derivatives that vanish at the cutoff radius, a property that is valuable in estimating dielectric constants using the conducting boundary fluctuation formula.[37]

In most cases, GSF can obtain nearly quantitative agreement with the lattice energy constants with reasonably small cutoff radii. The only exception we have observed is for crystals which exhibit a bulk macroscopic dipole moment (e.g. Luttinger & Tisza’s Z_1 lattice). In this particular case, the multipole neutralization scheme can interfere with the correct computation of the energies. We note that the energies for these arrangements are typically much larger than for crystals with net-zero moments, so this is not expected to be an issue in most simulations.

Relatively weak damping is sufficient to converge to the analytical energy constants within moderately short cutoff distances. Because overdamping can present additional issues with higher order multipoles, our results indicate that the damping coefficient should be taken as small as possible, and that the *undamped* GSF

and SP methods may be the best choice in crystalline systems.

The techniques used here to derive the force, torque and energy expressions can be extended to higher order multipoles, although some of the objects (e.g. the matrix cross product in Eq. B.31) will need to be generalized for higher-rank tensors. We also note that the definitions of the multipoles used here are in a primitive form, and these need some care when comparing with experiment or other computational techniques.

In large systems, these new methods can be made to scale approximately linearly with system size, and detailed comparisons with the Ewald sum for a wide range of chemical environments follows in the chapter 3.

CHAPTER 3

COMPARISONS WITH THE EWALD SUM

In the previous chapter, I briefly discussed the short-ranged nature of the electrostatic interaction in the crystalline environment. This chapter discusses the property of the electrostatic interactions in more detail and extend the idea of the short-ranged nature of the interaction in the case of liquid simulation. I present the comparison of the energies, forces and torques calculated using real-space methods with the Ewald sum. Additionally I derive different static and dynamic properties using newly developed real-space methods and compare result with the Ewald. Finally I report on the conservation of total energy in the molecular dynamics simulation for the various real-space and Ewald methods.

3.1 Introduction

As we mentioned earlier Wolf *et al.*[16] proposed a real space $O(N)$ method for calculating electrostatic interactions between point charges. They argued that the effective Coulomb interaction in most condensed phase systems is effectively short ranged.[71, 72] For an ordered lattice (e.g., when computing the Madelung constant of an ionic solid), the material can be considered as a set of ions interacting with neutral dipolar or quadrupolar “molecules” giving an effective distance dependence for the electrostatic interactions of r^{-5} (see Fig. 3.1). If one views the

NaCl crystal as a simple cubic (SC) structure with an octupolar $(\text{NaCl})_4$ basis, the electrostatic energy per ion converges more rapidly to the Madelung energy than the dipolar approximation.[71] To find the correct Madelung constant, Lacman suggested that the NaCl structure could be constructed in a way that the finite crystal terminates with complete $(\text{NaCl})_4$ molecules.[73] The central ion sees what is effectively a set of octupoles at large distances. These facts suggest that the Madelung constants are relatively short ranged for perfect ionic crystals.[16] For this reason, careful application of Wolf’s method can provide accurate estimates of Madelung constants using relatively short cutoff radii.

Direct truncation of interactions at a cutoff radius creates numerical errors. Wolf *et al.* suggest that truncation errors are due to net charge remaining inside the cutoff sphere.[16] To neutralize this charge they proposed placing an image charge on the surface of the cutoff sphere for every real charge inside the cutoff sphere. These charges are present for the evaluation of both the pair interaction energy and the force, although the force expression maintains a discontinuity at the cutoff sphere. In the original Wolf formulation, the total energy for the charge and image were not equal to the integral of the force expression, and as a result, the total energy would not be conserved in molecular dynamics (MD) simulations.[17] Zahn *et al.*, and Fennell and Gezelter later proposed shifted force variants of the Wolf method with commensurate force and energy expressions that do not exhibit this problem.[15, 17] Related real-space methods were also proposed by Chen *et al.* [33–36] and by Wu and Brooks.[74] Recently, Fukuda has successfully used additional neutralization of higher order moments for systems of point charges.[28]

One can make a similar effective range argument for crystals of point *multi-*

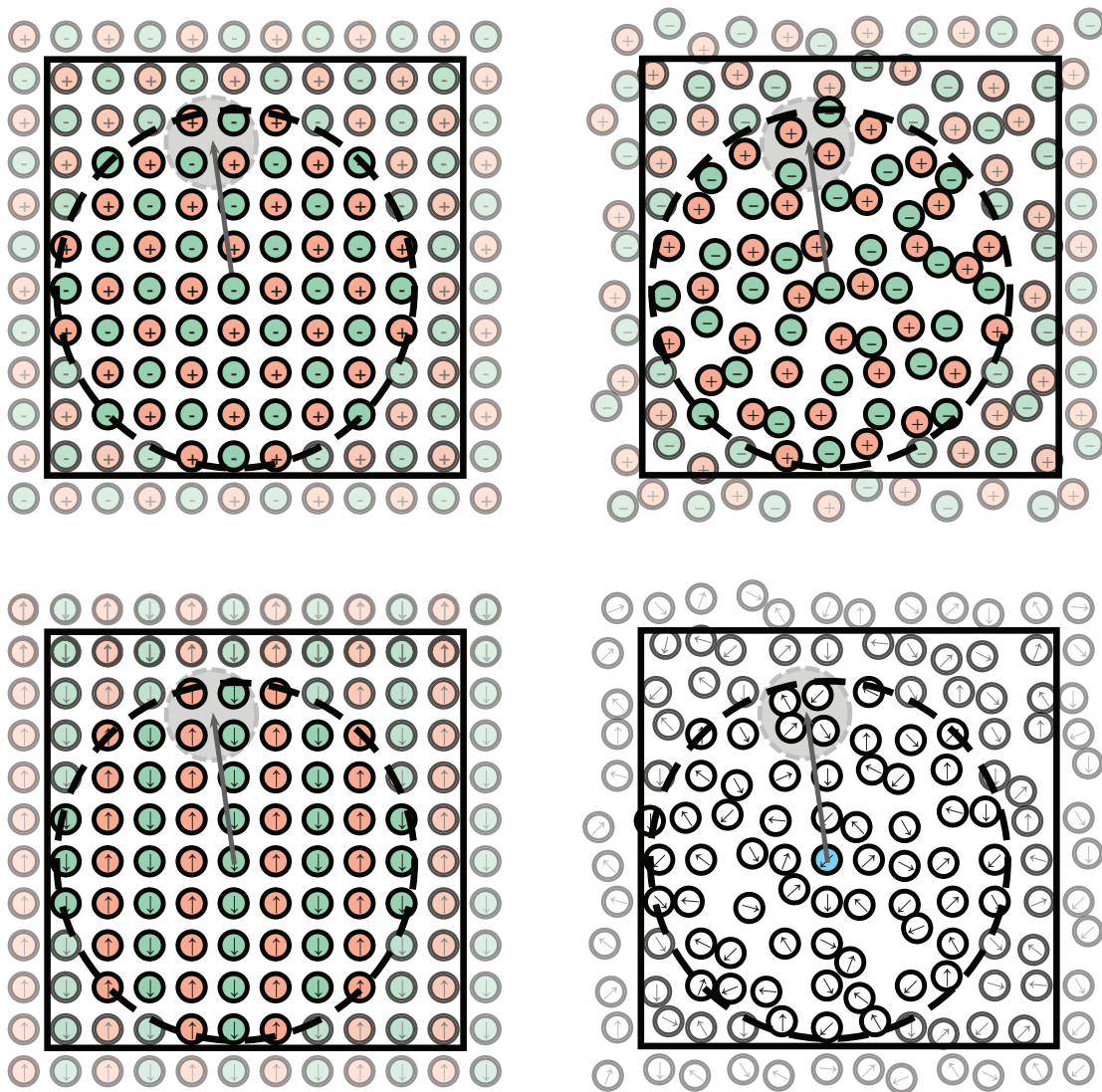


Figure 3.1. Top: Ionic systems exhibit local clustering of dissimilar charges (in the smaller grey circle), so interactions are effectively charge-multipole at longer distances. With hard cutoffs, motion of individual charges in and out of the cutoff sphere can break the effective multipolar ordering. Bottom: dipolar crystals and fluids have a similar effective *quadrupolar* ordering (in the smaller grey circles), and orientational averaging helps to reduce the effective range of the interactions in the fluid. Placement of reversed image multipoles on the surface of the cutoff sphere recovers the effective higher-order multipole behavior.

poles. The Luttinger and Tisza treatment of energy constants for dipolar lattices utilizes 24 basis vectors that contain dipoles at the eight corners of a unit cube.[67] Only three of these basis vectors, X_1, Y_1 , and Z_1 , retain net dipole moments, while the rest have zero net dipole and retain contributions only from higher order multipoles. The lowest-energy crystalline structures are built out of basis vectors that have only residual quadrupolar moments (e.g. the Z_5 array). In these low energy structures, the effective interaction between a dipole at the center of a crystal and a group of eight dipoles farther away is significantly shorter ranged than the r^{-3} that one would expect for raw dipole-dipole interactions. Only in crystals which retain a bulk dipole moment (e.g. ferroelectrics) does the analogy with the ionic crystal break down – ferroelectric dipolar crystals can exist, while ionic crystals with net charge in each unit cell would be unstable.

In ionic crystals, real-space truncation can break the effective multipolar arrangements (see Fig. 3.1), causing significant swings in the electrostatic energy as individual ions move back and forth across the boundary. This is why the image charges are necessary for the Wolf sum to exhibit rapid convergence. Similarly, the real-space truncation of point multipole interactions breaks higher order multipole arrangements, and image multipoles are required for real-space treatments of electrostatic energies.

The shorter effective range of electrostatic interactions is not limited to perfect crystals, but can also apply in disordered fluids. Even at elevated temperatures, there is local charge balance in an ionic liquid, where each positive ion has surroundings dominated by negative ions and vice versa. The reversed-charge images on the cutoff sphere that are integral to the Wolf and damped shifted force (DSF) approaches retain the effective multipolar interactions as the charges traverse the

cutoff boundary.

In multipolar fluids (see Fig. 3.1) there is significant orientational averaging that additionally reduces the effect of long-range multipolar interactions. The image multipoles that are introduced in the Taylor shifted force (TSF), gradient shifted force (GSF), and shifted potential (SP) methods mimic this effect and reduce the effective range of the multipolar interactions as interacting molecules traverse each other’s cutoff boundaries.

Forces and torques acting on atomic sites are fundamental in driving dynamics in molecular simulations, and the DSF energy kernel provides consistent energies and forces on charged atoms within the cutoff sphere. Both the energy and the force go smoothly to zero as an atom approaches the cutoff radius. The comparisons of the accuracy these quantities between the DSF kernel and SPME was surprisingly good.[15] As a result, the DSF method has seen increasing use in molecular systems with relatively uniform charge densities. [39–45]

3.2 Methodology

To understand how the real-space multipole methods behave in computer simulations, it is vital to test against established methods for computing electrostatic interactions in periodic systems, and to evaluate the size and sources of any errors that arise from the real-space cutoffs. In the chapter 2 of this series, we compared the dipolar and quadrupolar energy expressions against analytic expressions for ordered dipolar and quadrupolar arrays.[66, 67, 69, 70] In this work, we used the multipolar Ewald sum as a reference method for comparing energies, forces, and torques for molecular models that mimic disordered and ordered condensed-phase systems. The parameters used in the test cases are given in Table 3.1.

TABLE 3.1: The parameters used in the systems used to evaluate the new real-space methods. The most comprehensive test was a liquid composed of 2000 soft DQ liquid molecules with 48 dissolved ions (24 Na+ and 24 Cl- ions). This test exercises all orders of the multipolar interactions developed in the chapter 2.

Test system	LJ parameters		Electrostatic moments					mass (amu)	I_{xx}	I_{yy} (amu Å ²)	I_{zz}
	σ (Å)	ϵ (kcal/mol)	C (e)	D (debye)	Q_{xx} (debye Å)	Q_{yy} (debye Å)	Q_{zz} (debye Å)				
Soft Dipolar fluid	3.051	0.152		2.35				18.0153	1.77	0.6145	1.155
Soft Dipolar solid	2.837	1.0		2.35				10 ⁴	17.6	17.6	0
Soft Quadrupolar fluid	3.051	0.152			-1	-1	-2.5	18.0153	1.77	0.6145	1.155
Soft Quadrupolar solid	2.837	1.0			-1	-1	-2.5	10 ⁴	17.6	17.6	0
Soft DQ liquid	3.051	0.152		2.35	-1.35	0	-0.68	18.0153	1.77	0.6145	1.155
Na+	2.579	0.118	+1					22.99			
Cl-	4.445	0.1	-1					35.4527			

The systems consist of pure multipolar solids (both dipole and quadrupole), pure multipolar liquids (both dipole and quadrupole), a fluid composed of sites containing both dipoles and quadrupoles simultaneously, and a final test case that includes ions with point charges in addition to the multipolar fluid. The solid-phase parameters were chosen so that the systems can explore some orientational freedom for the multipolar sites, while maintaining relatively strict translational order. The soft DQ liquid model used here based loosely on the SSDQO water model,[49, 51, 52] but is not itself a particularly accurate water model. However, the soft DQ model does test dipole-dipole, dipole-quadrupole, and quadrupole-quadrupole interactions at roughly the same magnitudes. The last test case, a soft DQ liquid with dissolved ions, exercises *all* levels of the multipole-multipole interactions we have derived so far and represents the most complete test of the new methods.

In the following section, we present results for the total electrostatic energy, as well as the electrostatic contributions to the force and torque on each molecule. These quantities have been computed using the SP, TSF, and GSF methods, as well as a hard cutoff, and have been compared with the values obtained from the multipolar Ewald sum. In Monte Carlo (MC) simulations, the energy differences between two configurations is the primary quantity that governs how the simulation proceeds. These differences are the most important indicators of the reliability of a method even if the absolute energies are not exact. For each of the multipolar systems listed above, we have compared the change in electrostatic potential energy (ΔE) between 250 statistically-independent configurations. In molecular dynamics (MD) simulations, the forces and torques govern the behavior of the simulation, so we also compute the electrostatic contributions to the

forces and torques.

3.2.1 Implementation

The real-space methods developed in the chapter 2 in this series have been implemented in our group’s open source molecular simulation program, OpenMD,[18] which was used for all calculations in this work. The complementary error function can be a relatively slow function on some processors, so all of the radial functions are precomputed on a fine grid and are spline-interpolated to provide values when required.

Using the same simulation code, we compare to a multipolar Ewald sum with a reciprocal space cutoff, $k_{\text{max}} = 7$. Our version of the Ewald sum is a re-implementation of the algorithm originally proposed by Smith that does not use the particle mesh or smoothing approximations.[63, 64] This implementation was tested extensively against the analytic energy constants for the multipolar lattices that are discussed in reference.[62] In all cases discussed below, the quantities being compared are the electrostatic contributions to energies, force, and torques. All other contributions to these quantities (i.e. from Lennard-Jones interactions) are removed prior to the comparisons.

The convergence parameter (α) also plays a role in the balance of the real-space and reciprocal-space portions of the Ewald calculation. Typical molecular mechanics packages set this to a value that depends on the cutoff radius and a tolerance (typically less than 1×10^{-4} kcal/mol). Smaller tolerances are typically associated with increasing accuracy at the expense of computational time spent on the reciprocal-space portion of the summation.[4, 8] A default tolerance of 1×10^{-8} kcal/mol was used in all Ewald calculations, resulting in Ewald coefficient 0.3119

\AA^{-1} for a cutoff radius of 12 \AA .

The real-space models have self-interactions that provide contributions to the energies only. Although the self interaction is a rapid calculation, we note that in systems with fluctuating charges or point polarizabilities, the self-term is not static and must be recomputed at each time step.

3.2.2 Model systems

To sample independent configurations of the multipolar crystals, body centered cubic (bcc) crystals, which exhibit the minimum energy structures for point dipoles, were generated using 3,456 molecules. The multipoles were translationally locked in their respective crystal sites for equilibration at a relatively low temperature (50K) so that dipoles or quadrupoles could freely explore all accessible orientations. The translational constraints were then removed, the systems were re-equilibrated, and the crystals were simulated for an additional 10 ps in the microcanonical (NVE) ensemble with an average temperature of 50 K. The balance between moments of inertia and particle mass were chosen to allow orientational sampling without significant translational motion. Configurations were sampled at equal time intervals in order to compare configurational energy differences. The crystals were simulated far from the melting point in order to avoid translational deformation away of the ideal lattice geometry.

For dipolar, quadrupolar, and mixed-multipole *liquid* simulations, each system was created with 2,048 randomly-oriented molecules. These were equilibrated at a temperature of 300K for 1 ns. Each system was then simulated for 1 ns in the microcanonical (NVE) ensemble with the Dullweber, Leimkuhler, and McLachlan (DLM) symplectic splitting integrator using 1 fs timesteps.[75] We collected 250

different configurations at equal time intervals. For the liquid system that included ionic species, we converted 48 randomly-distributed molecules into 24 Na⁺ and 24 Cl⁻ ions and re-equilibrated. After equilibration, the system was run under the same conditions for 1 ns. A total of 250 configurations were collected. In the following comparisons of energies, forces, and torques, the Lennard-Jones potentials were turned off and only the purely electrostatic quantities were compared with the same values obtained via the Ewald sum.

3.2.3 Accuracy of Energy Differences, Forces and Torques

The pairwise summation techniques (outlined above) were evaluated for use in MC simulations by studying the energy differences between different configurations. We took the Ewald-computed energy difference between two conformations to be the correct behavior. An ideal performance by one of the new methods would reproduce these energy differences exactly. The configurational energies being used here contain only contributions from electrostatic interactions. Lennard-Jones interactions were omitted from the comparison as they should be identical for all methods.

Since none of the real-space methods provide exact energy differences, we used least square regressions analysis for the six different molecular systems to compare ΔE from Hard, SP, GSF, and TSF with the multipolar Ewald reference method. A result of unity for both the correlation (slope) and coefficient of determination (R^2) for these regressions would indicate perfect agreement between the real-space method and the multipolar Ewald sum.

Molecular systems were run long enough to explore independent configurations and 250 configurations were recorded for comparison. Each system provided

31,125 energy differences for a total of 186,750 data points. Similarly, the magnitudes of the forces and torques have also been compared using least squares regression analysis. In the forces and torques comparison, the magnitudes of the forces acting in each molecule for each configuration were evaluated. For example, our dipolar liquid simulation contains 2048 molecules and there are 250 different configurations for each system resulting in 3,072,000 data points for comparison of forces and torques.

3.2.4 Analysis of vector quantities

Getting the magnitudes of the force and torque vectors correct is only part of the issue for carrying out accurate molecular dynamics simulations. Because the real space methods reweight the different orientational contributions to the energies, it is also important to understand how the methods impact the *directionality* of the force and torque vectors. Fisher developed a probability density function to analyse directional data sets,

$$p_f(\theta) = \frac{\kappa}{2 \sinh \kappa} \sin \theta e^{\kappa \cos \theta} \quad (3.1)$$

where κ measures directional dispersion of the data around the mean direction.[76] This quantity (κ) can be estimated as a reciprocal of the circular variance.[77] To quantify the directional error, forces obtained from the Ewald sum were taken as the mean (or correct) direction and the angle between the forces obtained via the Ewald sum and the real-space methods were evaluated,

$$\cos \theta_i = \frac{\mathbf{f}_i^{\text{Ewald}} \cdot \mathbf{f}_i^{\text{GSF}}}{|\mathbf{f}_i^{\text{Ewald}}| |\mathbf{f}_i^{\text{GSF}}|} \quad (3.2)$$

The total angular displacement of the vectors was calculated as,

$$R = \sqrt{\left(\sum_{i=1}^N \cos \theta_i\right)^2 + \left(\sum_{i=1}^N \sin \theta_i\right)^2} \quad (3.3)$$

where N is number of force vectors. The circular variance is defined as

$$\text{Var}(\theta) \approx 1/\kappa = 1 - R/N \quad (3.4)$$

The circular variance takes on values between from 0 to 1, with 0 indicating a perfect directional match between the Ewald force vectors and the real-space forces. Lower values of $\text{Var}(\theta)$ correspond to higher values of κ , which indicates tighter clustering of the real-space force vectors around the Ewald forces.

A similar analysis was carried out for the electrostatic contribution to the molecular torques as well as forces.

3.2.5 Energy conservation

To test conservation the energy for the methods, the mixed molecular system of 2000 soft DQ liquid molecules with 24 Na⁺ and 24 Cl⁻ ions was run for 1 ns in the microcanonical ensemble at an average temperature of 300K. Each of the different electrostatic methods (Ewald, Hard, SP, GSF, and TSF) was tested for a range of different damping values. The molecular system was started with same initial positions and velocities for all cutoff methods. The energy drift (δE_1) and standard deviation of the energy about the slope (δE_0) were evaluated from the total energy of the system as a function of time. Although both measures are valuable at investigating new methods for molecular dynamics, a useful interaction model must allow for long simulation times with minimal energy drift.

3.3 Results

3.3.1 Configurational energy differences

The combined coefficient of determination and slope for all six systems is shown in Fig. 3.2. Most of the methods reproduce the Ewald configurational energy differences with remarkable fidelity. Undamped hard cutoffs introduce a significant amount of random scatter in the energy differences which is apparent in the reduced value of R^2 for this method. This can be easily understood as configurations which exhibit small traversals of a few dipoles or quadrupoles out of the cutoff sphere will see large energy jumps when hard cutoffs are used. The orientations of the multipoles (particularly in the ordered crystals) mean that these energy jumps can go in either direction, producing a significant amount of random scatter, but no systematic error.

The TSF method produces energy differences that are highly correlated with the Ewald results, but it also introduces a significant systematic bias in the values of the energies, particularly for smaller cutoff values. The TSF method alters the distance dependence of different orientational contributions to the energy in a non-uniform way, so the size of the cutoff sphere can have a large effect, particularly for the crystalline systems.

Both the SP and GSF methods appear to reproduce the Ewald results with excellent fidelity, particularly for moderate damping ($\alpha \approx 0.2 \text{ \AA}^{-1}$) and with a commonly-used cutoff value ($r_c = 12 \text{ \AA}$). With the exception of the undamped hard cutoff, and the TSF method with short cutoffs, all of the methods would be appropriate for use in Monte Carlo simulations.

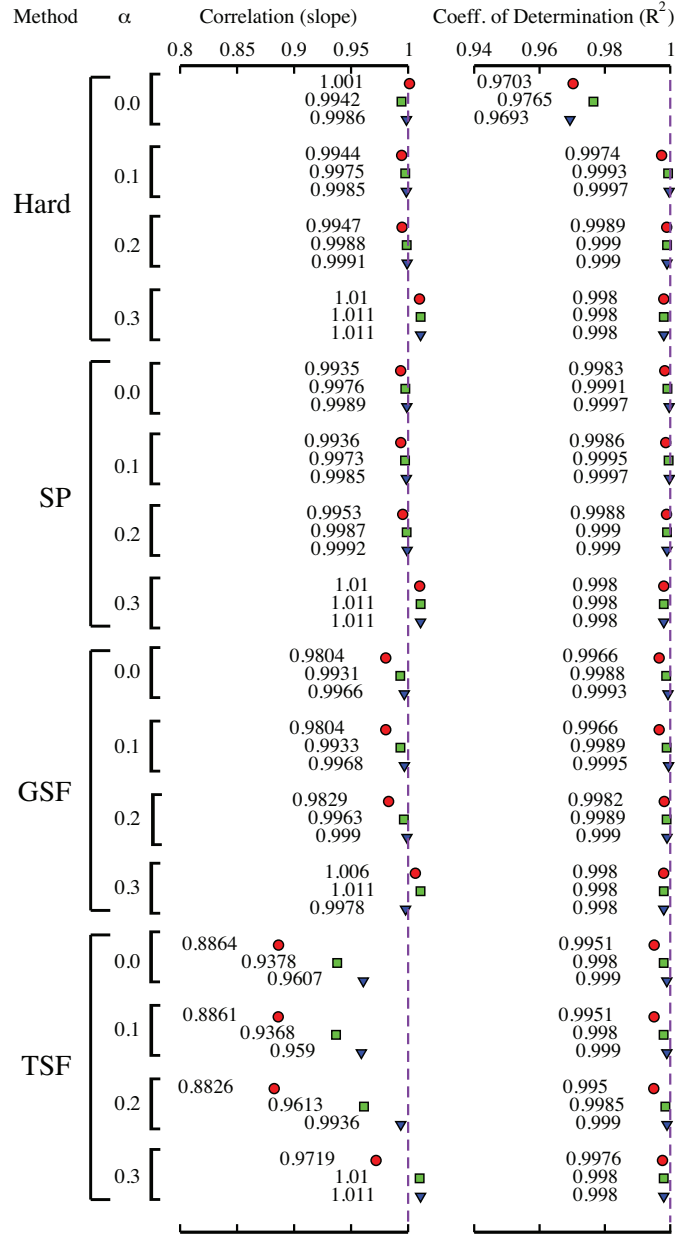


Figure 3.2. Statistical analysis of the quality of configurational energy differences for the real-space electrostatic methods compared with the reference Ewald sum. Results with a value equal to 1 (dashed line) indicate ΔE values indistinguishable from those obtained using the multipolar Ewald sum. Different values of the cutoff radius are indicated with different symbols (9 Å = circles, 12 Å = squares, and 15 Å = inverted triangles).

3.3.2 Magnitude of the force and torque vectors

The comparisons of the magnitudes of the forces and torques for the data accumulated from all six systems are shown in Fig. 3.3 and 3.4. The correlation and slope for the forces agree well with the Ewald sum even for the hard cutoffs.

For systems of molecules with only multipolar interactions, the pair energy contributions are quite short ranged. Moreover, the force decays more rapidly than the electrostatic energy, hence the hard cutoff method can also produce reasonable agreement for this quantity. Although the pure cutoff gives reasonably good electrostatic forces for pairs of molecules included within each other’s cutoff spheres, the discontinuity in the force at the cutoff radius can potentially cause energy conservation problems as molecules enter and leave the cutoff spheres. This is discussed in detail in section 3.3.4.

The two shifted-force methods (GSF and TSF) exhibit a small amount of systematic variation and scatter compared with the Ewald forces. The shifted-force models intentionally perturb the forces between pairs of molecules inside each other’s cutoff spheres in order to correct the energy conservation issues, and this perturbation is evident in the statistics accumulated for the molecular forces. The GSF perturbations are minimal, particularly for moderate damping and commonly-used cutoff values ($r_c = 12 \text{ \AA}$). The TSF method shows reasonable agreement in R^2 , but again the systematic error in the forces is concerning if replication of Ewald forces is desired.

It is important to note that the forces and torques from the SP and the Hard cutoffs are not identical. The SP method shifts each orientational contribution separately (e.g. the dipole-dipole dot product is shifted by a different function than the dipole-distance products), while the hard cutoff contains no orientation-

dependent shifting. The forces and torques for these methods therefore diverge for multipoles even though the forces for point charges are identical.

The torques (Fig. 3.4) appear to be significantly influenced by the choice of real-space method. The torque expressions have the same distance dependence as the energies, which are naturally longer-ranged expressions than the inter-site forces. Torques are also quite sensitive to orientations of neighboring molecules, even those that are near the cutoff distance.

The results shows that the torque from the hard cutoff method reproduces the torques in quite good agreement with the Ewald sum. The other real-space methods can cause some deviations, but excellent agreement with the Ewald sum torques is recovered at moderate values of the damping coefficient ($\alpha \approx 0.2 \text{ \AA}^{-1}$) and cutoff radius ($r_c \geq 12 \text{ \AA}$). The TSF method exhibits only fair agreement in the slope when compared with the Ewald torques even for larger cutoff radii. It appears that the severity of the perturbations in the TSF method are most in evidence for the torques.

3.3.3 Directionality of the force and torque vectors

The accurate evaluation of force and torque directions is just as important for molecular dynamics simulations as the magnitudes of these quantities. Force and torque vectors for all six systems were analyzed using Fisher statistics, and the quality of the vector directionality is shown in terms of circular variance ($\text{Var}(\theta)$) in Fig. 3.5. The force and torque vectors from the new real-space methods exhibit nearly-ideal Fisher probability distributions (Eq. 3.1). Both the hard and SP cutoff methods exhibit the best vectorial agreement with the Ewald sum. The force and torque vectors from GSF method also show good agreement with the

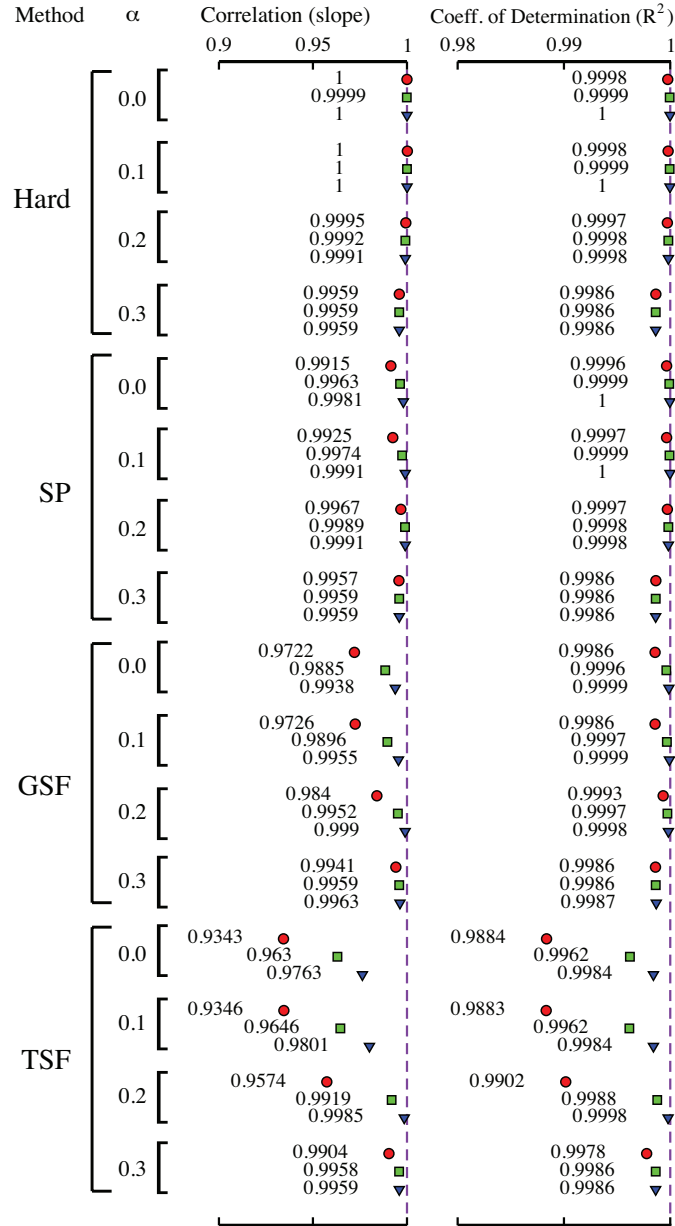


Figure 3.3. Statistical analysis of the quality of the force vector magnitudes for the real-space electrostatic methods compared with the reference Ewald sum. Results with a value equal to 1 (dashed line) indicate force magnitude values indistinguishable from those obtained using the multipolar Ewald sum. Different values of the cutoff radius are indicated with different symbols (9 Å = circles, 12 Å = squares, and 15 Å = inverted triangles).

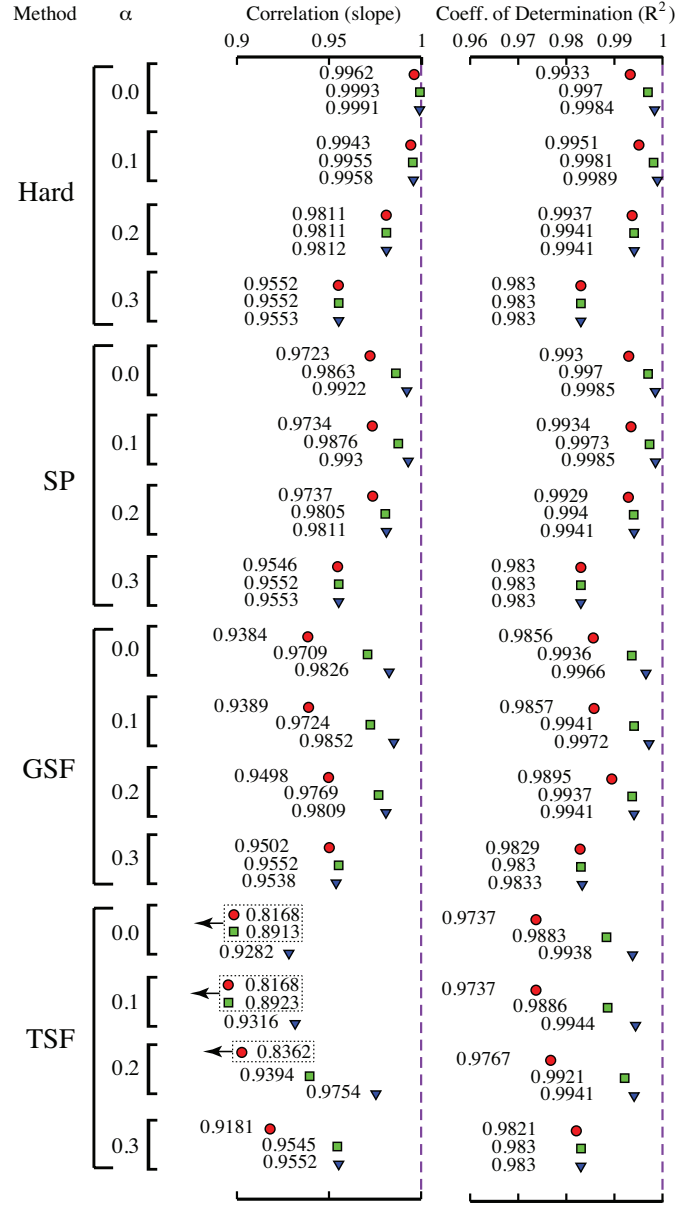


Figure 3.4. Statistical analysis of the quality of the torque vector magnitudes for the real-space electrostatic methods compared with the reference Ewald sum. Results with a value equal to 1 (dashed line) indicate force magnitude values indistinguishable from those obtained using the multipolar Ewald sum. Different values of the cutoff radius are indicated with different symbols (9 Å = circles, 12 Å = squares, and 15 Å = inverted triangles).

Ewald method, which can also be systematically improved by using moderate damping and a reasonable cutoff radius. For $\alpha = 0.2 \text{ \AA}^{-1}$ and $r_c = 12 \text{ \AA}$, we observe $\text{Var}(\theta) = 0.00206$, which corresponds to a distribution with 95% of force vectors within 6.37° of the corresponding Ewald forces. The TSF method produces the poorest agreement with the Ewald force directions.

Torques are again more perturbed than the forces by the new real-space methods, but even here the variance is reasonably small. For the same method (GSF) with the same parameters ($\alpha = 0.2 \text{ \AA}^{-1}$, $r_c = 12 \text{ \AA}$), the circular variance was 0.01415, corresponds to a distribution which has 95% of torque vectors are within 16.75° of the Ewald results. Again, the direction of the force and torque vectors can be systematically improved by varying α and r_c .

3.3.4 Energy conservation

We have tested the conservation of energy one can expect to see with the new real-space methods using the soft DQ liquid model with a small fraction of solvated ions. This is a test system which exercises all orders of multipole-multipole interactions derived in the chapter 2 in this series and provides the most comprehensive test of the new methods. A liquid-phase system was created with 2000 liquid-phase molecules and 48 dissolved ions at a density of 0.98 g cm^{-3} and a temperature of 300K. After equilibration in the canonical (NVT) ensemble using a Nosé-Hoover thermostat, six statistically-independent replicas of this liquid-phase system were run in the microcanonical (NVE) ensemble under the Ewald, Hard, SP, GSF, and TSF methods with a cutoff radius of 12 \AA . The value of the damping coefficient was also varied from the undamped case ($\alpha = 0$) to a heavily damped case ($\alpha = 0.3 \text{ \AA}^{-1}$) for all of the real space methods. A sample was also run using

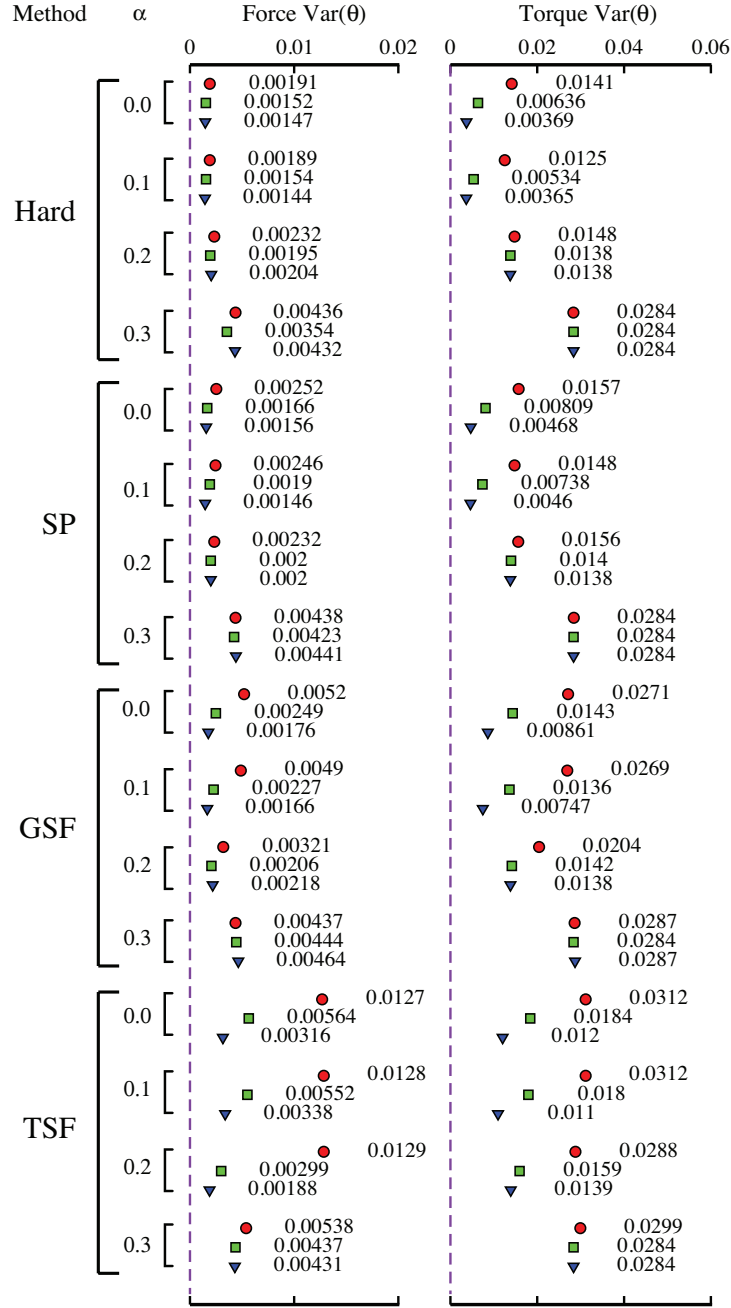


Figure 3.5. The circular variance of the direction of the force and torque vectors obtained from the real-space methods around the reference Ewald vectors. A variance equal to 0 (dashed line) indicates direction of the force or torque vectors are indistinguishable from those obtained from the Ewald sum. Here different symbols represent different values of the cutoff radius (9 Å = circle, 12 Å = square, 15 Å = inverted triangle)

the multipolar Ewald sum with the same real-space cutoff.

In Fig. 3.6 we show the both the linear drift in energy over time, δE_1 , and the standard deviation of energy fluctuations around this drift δE_0 . Both of the shifted-force methods (GSF and TSF) provide excellent energy conservation (drift less than 10^{-5} kcal / mol / ns / particle), while the hard cutoff is essentially unusable for molecular dynamics. SP provides some benefit over the hard cutoff because the energetic jumps that happen as particles leave and enter the cutoff sphere are somewhat reduced, but like the Wolf method for charges, the SP method would not be as useful for molecular dynamics as either of the shifted-force methods.

We note that for all tested values of the cutoff radius, the new real-space methods can provide better energy conservation behavior than the multipolar Ewald sum, even when relatively large k -space cutoff values are utilized.

3.3.5 Reproduction of Structural & Dynamical Features

The most important test of the modified interaction potentials is the fidelity with which they can reproduce structural features and dynamical properties in a liquid. One commonly-utilized measure of structural ordering is the pair distribution function, $g(r)$, which measures local density deviations in relation to the bulk density. In the electrostatic approaches studied here, the short-range repulsion from the Lennard-Jones potential is identical for the various electrostatic methods, and since short range repulsion determines much of the local liquid ordering, one would not expect to see many differences in $g(r)$. Indeed, the pair distributions are essentially identical for all of the electrostatic methods studied (for each of the different systems under investigation).

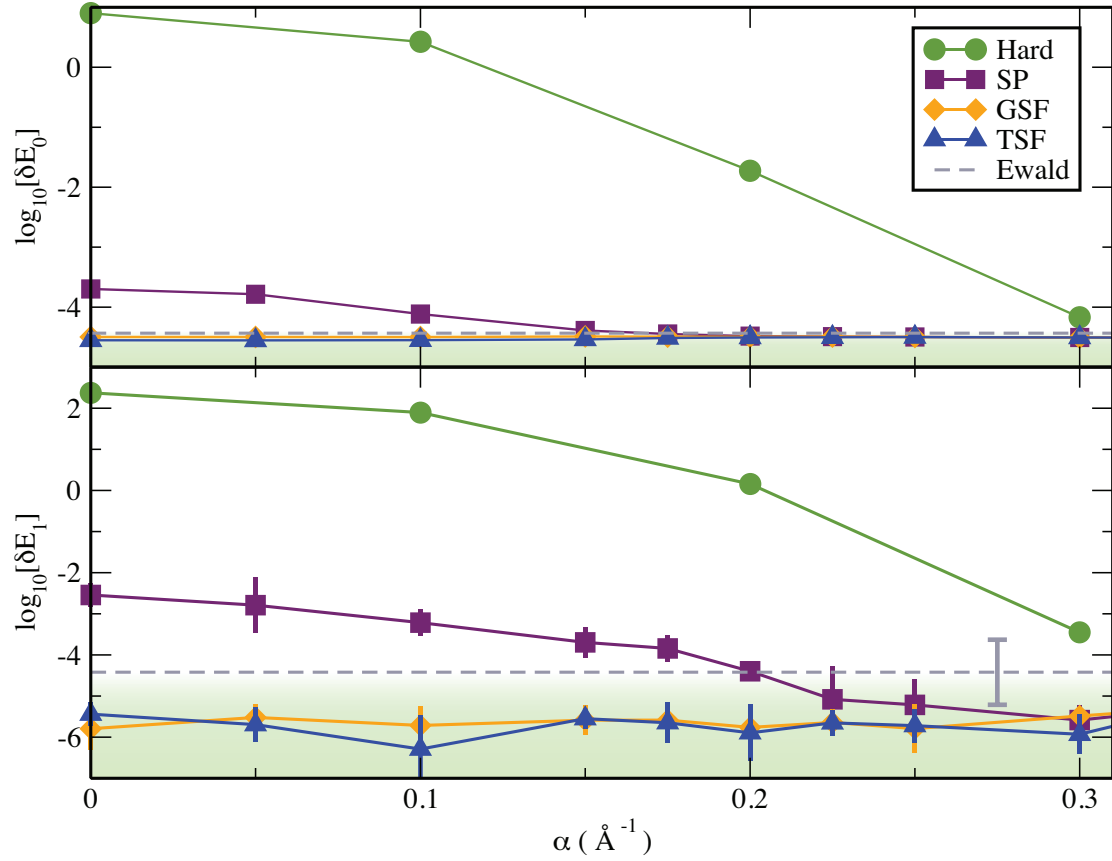


Figure 3.6. Energy conservation of the real-space methods for the soft DQ liquid / ion system. δE_1 is the linear drift in energy over time (in kcal/mol/particle/ns) and δE_0 is the standard deviation of energy fluctuations around this drift (in kcal/mol/particle). Points that appear in the green region at the bottom exhibit better energy conservation than would be obtained using common parameters for Ewald-based electrostatics.

There is a minor over-structuring of the first solvation shell when using TSF or when overdamping with any of the real-space methods. With moderate damping, GSF and SP produce pair distributions that are identical (within numerical noise) to their Ewald counterparts. The degree of over-structuring can be measured most easily using the coordination number,

$$n_C = 4\pi\rho \int_0^a r^2 g(r) dr, \quad (3.5)$$

where ρ is the number density of the site-site pair interactions, and a is the radial location of the minima following the first peak in $g(r)$ ($a = 4.2$ Å for the soft DQ liquid / ion system). The coordination number is shown as a function of the damping coefficient for all of the real space methods in Fig. 3.7.

A more demanding test of modified electrostatics is the average value of the electrostatic energy $\langle U_{\text{elect}} \rangle / N$ which is obtained by sampling the liquid-state configurations experienced by a liquid evolving entirely under the influence of each of the methods. In Fig. 3.7 we demonstrate how $\langle U_{\text{elect}} \rangle / N$ varies with the damping parameter, α , for each of the methods.

As in the crystals studied in the chapter 2, damping is important for converging the mean electrostatic energy values, particularly for the two shifted force methods (GSF and TSF). A value of $\alpha \approx 0.2$ Å⁻¹ is sufficient to converge the SP and GSF energies with a cutoff of 12 Å, while shorter cutoffs require more dramatic damping ($\alpha \approx 0.28$ Å⁻¹ for $r_c = 9$ Å). Overdamping the real-space electrostatic methods occurs with $\alpha > 0.3$ Å⁻¹, causing the estimate of the electrostatic energy to drop below the Ewald results.

These “optimal” values of the damping coefficient for structural features are similar to those observed for DSF electrostatics for purely point-charge systems,

and the range $\alpha = 0.175 \rightarrow 0.225 \text{ \AA}^{-1}$ for $r_c = 12 \text{ \AA}$ appears to be an excellent compromise for mixed charge/multipolar systems.

To test the fidelity of the electrostatic methods at reproducing *dynamics* in a multipolar liquid, it is also useful to look at transport properties, particularly the diffusion constant,

$$D = \lim_{t \rightarrow \infty} \frac{1}{6t} \langle |\mathbf{r}(t) - \mathbf{r}(0)|^2 \rangle \quad (3.6)$$

which measures long-time behavior and is sensitive to the forces on the multipoles. The self-diffusion constants (D) were calculated from linear fits to the long-time portion of the mean square displacement, $\langle r^2(t) \rangle$. [22] In Fig. 3.7 we demonstrate how the diffusion constant depends on the choice of real-space methods and the damping coefficient. Both the SP and GSF methods can obtain excellent agreement with Ewald again using moderate damping.

In addition to translational diffusion, orientational relaxation times were calculated for comparisons with the Ewald simulations and with experiments. These values were determined by calculating the orientational time correlation function,

$$C_l^\gamma(t) = \left\langle P_l \left[\hat{\mathbf{A}}_\gamma(t) \cdot \hat{\mathbf{A}}_\gamma(0) \right] \right\rangle, \quad (3.7)$$

from the same 350 ps microcanonical trajectories that were used for translational diffusion. Here, P_l is the Legendre polynomial of order l and $\hat{\mathbf{A}}_\gamma$ is the unit vector for body axis γ . The reference frame used for our sample dipolar systems has the z -axis running along the dipoles, and for the soft DQ liquid model, the y -axis connects the two implied hydrogen-like positions. From the orientation autocorrelation functions, we can obtain time constants for rotational relaxation either by fitting to a multi-exponential model for the orientational relaxation, or by integrating the correlation functions.

In a good model for water, the orientational decay times would be comparable to water orientational relaxation times from nuclear magnetic resonance (NMR). The relaxation constant obtained from $C_2^y(t)$ is normally of experimental interest because it describes the relaxation of the principle axis connecting the hydrogen atoms. Thus, $C_2^y(t)$ can be compared to the intermolecular portion of the dipole-dipole relaxation from a proton NMR signal and can provide an estimate of the NMR relaxation time constant.[78] In Fig. 3.7 we compare the τ_2^y and τ_2^z values for the various real-space methods over a range of different damping coefficients. The rotational relaxation for the z axis primarily probes the torques on the dipoles, while the relaxation for the y axis is sensitive primarily to the quadrupolar torques.

In Fig. 3.7 it appears that values for D , τ_2^y , and τ_2^z using the Ewald sum are reproduced with excellent fidelity by the GSF and SP methods. All of the real space methods can be *overdamped*, which reduces the effective range of multipole interactions, causing structural and dynamical changes from the correct behavior. Because overdamping weakens orientational preferences between adjacent molecules, it manifests as too-rapid orientational decay coupled with faster diffusion and over-coordination of the liquid. Underdamping is less problematic for the SP and GSF methods, as their structural and dynamical properties still reproduce the Ewald results even in the completely undamped ($\alpha = 0$) case. An optimal range for the electrostatic damping parameter appears to be $\alpha = 0.175 \rightarrow 0.225 \text{ \AA}^{-1}$ for $r_c = 12 \text{ \AA}$, which is similar to the optimal range found for the damped shifted force potential for point charges.[15]

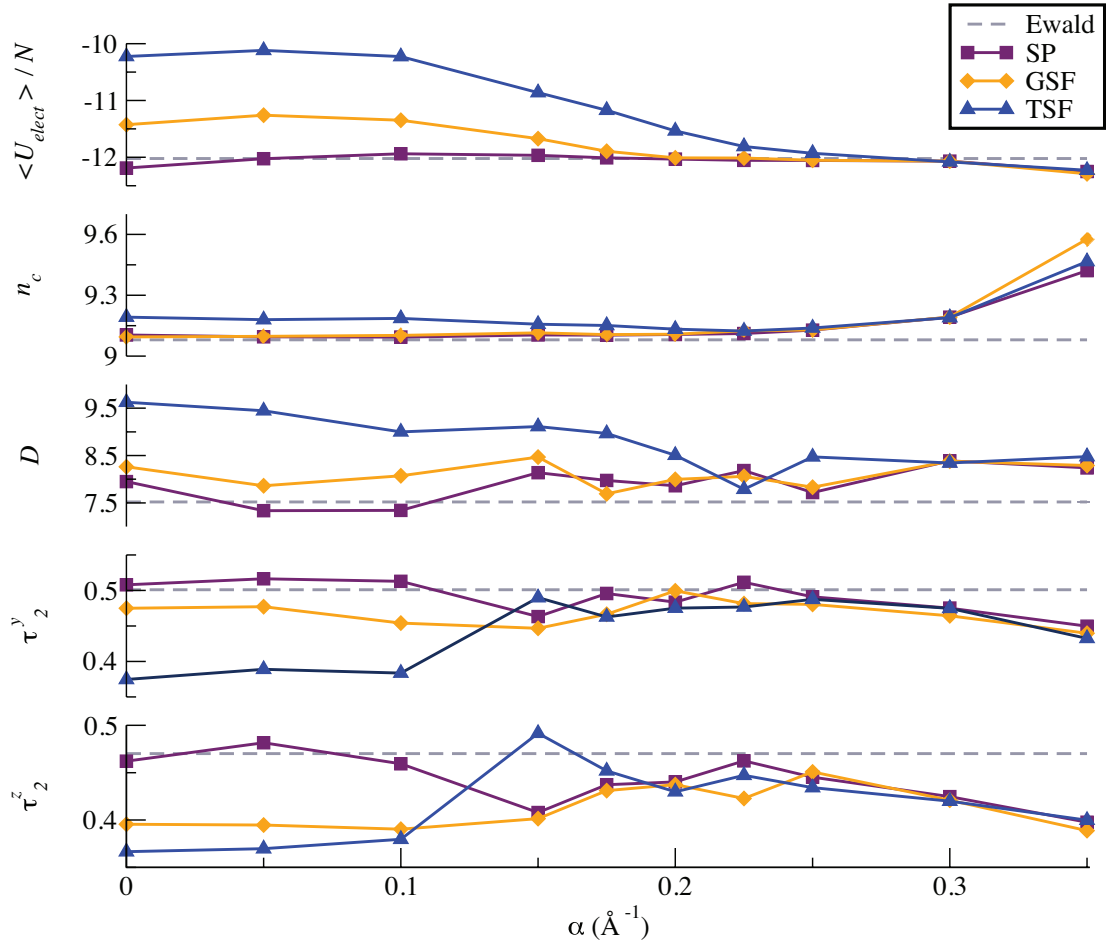


Figure 3.7. Comparison of the structural and dynamic properties for the combined multipolar liquid (soft DQ liquid + ions) for all of the real-space methods with $r_c = 12 \text{ \AA}$. Electrostatic energies, $\langle U_{\text{elect}} \rangle / N$ (in kcal / mol), coordination numbers, n_C , diffusion constants (in $10^{-5} \text{ cm}^2 \text{ s}^{-1}$), and rotational correlation times (in ps) all show excellent agreement with Ewald results for damping coefficients in the range $\alpha = 0.175 \rightarrow 0.225 \text{ \AA}^{-1}$.

3.4 Summary

In the chapter 2, we generalized the charge-neutralized electrostatic energy originally developed by Wolf *et al.*[16] to multipole-multipole interactions up to quadrupolar order. The SP method is essentially a multipole-capable version of the Wolf model. The SP method for multipoles provides excellent agreement with Ewald-derived energies, forces and torques, and is suitable for Monte Carlo simulations, although the forces and torques retain discontinuities at the cutoff distance that prevents its use in molecular dynamics.

We also developed two natural extensions of the damped shifted-force (DSF) model originally proposed by Zahn *et al.* and extended by Fennell and Gezelter.[15, 17] The GSF and TSF approaches provide smooth truncation of energies, forces, and torques at the real-space cutoff, and both converge to DSF electrostatics for point-charge interactions. The TSF model is based on a high-order truncated Taylor expansion which can be relatively perturbative inside the cutoff sphere. The GSF model takes the gradient from an images of the interacting multipole that has been projected onto the cutoff sphere to derive shifted force and torque expressions, and is a significantly more gentle approach.

The GSF method produces quantitative agreement with Ewald energies, forces, and torques. It also performs well in conserving energy in MD simulations. The Taylor-shifted (TSF) model provides smooth dynamics, but these take place on a potential energy surface that is significantly perturbed from Ewald-based electrostatics. Because it performs relatively poorly compared with GSF, it may seem odd that the TSF model was included in this work. However, the functional forms derived for the SP and GSF methods depend on the separation of orientational contributions that were made visible by the Taylor series of the electrostatic

kernel at the cutoff radius. The TSF method also has the unique property that a large number of derivatives can be made to vanish at the cutoff radius. This property has proven useful in past treatments of the corrections to the Clausius-Mossotti fluctuation formula for dielectric constants.[37]

Reproduction of both structural and dynamical features in the liquid systems is remarkably good for both the SP and GSF models. Pair distribution functions are essentially equivalent to the same functions produced using Ewald-based electrostatics, and with moderate damping, a structural feature that directly probes the electrostatic interaction (e.g. the mean electrostatic potential energy) can also be made quantitative. Dynamical features are sensitive probes of the forces and torques produced by these methods, and even though the smooth behavior of forces is produced by perturbing the overall potential, the diffusion constants and orientational correlation times are quite close to the Ewald-based results.

The only cases we have found where the new GSF and SP real-space methods can be problematic are those which retain a bulk dipole moment at large distances (e.g. the Z_1 dipolar lattice). In ferroelectric materials, uniform weighting of the orientational contributions can be important for converging the total energy. In these cases, the damping function which causes the non-uniform weighting can be replaced by the bare electrostatic kernel, and the energies return to the expected converged values.

Based on the results of this work, we can conclude that the GSF method is a suitable and efficient replacement for the Ewald sum for evaluating electrostatic interactions in modern MD simulations, and the SP method would be an excellent choice for Monte Carlo simulations where smooth forces and energy conservation are not important. Both the SP and GSF methods retain excellent fidelity to the

Ewald energies, forces and torques. Additionally, the energy drift and fluctuations from the GSF electrostatics are significantly better than a multipolar Ewald sum for finite-sized reciprocal spaces, and physical properties are reproduced accurately.

As in all purely pairwise cutoff methods, the SP, GSF and TSF methods are expected to scale approximately *linearly* with system size, and are easily parallelizable. This should result in substantial reductions in the computational cost of performing large simulations. With the proper use of pre-computation and spline interpolation of the radial functions, the real-space methods are essentially the same cost as a simple real-space cutoff. They require no Fourier transforms or k -space sums, and guarantee the smooth handling of energies, forces, and torques as multipoles cross the real-space cutoff boundary.

We are not suggesting that there is any flaw with the Ewald sum; in fact, it is the standard by which the SP, GSF, and TSF methods have been judged in this work. However, these results provide evidence that in the typical simulations performed today, the Ewald summation may no longer be required to obtain the level of accuracy most researchers have come to expect.

CHAPTER 4

DIELECTRIC PROPERTIES

In the chapter 3, I have presented various physical properties calculated using SP, GSF,TSF, and Ewald methods. This chapter reports on the fluctuation, perturbation, and potential of mean force (PMF) methods for calculating dielectric properties for dipolar and quadrupolar fluids. Since the dielectric constant is a macroscopic property, interactions of a molecule with the all of the molecules in the system should be considered. But the real space methods utilize a cutoff radius and ignores the interaction beyond cutoff radius. Hence the formula for calculating dielectric constant should be modified accordingly. To evaluate correct dielectric properties from the simulation, we have to take account of correction factor for each real-space methods. In this chapter, I have also presented the correction factor required for the calculation of the dielectric properties for dipolar and quadrupolar fluids.

4.1 Introduction

One of the most stringent tests of any new electrostatic method is the fidelity with which that method can reproduce the bulk-phase polarizability or equivalently, the dielectric properties of a fluid. Before the advent of computer simulations, Kirkwood and Onsager developed fluctuation formulae for the dielec-

tric properties of dipolar fluids.[79, 80] Along with projections of the frequency-dependent dielectric to zero frequency, these fluctuation formulae are now widely used to predict the static dielectric constant of simulated materials.

If we consider a system of dipolar or quadrupolar molecules under the influence of an external field or field gradient, the net polarization of the system will largely be proportional to the applied perturbation.[81–84] In simulations, the net polarization of the system is also determined by the interactions *between* the molecules. Therefore the macroscopic polarizability obtained from a simulation depends on the details of the electrostatic interaction methods that were employed in the simulation. To determine the relevant physical properties of the multipolar fluid from the system fluctuations, the interactions between molecules must be incorporated into the formalism for the bulk properties.

In most simulations, bulk materials are treated using periodic replicas of small regions, and this level of approximation requires corrections to the fluctuation formulae that were derived for the bulk fluids. In 1983 Neumann proposed a general formula for evaluating dielectric properties of dipolar fluids using both Ewald and real-space cutoff methods.[2] Steihauser and Neumann used this formula to evaluate the corrected dielectric constant for the Stockmayer fluid using two different methods: Ewald-Kornfeld (EK) and reaction field (RF) methods.[85]

Zahn *et al.*[17] utilized this approach and evaluated the correction factor for using damped shifted charge-charge kernel. This was later generalized by Izvekov *et al.*,[37] who noted that the expression for the dielectric constant reduces to widely-used conducting boundary formula for real-space methods that have first derivatives that vanish at the cutoff radius.

One of the primary topics of this chapter is the derivation of correction factors

for the three new real space methods. We find that the correction formulae for dipolar molecules depends not only on the methodology being used, but also on whether the molecular dipoles are treated using point charges or point dipoles. We derive correction factors for both cases.

In quadrupolar fluids, the relationship between quadrupolar susceptibility and the dielectric constant is not as straightforward as in the dipolar case. The effective dielectric constant depends on the geometry of the external (or internal) field perturbation.[86] Significant efforts have been made to increase our understanding the dielectric properties of these fluids,[81, 87, 88] although a general correction formula has not yet been developed.

In this chapter, we derive general formulae for calculating the quadrupolar susceptibility of quadrupolar fluids. We also evaluate the correction factor for SP, GSF, and TSF methods for quadrupolar fluids interacting via point charges, point dipoles or directly through quadrupole-quadrupole interactions.

We also calculate the screening behavior for two ions immersed in multipolar fluids to estimate the distance dependence of charge screening in both dipolar and quadrupolar fluids. We use three distinct methods to compare our analytical results with computer simulations:

1. responses of the fluid to external perturbations,
2. fluctuations of system multipole moments, and
3. potentials of mean force between solvated ions,

Under the influence of weak external fields, the bulk polarization of the system is primarily a linear response to the perturbation, where proportionality constant depends on the electrostatic interactions between the multipoles. The fluctuation

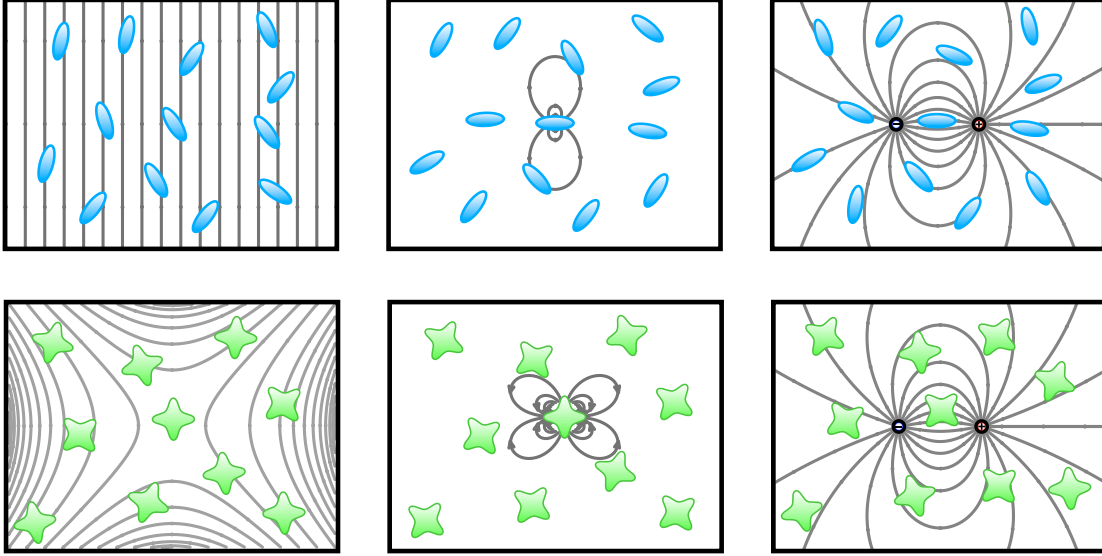


Figure 4.1. Dielectric properties of a fluid measure the response to external electric fields and gradients (left), or internal fields and gradients generated by the molecules themselves (center), or fields produced by embedded ions (right). The dielectric constant (ϵ) measures all three responses in dipolar fluids (top). In quadrupolar liquids (bottom), the relevant bulk property is the quadrupolar susceptibility (χ_Q), and the geometry of the field determines the effective dielectric screening.

formulae connect bulk properties of the fluid to equilibrium fluctuations in the system multipolar moments during a simulation. These fluctuations also depend on the form of the electrostatic interactions between molecules. Therefore, the connections between the actual bulk properties and both the computed fluctuation and external field responses must be modified accordingly.

The potential of mean force (PMF) allows calculation of an effective dielectric constant or screening factor from the potential energy between ions before and after dielectric material is introduced. Computing the PMF between embedded point charges is an additional check on the bulk properties computed via the other two methods.

4.2 Dipolar Fluids and the Dielectric Constant

Dielectric properties of a fluid arise mainly from responses of the fluid to either applied fields or transient fields internal to the fluid. In response to an applied field, the molecules have electronic polarizabilities, changes to internal bond lengths, and reorientations towards the direction of the applied field. There is an added complication that in the presence of external field, the perturbation experienced by any single molecule is not only due to external field but also to the fields produced by the all other molecules in the system.

4.2.1 Response to External Perturbations

In the presence of uniform electric field \mathbf{E} , an individual molecule with a permanent dipole moment p_o will realign along the direction of the field with an

average polarization given by

$$\langle \mathbf{p} \rangle = \epsilon_0 \alpha_p \mathbf{E}, \quad (4.1)$$

where $\alpha_p = p_o^2 / 3\epsilon_0 k_B T$ is the contribution to molecular polarizability due solely to reorientation dynamics. Because the applied field must overcome thermal motion, the orientational polarization depends inversely on the temperature.

Likewise, a condensed phase system of permanent dipoles will also polarize along the direction of an applied field. The polarization density of the system is

$$\mathbf{P} = \epsilon_0 \alpha_D \mathbf{E}. \quad (4.2)$$

The constant α_D is the macroscopic polarizability, which is an emergent property of the dipolar fluid. Note that the polarizability, α_D is distinct from the dipole susceptibility, χ_D , which is the quantity most directly related to the static dielectric constant, $\epsilon = 1 + \chi_D$.

4.2.2 Fluctuation Formula

For a system of dipolar molecules at thermal equilibrium, we can define both a system dipole moment, $\mathbf{M} = \sum_i \mathbf{p}_i$ as well as a dipole polarization density, $\mathbf{P} = \langle \mathbf{M} \rangle / V$.

In the presence of applied field \mathbf{E} , the polarization density can be expressed in terms of fluctuations in the net dipole moment,

$$\mathbf{P} = \epsilon_0 \frac{\langle \mathbf{M}^2 \rangle - \langle \mathbf{M} \rangle^2}{3\epsilon_0 V k_B T} \mathbf{E} \quad (4.3)$$

This has structural similarity with the Boltzmann average for the polarization of a single molecule. Here $\langle \mathbf{M}^2 \rangle - \langle \mathbf{M} \rangle^2$ measures fluctuations in the net dipole moment,

$$\langle \mathbf{M}^2 \rangle - \langle \mathbf{M} \rangle^2 = \langle M_x^2 + M_y^2 + M_z^2 \rangle - (\langle M_x \rangle^2 + \langle M_y \rangle^2 + \langle M_z \rangle^2). \quad (4.4)$$

For the limiting case $\mathbf{E} \rightarrow 0$, the ensemble average of both the net dipole moment $\langle \mathbf{M} \rangle$ and dipolar polarization \mathbf{P} tends to vanish but $\langle \mathbf{M}^2 \rangle$ does not. The macroscopic dipole polarizability can therefore be written as,

$$\alpha_D = \frac{\langle \mathbf{M}^2 \rangle - \langle \mathbf{M} \rangle^2}{3\epsilon_o V k_B T} \quad (4.5)$$

This relationship between a macroscopic property of dipolar material and microscopic fluctuations is true even when the applied field $\mathbf{E} \rightarrow 0$.

4.2.3 Correction Factors

In the presence of a uniform external field \mathbf{E}° , the total electric field at \mathbf{r} depends on the polarization density at all other points in the system,[2]

$$\mathbf{E}(\mathbf{r}) = \mathbf{E}^\circ(\mathbf{r}) + \frac{1}{4\pi\epsilon_o} \int d\mathbf{r}' \mathbf{T}(\mathbf{r} - \mathbf{r}') \cdot \mathbf{P}(\mathbf{r}'). \quad (4.6)$$

\mathbf{T} is the dipole interaction tensor connecting dipoles at \mathbf{r}' with the point of interest (\mathbf{r}).

In simulations of dipolar fluids, the molecular dipoles may be represented either by closely-spaced point charges or by point dipoles (see Fig. 4.2). In the case where point charges are interacting via an electrostatic kernel, $v(r)$, the effective

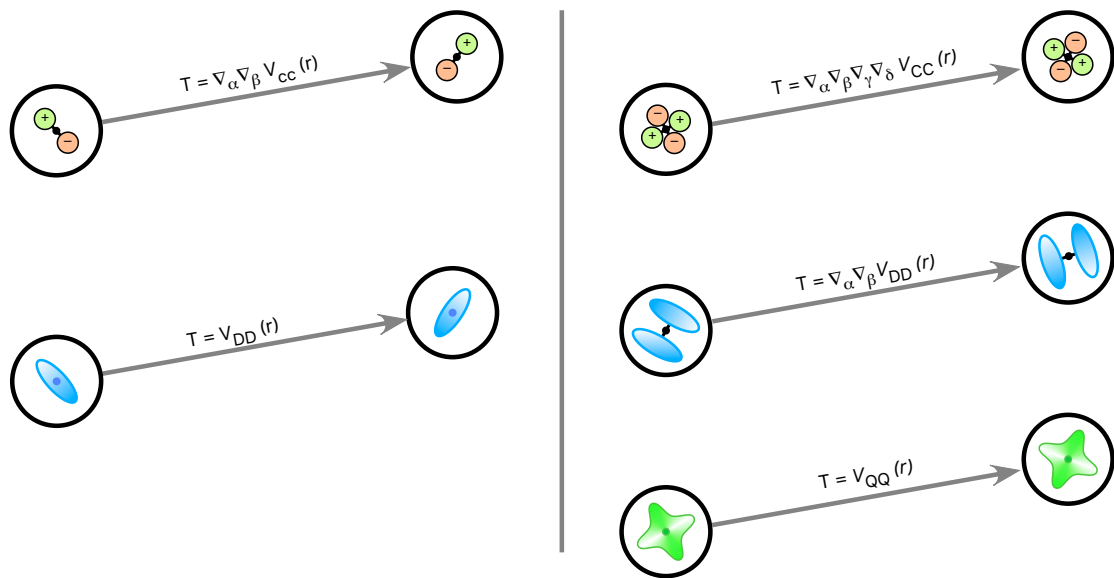


Figure 4.2. In the real-space electrostatic methods, the molecular dipole tensor, $\mathbf{T}_{\alpha\beta}(r)$, is not the same for charge-charge interactions as for point dipoles (left panel). The same holds true for the molecular quadrupole tensor (right panel), $\mathbf{T}_{\alpha\beta\gamma\delta}(r)$, which can have distinct forms if the molecule is represented by charges, dipoles, or point quadrupoles.

molecular dipole tensor, \mathbf{T} is obtained from two successive applications of the gradient operator to the electrostatic kernel,

$$\mathbf{T}_{\alpha\beta}(r) = \nabla_\alpha \nabla_\beta (v(r)) \quad (4.7)$$

$$= \delta_{\alpha\beta} \left(\frac{1}{r} v'(r) \right) + \frac{r_\alpha r_\beta}{r^2} \left(v''(r) - \frac{1}{r} v'(r) \right) \quad (4.8)$$

where $v(r)$ may be either the bare kernel ($1/r$) or one of the modified (Wolf or DSF) kernels. This tensor describes the effective interaction between molecular dipoles (\mathbf{D}) in Gaussian units as $-\mathbf{D} \cdot \mathbf{T} \cdot \mathbf{D}$.

When utilizing any of the three new real-space methods for point *dipoles*, the tensor is explicitly constructed,

$$\mathbf{T}_{\alpha\beta}(r) = \delta_{\alpha\beta} v_{21}(r) + \frac{r_\alpha r_\beta}{r^2} v_{22}(r) \quad (4.9)$$

where the functions $v_{21}(r)$ and $v_{22}(r)$ depend on the level of the approximation.[62, 89] Although the Taylor-shifted (TSF) and gradient-shifted (GSF) models produce to the same $v(r)$ function for point charges, they have distinct forms for the dipole-dipole interaction.

Using a constitutive relation, the polarization density $\mathbf{P}(\mathbf{r})$ is given by,

$$\mathbf{P}(\mathbf{r}) = \epsilon_o \chi_D \left(\mathbf{E}^\circ(\mathbf{r}) + \frac{1}{4\pi\epsilon_o} \int d\mathbf{r}' \mathbf{T}(\mathbf{r} - \mathbf{r}') \cdot \mathbf{P}(\mathbf{r}') \right). \quad (4.10)$$

Note that χ_D explicitly depends on the details of the dipole interaction tensor. Neumann *et al.* [2, 85, 90, 91] derived an elegant way to modify the fluctuation formula to correct for approximate interaction tensors. This correction was derived using a Fourier representation of the interaction tensor, $\tilde{\mathbf{T}}(\mathbf{k})$, and involves the

quantity,

$$A = \frac{3}{4\pi} \tilde{\mathbf{T}}(0) = \frac{3}{4\pi} \int_V d\mathbf{r} \mathbf{T}(\mathbf{r}) \quad (4.11)$$

which is the $k \rightarrow 0$ limit of $\tilde{\mathbf{T}}$. Using this quantity (originally called Q in Refs. [2, 85, 90, 91]), the dielectric constant can be computed

$$\epsilon = \frac{3 + (A + 2)(\epsilon_{CB} - 1)}{3 + (A - 1)(\epsilon_{CB} - 1)} \quad (4.12)$$

where ϵ_{CB} is the widely-used conducting boundary expression for the dielectric constant,

$$\epsilon_{CB} = 1 + \frac{\langle \mathbf{M}^2 \rangle - \langle \mathbf{M} \rangle^2}{3\epsilon_o V k_B T} = 1 + \alpha_D \quad (4.13)$$

Eqs. (4.12) and (4.13) allows estimation of the static dielectric constant from fluctuations easily computed directly from simulations.

We have utilized the Neumann *et al.* approach for the three new real-space methods, and obtain method-dependent correction factors. The expression for the correction factor also depends on whether the simulation involves point charges or point dipoles to represent the molecular dipoles. These corrections factors are listed in Table 4.1. We note that the GSF correction factor for point dipoles has been independently derived by Stenqvist *et al.*[92]

Note that for point charges, the GSF and TSF methods produce estimates of the dielectric that need no correction, and the TSF method likewise needs no correction for point dipoles.

TABLE 4.1: Expressions for the dipolar correction factor (A) for the real-space electrostatic methods in terms of the damping parameter (α) and the cutoff radius (r_c). The Ewald-Kornfeld result derived in Refs.[1–3] is shown for comparison using the Ewald convergence parameter (κ) and the real-space cutoff value (r_c).

Method	Molecular Representation	
	point charges	point dipoles
Shifted Potential (SP)	$\text{erf}(r_c \alpha) - \frac{2\alpha r_c}{\sqrt{\pi}} e^{-\alpha^2 r_c^2}$	$\text{erf}(r_c \alpha) - \frac{2\alpha r_c}{\sqrt{\pi}} \left(1 + \frac{2\alpha^2 r_c^2}{3}\right) e^{-\alpha^2 r_c^2}$
Gradient-shifted (GSF)	1	$\text{erf}(\alpha r_c) - \frac{2\alpha r_c}{\sqrt{\pi}} \left(1 + \frac{2\alpha^2 r_c^2}{3} + \frac{\alpha^4 r_c^4}{3}\right) e^{-\alpha^2 r_c^2}$
Taylor-shifted (TSF)	1	1
Spherical Cutoff (SC)	$\text{erf}(r_c \alpha) - \frac{2\alpha r_c}{\sqrt{\pi}} e^{-\alpha^2 r_c^2}$	$\text{erf}(r_c \alpha) - \frac{2\alpha r_c}{\sqrt{\pi}} e^{-\alpha^2 r_c^2}$
Ewald-Kornfeld (EK)	$\text{erf}(r_c \kappa) - \frac{2\kappa r_c}{\sqrt{\pi}} e^{-\kappa^2 r_c^2}$	$\text{erf}(r_c \kappa) - \frac{2\kappa r_c}{\sqrt{\pi}} e^{-\kappa^2 r_c^2}$

4.3 Quadrupolar Fluids and the Quadrupolar Susceptibility

4.3.1 Response to External Perturbations

A molecule with a permanent quadrupole, \mathbf{q} , will align in the presence of an electric field gradient $\nabla \mathbf{E}$. The anisotropic polarization of the quadrupole is given by,[93, 94]

$$\langle \mathbf{q} \rangle - \frac{\mathbf{I}}{3} \text{Tr}(\mathbf{q}) = \epsilon_o \alpha_q \nabla \mathbf{E}, \quad (4.14)$$

where $\alpha_q = q_o^2/15\epsilon_o k_B T$ is a molecular quadrupole polarizability and q_o is an effective quadrupole moment for the molecule,

$$q_o^2 = 3\mathbf{q} : \mathbf{q} - \text{Tr}(\mathbf{q})^2. \quad (4.15)$$

In the presence of an external field gradient, a system of quadrupolar molecules also organizes with an anisotropic polarization,

$$\mathbf{Q} - \frac{\mathbf{I}}{3} \text{Tr}(\mathbf{Q}) = \epsilon_o \alpha_Q \nabla \mathbf{E} \quad (4.16)$$

where \mathbf{Q} is the traced quadrupole density of the system and α_Q is a macroscopic quadrupole polarizability which has dimensions of length^{-2} . Equivalently, the traceless form may be used,

$$\Theta = 3\epsilon_o \alpha_Q \nabla \mathbf{E}, \quad (4.17)$$

where $\Theta = 3\mathbf{Q} - \mathbf{I} \text{Tr}(\mathbf{Q})$ is the traceless tensor that also describes the system quadrupole density. It is this tensor that will be utilized to derive correction factors below.

4.3.2 Fluctuation Formula

As in the dipolar case, we may define a system quadrupole moment, $\mathbf{M}_Q = \sum_i \mathbf{q}_i$ and the traced quadrupolar density, $\mathbf{Q} = \mathbf{M}_Q/V$. A fluctuation formula can be written for a system comprising quadrupolar molecules,[95–97]

$$\mathbf{Q} - \frac{\mathbf{I}}{3}\text{Tr}(\mathbf{Q}) = \epsilon_o \frac{\langle \mathbf{M}_Q^2 \rangle - \langle \mathbf{M}_Q \rangle^2}{15\epsilon_o V k_B T} \nabla \mathbf{E}. \quad (4.18)$$

Some care is needed in the definitions of the averaged quantities. These refer to the effective quadrupole moment of the system, and they are computed as follows,

$$\langle \mathbf{M}_Q^2 \rangle = \langle 3\mathbf{M}_Q : \mathbf{M}_Q - \text{Tr}(\mathbf{M}_Q)^2 \rangle \quad (4.19)$$

$$\langle \mathbf{M}_Q \rangle^2 = 3 \langle \mathbf{M}_Q \rangle : \langle \mathbf{M}_Q \rangle - \text{Tr}(\langle \mathbf{M}_Q \rangle)^2 \quad (4.20)$$

The macroscopic quadrupolarizability is given by,

$$\alpha_Q = \frac{\langle \mathbf{M}_Q^2 \rangle - \langle \mathbf{M}_Q \rangle^2}{15\epsilon_o V k_B T} \quad (4.21)$$

This relationship between a macroscopic property of a quadrupolar fluid and microscopic fluctuations should be true even when the applied field gradient $\nabla \mathbf{E} \rightarrow 0$.

4.3.3 Correction Factors

In this section we generalize the treatment of Neumann *et al.* for quadrupolar fluids. Interactions involving multiple quadrupoles are rank 4 tensors, and we therefore describe quantities in this section using Einstein notation.

In the presence of a uniform external field gradient, $\partial_\alpha E_\beta^\circ$, the total field gradient at \mathbf{r} depends on the quadrupole polarization density at all other points in

the system,

$$\partial_\alpha E_\beta(\mathbf{r}) = \partial_\alpha E_\beta^\circ(\mathbf{r}) + \frac{1}{8\pi\epsilon_o} \int T_{\alpha\beta\gamma\delta}(\mathbf{r} - \mathbf{r}') Q_{\gamma\delta}(\mathbf{r}') d\mathbf{r}' \quad (4.22)$$

where $T_{\alpha\beta\gamma\delta}$ is the quadrupole interaction tensor connecting quadrupoles at \mathbf{r}' with the point of interest (\mathbf{r}).

In simulations of quadrupolar fluids, the molecular quadrupoles may be represented by closely-spaced point charges, by multiple point dipoles, or by a single point quadrupole (see Fig. 4.2). In the case where point charges are interacting via an electrostatic kernel, $v(r)$, the effective molecular quadrupole tensor can be obtained from four successive applications of the gradient operator to the electrostatic kernel,

$$\begin{aligned} T_{\alpha\beta\gamma\delta}(\mathbf{r}) &= \nabla_\alpha \nabla_\beta \nabla_\gamma \nabla_\delta v(r) \\ &= (\delta_{\alpha\beta}\delta_{\gamma\delta} + \delta_{\alpha\gamma}\delta_{\beta\delta} + \delta_{\alpha\delta}\delta_{\beta\gamma}) \left(-\frac{v'(r)}{r^3} + \frac{v''(r)}{r^2} \right) \\ &\quad + (\delta_{\alpha\beta}r_\gamma r_\delta + 5 \text{ permutations}) \left(\frac{3v'(r)}{r^5} - \frac{3v''(r)}{r^4} + \frac{v'''(r)}{r^3} \right) \\ &\quad + r_\alpha r_\beta r_\gamma r_\delta \left(-\frac{15v'(r)}{r^7} + \frac{15v''(r)}{r^6} - \frac{6v'''(r)}{r^5} + \frac{v''''(r)}{r^4} \right), \end{aligned} \quad (4.23)$$

$$(4.24)$$

where $v(r)$ can either be the electrostatic kernel ($1/r$) or one of the modified (Wolf or DSF) kernels.

Similarly, when representing quadrupolar molecules with multiple point *dipoles*, the molecular quadrupole interaction tensor can be obtained using two successive

applications of the gradient operator to the dipole interaction tensor,

$$T_{\alpha\beta\gamma\delta}(\mathbf{r}) = \nabla_\alpha \nabla_\beta T_{\gamma\delta}(\mathbf{r}) \quad (4.25)$$

$$\begin{aligned} &= \delta_{\alpha\beta}\delta_{\gamma\delta} \frac{v'_{21}(r)}{r} + (\delta_{\alpha\gamma}\delta_{\beta\delta} + \delta_{\alpha\delta}\delta_{\beta\gamma}) \frac{v_{22}(r)}{r^2} \\ &\quad + \delta_{\gamma\delta} r_\alpha r_\beta \left(\frac{v''_{21}(r)}{r^2} - \frac{v'_{21}(r)}{r^3} \right) \\ &\quad + (\delta_{\alpha\beta} r_\gamma r_\delta + \delta_{\alpha\gamma} r_\beta r_\delta + \delta_{\alpha\delta} r_\gamma r_\beta + \delta_{\beta\gamma} r_\alpha r_\delta + \delta_{\beta\delta} r_\alpha r_\gamma) \left(\frac{v'_{22}(r)}{r^3} - \frac{2v_{22}(r)}{r^4} \right) \\ &\quad + r_\alpha r_\beta r_\gamma r_\delta \left(\frac{v''_{22}(r)}{r^4} - \frac{5v'_{22}(r)}{r^5} + \frac{8v_{22}(r)}{r^6} \right), \end{aligned} \quad (4.26)$$

where $T_{\gamma\delta}(\mathbf{r})$ is a dipole-dipole interaction tensor that depends on the level of the approximation.[62, 89] Similarly $v_{21}(r)$ and $v_{22}(r)$ are the radial function for different real space cutoff methods defined in the Chapter 2.[62]

For quadrupolar liquids modeled using point quadrupoles, the interaction tensor can be constructed as,

$$\begin{aligned} T_{\alpha\beta\gamma\delta}(\mathbf{r}) &= (\delta_{\alpha\beta}\delta_{\gamma\delta} + \delta_{\alpha\gamma}\delta_{\beta\delta} + \delta_{\alpha\delta}\delta_{\beta\gamma}) v_{41}(r) + (\delta_{\gamma\delta} r_\alpha r_\beta + 5 \text{ permutations}) \frac{v_{42}(r)}{r^2} \\ &\quad + r_\alpha r_\beta r_\gamma r_\delta \left(\frac{v_{43}(r)}{r^4} \right), \end{aligned} \quad (4.27)$$

where again $v_{41}(r)$, $v_{42}(r)$, and $v_{43}(r)$ are radial functions defined in Chapter 2. [62] Note that these radial functions have different functional forms depending on the level of approximation being employed.

The integral in Eq. (4.22) can be divided into two parts, $|\mathbf{r} - \mathbf{r}'| \rightarrow 0$ and $|\mathbf{r} - \mathbf{r}'| > 0$. Since the self-contribution to the field gradient vanishes at the

singularity (see the supporting information), Eq. (4.22) can be written as,

$$\partial_\alpha E_\beta(\mathbf{r}) = \partial_\alpha E_\beta^\circ(\mathbf{r}) + \frac{1}{8\pi\epsilon_o} \int_{|\mathbf{r}-\mathbf{r}'|>0} T_{\alpha\beta\gamma\delta}(\mathbf{r}-\mathbf{r}') Q_{\gamma\delta}(\mathbf{r}') d\mathbf{r}'. \quad (4.28)$$

If $\mathbf{r} = \mathbf{r}'$ is excluded from the integration, the total gradient can be most easily expressed in terms of traceless quadrupole density as below,[95]

$$\partial_\alpha E_\beta(\mathbf{r}) = \partial_\alpha E_\beta^\circ(\mathbf{r}) + \frac{1}{24\pi\epsilon_o} \int_{|\mathbf{r}-\mathbf{r}'|>0} T_{\alpha\beta\gamma\delta}(\mathbf{r}-\mathbf{r}') \Theta_{\gamma\delta}(\mathbf{r}') d\mathbf{r}', \quad (4.29)$$

where $\Theta_{\alpha\beta} = 3Q_{\alpha\beta} - \delta_{\alpha\beta} Tr(Q)$ is the traceless quadrupole density. In analogy to Eq. (4.17) above, the quadrupole polarization density may now be related to the quadrupolar susceptibility, χ_Q ,

$$\frac{1}{3} \Theta_{\alpha\beta}(\mathbf{r}) = \epsilon_o \chi_Q \left[\partial_\alpha E_\beta^\circ(\mathbf{r}) + \frac{1}{24\pi\epsilon_o} \int_{|\mathbf{r}-\mathbf{r}'|>0} T_{\alpha\beta\gamma\delta}(\mathbf{r}-\mathbf{r}') \Theta_{\gamma\delta}(\mathbf{r}') d\mathbf{r}' \right]. \quad (4.30)$$

For periodic boundaries and with a uniform imposed $\partial_\alpha E_\beta^\circ$, the quadrupole density $\Theta_{\alpha\beta}$ will be uniform over the entire space. After performing a Fourier transform (see the Appendix in Ref.[2]) we obtain,

$$\frac{1}{3} \tilde{\Theta}_{\alpha\beta}(\mathbf{k}) = \epsilon_o \chi_Q \left[\partial_\alpha \tilde{E}_\beta^\circ(\mathbf{k}) + \frac{1}{24\pi\epsilon_o} \tilde{T}_{\alpha\beta\gamma\delta}(\mathbf{k}) \tilde{\Theta}_{\gamma\delta}(\mathbf{k}) \right]. \quad (4.31)$$

If the applied field gradient is homogeneous over the entire volume, $\partial_\alpha \tilde{E}_\beta^\circ(\mathbf{k}) = 0$ except at $\mathbf{k} = 0$. Similarly, the quadrupolar polarization density can also be considered uniform over entire space. As in the dipolar case, [2] the only relevant contribution from the interaction tensor will also be when $\mathbf{k} = 0$. Therefore

Eq. (4.31) can be written as,

$$\frac{1}{3}\tilde{\Theta}_{\alpha\beta}(0) = \epsilon_o\chi_Q \left[\partial_\alpha \tilde{E}_\beta^\circ(0) + \frac{1}{24\pi\epsilon_o} \tilde{T}_{\alpha\beta\gamma\delta}(0) \tilde{\Theta}_{\gamma\delta}(0) \right]. \quad (4.32)$$

The quadrupolar tensor $\tilde{T}_{\alpha\beta\gamma\delta}(0)$ is a rank 4 tensor with 81 elements. The only non-zero elements, however, are those with two doubly-repeated indices, *i.e.* $\tilde{T}_{aabb}(0)$ and all permutations of these indices. The special case of quadruply-repeated indices, $\tilde{T}_{aaaa}(0)$ also survives (see appendix B.1). Furthermore, for the both diagonal and non-diagonal components of the quadrupolar polarization $\tilde{\Theta}_{\alpha\beta}$, we can contract the second term in Eq. 4.32 (see appendix B.1):

$$\tilde{T}_{\alpha\beta\gamma\delta}(0) \tilde{\Theta}_{\gamma\delta}(0) = 8\pi B \tilde{\Theta}_{\alpha\beta}(0). \quad (4.33)$$

Here $B = \tilde{T}_{abab}(0)/4\pi$ for $a \neq b$. Using this quadrupolar contraction we can solve Eq. (4.32) as follows

$$\begin{aligned} \frac{1}{3}\tilde{\Theta}_{\alpha\beta}(0) &= \epsilon_o\chi_Q \left[\partial_\alpha \tilde{E}_\beta^\circ(0) + \frac{B}{3\epsilon_o} \tilde{\Theta}_{\alpha\beta}(0) \right] \\ &= \left[\frac{\epsilon_o\chi_Q}{1 - \chi_Q B} \right] \partial_\alpha \tilde{E}_\beta^\circ(0). \end{aligned} \quad (4.34)$$

In real space, the correction factor is found to be,

$$B = \frac{1}{4\pi} \tilde{T}_{abab}(0) = \frac{1}{4\pi} \int_V T_{abab}(\mathbf{r}) d\mathbf{r}, \quad (4.35)$$

which has been integrated over the interaction volume V and has units of length^{-2} .

In terms of the traced quadrupole moment, Eq. (4.34) can be written,

$$\mathbf{Q} - \frac{\mathbf{I}}{3}\text{Tr}(\mathbf{Q}) = \frac{\epsilon_o\chi_Q}{1 - \chi_Q B} \nabla \mathbf{E}^\circ \quad (4.36)$$

Comparing (4.36) and (4.18) we obtain,

$$\frac{\langle \mathbf{M}_Q^2 \rangle - \langle \mathbf{M}_Q \rangle^2}{15\epsilon_o V k_B T} = \frac{\chi_Q}{1 - \chi_Q B}, \quad (4.37)$$

or equivalently,

$$\chi_Q = \frac{\langle \mathbf{M}_Q^2 \rangle - \langle \mathbf{M}_Q \rangle^2}{15\epsilon_o V k_B T} \left(1 + B \frac{\langle \mathbf{M}_Q^2 \rangle - \langle \mathbf{M}_Q \rangle^2}{15\epsilon_o V k_B T} \right)^{-1} \quad (4.38)$$

Eq. (4.38) now expresses a bulk property (the quadrupolar susceptibility, χ_Q) in terms of a fluctuation in the system quadrupole moment and a quadrupolar correction factor (B). The correction factors depend on the cutoff method being employed in the simulation, and these are listed in Table 4.2.

In terms of the macroscopic quadrupole polarizability, α_Q , which may be thought of as the “conducting boundary” version of the susceptibility,

$$\chi_Q = \frac{\alpha_Q}{1 + B\alpha_Q}. \quad (4.39)$$

If an electrostatic method produces $B \rightarrow 0$, the computed quadrupole polarizability and quadrupole susceptibility converge to the same value.

TABLE 4.2: Expressions for the quadrupolar correction factor (B) for the real-space electrostatic methods in terms of the damping parameter (α) and the cutoff radius (r_c). The units of the correction factor are length⁻² for quadrupolar fluids.

Method	Molecular Representation		
	charges	dipoles	quadrupoles
Shifted Potential (SP)	$-\frac{8\alpha^5 r_c^3 e^{-\alpha^2 r_c^2}}{15\sqrt{\pi}}$	$-\frac{3\text{erfc}(\kappa_c \alpha)}{5r_c^2} - \frac{2\alpha e^{-\alpha^2 r_c^2} (9+6\alpha^2 r_c^2 + 4\alpha^4 r_c^4)}{15\sqrt{\pi} r_c}$	$-\frac{16\alpha^7 r_c^5 e^{-\alpha^2 r_c^2}}{45\sqrt{\pi}}$
Gradient-shifted (GSF)	$-\frac{8\alpha^5 r_c^3 e^{-\alpha^2 r_c^2}}{15\sqrt{\pi}}$	0	$-\frac{4\alpha^7 r_c^5 e^{-\alpha^2 r_c^2} (-1+2\alpha^2 r_c^2)}{45\sqrt{\pi}}$
Taylor-shifted (TSF)	$-\frac{8\alpha^5 r_c^3 e^{-\alpha^2 r_c^2}}{15\sqrt{\pi}}$	$\frac{4\text{erfc}(\alpha r_c)}{5r_c^2} + \frac{8\alpha e^{-\alpha^2 r_c^2} (3+2\alpha^2 r_c^2 + \alpha^4 r_c^4)}{15\sqrt{\pi} r_c}$	$\frac{2\text{erfc}(\alpha r_c)}{r_c^2} + \frac{4\alpha e^{-\alpha^2 r_c^2} (45+30\alpha^2 r_c^2 + 12\alpha^4 r_c^4 + 3\alpha^6 r_c^6 + 2\alpha^8 r_c^8)}{45\sqrt{\pi}}$
Spherical Cutoff (SC)	$-\frac{8\alpha^5 r_c^3 e^{-\alpha^2 r_c^2}}{15\sqrt{\pi}}$	$-\frac{8\alpha^5 r_c^3 e^{-\alpha^2 r_c^2}}{15\sqrt{\pi}}$	$-\frac{8\alpha^5 r_c^3 e^{-\alpha^2 r_c^2}}{15\sqrt{\pi}}$
Ewald-Kornfeld (EK)	$-\frac{8\kappa^5 r_c^3 e^{-\kappa^2 r_c^2}}{15\sqrt{\pi}}$	$-\frac{8\kappa^5 r_c^3 e^{-\kappa^2 r_c^2}}{15\sqrt{\pi}}$	$-\frac{8\kappa^5 r_c^3 e^{-\kappa^2 r_c^2}}{15\sqrt{\pi}}$

4.4 Screening of Charges by Multipolar Fluids

In a dipolar fluid, the static dielectric constant is also a measure of the ability of the fluid to screen charges from one another. A set of point charges creates an inhomogeneous field in the fluid, and the fluid responds to this field as if it was created externally or via local polarization fluctuations. For this reason, the dielectric constant can be used to estimate an effective potential between two point charges (C_i and C_j) embedded in the fluid,

$$U_{\text{effective}} = \frac{C_i C_j}{4\pi\epsilon_0\epsilon r_{ij}}. \quad (4.40)$$

The same set of point charges can also create an inhomogeneous field *gradient*, and this will cause a response in a quadrupolar fluid that will also cause an effective screening. As discussed above, however, the relevant physical property in quadrupolar fluids is the susceptibility, χ_Q . The screening dielectric associated with the quadrupolar susceptibility is defined as,[86]

$$\epsilon = 1 + \chi_Q G = 1 + G \frac{\alpha_Q}{1 + \alpha_Q B} \quad (4.41)$$

where G is a geometrical factor that depends on the geometry of the field perturbation,

$$G = \frac{\int_V |\nabla \mathbf{E}^\circ|^2 d\mathbf{r}}{\int_V |\mathbf{E}^\circ|^2 d\mathbf{r}} \quad (4.42)$$

integrated over the interaction volume. Note that this geometrical factor is also required to compute effective dielectric constants even when the field gradient is homogeneous over the entire sample.

To measure effective screening in a multipolar fluid, we compute an effective

interaction potential, the potential of mean force (PMF), between positively and negatively charged ions when they are screened by the intervening fluid. The PMF is obtained from a sequence of simulations in which two ions are constrained to a fixed distance, and the average constraint force to hold them at a fixed distance r is collected during a long simulation,[98]

$$w(r) = \int_{r_o}^r \left\langle \frac{\partial f}{\partial r'} \right\rangle_{r'} dr' + 2k_B T \ln \left(\frac{r}{r_o} \right) + w(r_o), \quad (4.43)$$

where $\langle \partial f / \partial r' \rangle_{r'}$ is the mean constraint force required to hold the ions at distance r' , $2k_B T \log(r/r_o)$ is the Fixman factor,[99] and r_o is a reference position (usually taken as a large separation between the ions). If the dielectric constant is a good measure of the screening at all inter-ion separations, we would expect $w(r)$ to have the form in Eq. (4.40). Because real fluids are not continuum dielectrics, the effective dielectric constant is a function of the inter-ionic separation,

$$\epsilon(r) = \frac{u_{\text{raw}}(r) - u_{\text{raw}}(r_o)}{w(r) - w(r_o)} \quad (4.44)$$

where $u_{\text{raw}}(r)$ is the direct charge-charge interaction potential that is in use during the simulation. $\epsilon(r)$ may vary considerably from the bulk estimates at short distances, although it should converge to the bulk value as the separation between the ions increases.

4.5 Simulation Methodology

To test the formalism developed in the preceding sections, we have carried out computer simulations using three different techniques: i) simulations in the presence of external fields, ii) equilibrium calculations of box moment fluctuations,

and iii) potentials of mean force (PMF) between embedded ions. In all cases, the fluids were composed of point multipoles protected by a Lennard-Jones potential. The parameters used in the test systems are given in Table 4.3.

The first of the test systems consists entirely of fluids of point dipolar or quadrupolar molecules in the presence of constant field or field gradients. Since there are no isolated charges within the system, the divergence of the field will be zero, *i.e.* $\vec{\nabla} \cdot \mathbf{E} = 0$. This condition can be satisfied by using the relatively simple applied potential as described in the supporting information.

When a constant electric field or field gradient is applied to the system, the molecules align along the direction of the applied field, and polarize to a degree determined both by the strength of the field and the fluid’s polarizability. We have calculated ensemble averages of the box dipole and quadrupole moments as a function of the strength of the applied fields. If the fields are sufficiently weak, the response is linear in the field strength, and one can easily compute the polarizability directly from the simulations.

The second set of test systems consists of equilibrium simulations of fluids of point dipolar or quadrupolar molecules simulated in the absence of any external perturbation. The fluctuation of the ensemble averages of the box multipolar moment was calculated for each of the multipolar fluids. The box multipolar moments were computed as simple sums over the instantaneous molecular moments, and fluctuations in these quantities were obtained from Eqs. (4.4) and (4.20). The macroscopic polarizabilities of the system at a were derived using Eqs.(4.3) and (4.18).

The final system consists of dipolar or quadrupolar fluids with two oppositely charged ions embedded within the fluid. These ions are constrained to be at

TABLE 4.3: The parameters used in simulations to evaluate the dielectric response of the new real-space methods.

Test system	LJ parameters		Electrostatic moments					mass (amu)	I_{xx} (amu Å ²)	I_{yy} (amu Å ²)	I_{zz}
	σ (Å)	ϵ (kcal/mol)	C (e)	D (debye)	Q_{xx} (debye Å)	Q_{yy} (debye Å)	Q_{zz} (debye Å)				
Dipolar fluid	3.41	0.2381	-	1.4026	-	-	-	39.948	11.613	11.613	0.0
Quadrupolar fluid	2.985	0.265	-	-	0.0	0.0	-2.139	18.0153	43.0565	43.0565	0.0
q+	1.0	0.1	+1	-	-	-	-	22.98	-	-	-
q-	1.0	0.1	-1	-	-	-	-	22.98	-	-	-

fixed distance throughout a simulation, although they are allowed to move freely throughout the fluid while satisfying that constraint. Separate simulations were run at a range of constraint distances. A dielectric screening factor was computed using the ratio between the potential between the two ions in the absence of the fluid medium and the PMF obtained from the simulations.

We carried out these simulations for all three of the new real-space electrostatic methods (SP, GSF, and TSF) that were developed in the Chapter 2 (Ref. citePaperI) in the series. The radius of the cutoff sphere was taken to be 12 Å. Each of the real space methods also depends on an adjustable damping parameter α (in units of length^{-1}). We have selected ten different values of damping parameter: 0.0, 0.05, 0.1, 0.15, 0.175, 0.2, 0.225, 0.25, 0.3, and 0.35 Å⁻¹ in our simulations of the dipolar liquids, while four values were chosen for the quadrupolar fluids: 0.0, 0.1, 0.2, and 0.3 Å⁻¹.

For each of the methods and systems listed above, a reference simulation was carried out using a multipolar implementation of the Ewald sum.[63, 64] A default tolerance of 1×10^{-8} kcal/mol was used in all Ewald calculations, resulting in Ewald coefficient 0.3119 Å⁻¹ for a cutoff radius of 12 Å. All of the electrostatics and constraint methods were implemented in our group’s open source molecular simulation program, OpenMD,[18, 100] which was used for all calculations in this work.

Dipolar systems contained 2048 Lennard-Jones-protected point dipolar (Stockmayer) molecules with reduced density $\rho^* = 0.822$, temperature $T^* = 1.15$, moment of inertia $I^* = 0.025$, and dipole moment $\mu^* = \sqrt{3.0}$. These systems were equilibrated for 0.5 ns in the canonical (NVT) ensemble. Data collection was carried out over a 1 ns simulation in the microcanonical (NVE) ensemble. Box

dipole moments were sampled every fs. For simulations with external perturbations, field strengths ranging from $0 - 10 \times 10^{-4} \text{ V/\AA}$ with increments of 10^{-4} V/\AA were carried out for each system.

Quadrupolar systems contained 4000 linear point quadrupoles with a density 2.338 g/cm^3 at a temperature of 500 K. These systems were equilibrated for 200 ps in a canonical (NVT) ensemble. Data collection was carried out over a 500 ps simulation in the microcanonical (NVE) ensemble. Components of box quadrupole moments were sampled every 100 fs. For quadrupolar simulations with external field gradients, field strengths ranging from $0 - 9 \times 10^{-2} \text{ V/\AA}^2$ with increments of 10^{-2} V/\AA^2 were carried out for each system.

To carry out the PMF simulations, two of the multipolar molecules in the test system were converted into q+ and q- ions and constrained to remain at a fixed distance for the duration of the simulation. The constrained distance was then varied from 5–12 Å. In the PMF calculations, all simulations were equilibrated for 500 ps in the NVT ensemble and run for 5 ns in the microcanonical (NVE) ensemble. Constraint forces were sampled every 20 fs.

4.6 Results

4.6.1 Dipolar fluid

[tbp] The macroscopic polarizability (α_D) for the dipolar fluid is shown in the upper panels in Fig. 4.3. The polarizability obtained from the both perturbation and fluctuation approaches are in excellent agreement with each other. The data also show a strong dependence on the damping parameter for both the Shifted Potential (SP) and Gradient Shifted force (GSF) methods, while Taylor shifted force (TSF) is largely independent of the damping parameter.

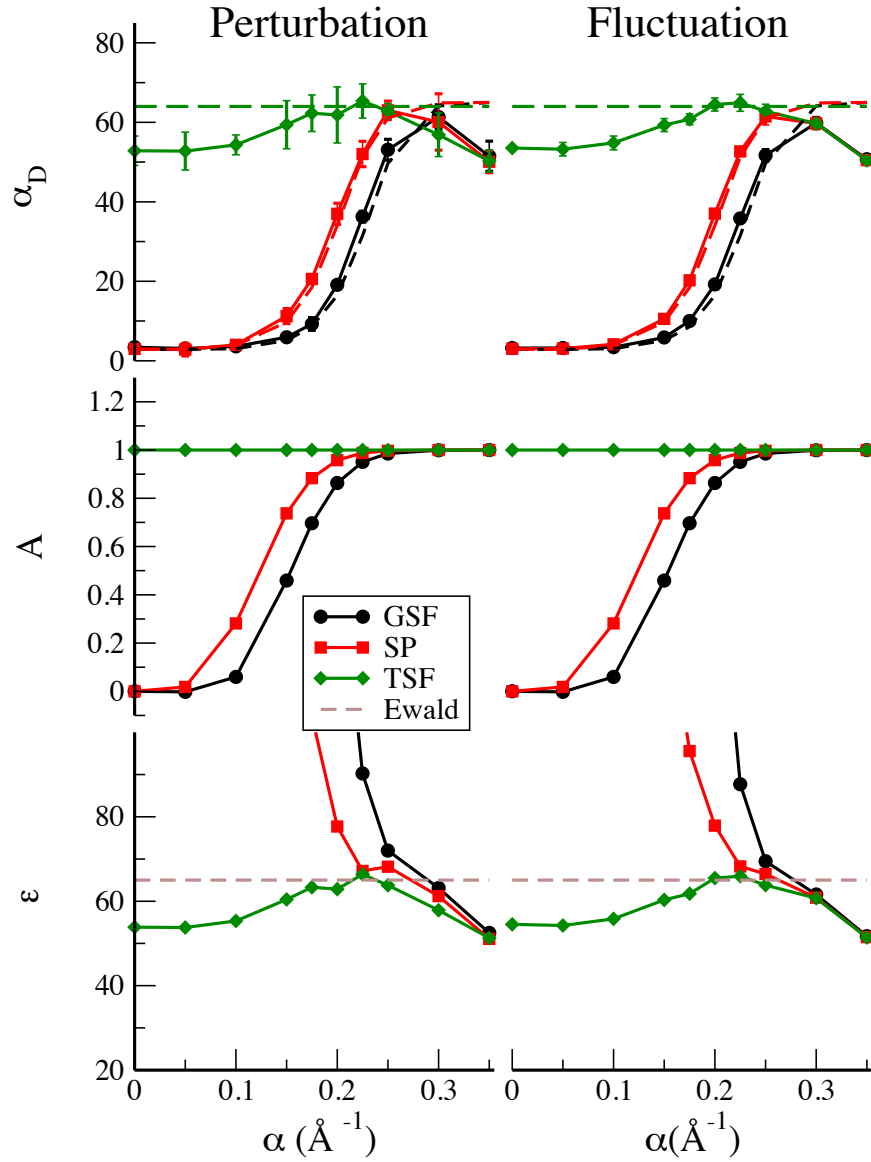


Figure 4.3. The polarizability (α_D), correction factor (A), and dielectric constant (ϵ) for the test dipolar fluid. The left panels were computed using external fields, and those on the right are the result of equilibrium fluctuations. In the GSF and SP methods, the corrections are large in with small values of α , and a optimal damping coefficient is evident around 0.25 \AA^{-1} . The dashed lines in the upper panel indicate back-calculation of the polarizability using the Ewald estimate (Refs.[1] and [2]) for the dielectric constant.

The calculated correction factors discussed in section 4.2.3 are shown in the middle panels. Because the TSF method has $A = 1$ for all values of the damping parameter, the computed polarizabilities need no correction for the dielectric calculation. The value of A varies with the damping parameter in both the SP and GSF methods, and inclusion of the correction yields dielectric estimates (shown in the lower panel) that are generally too large until the damping reaches $\sim 0.25 \text{ \AA}^{-1}$. Above this value, the dielectric constants are generally in good agreement with previous simulation results.[2]

Fig. 4.3 also contains back-calculations of the polarizability using the reference (Ewald) simulation results.[2] These are indicated with dashed lines in the upper panels. It is clear that the expected polarizability for the SP and GSF methods are quite close to results obtained from the simulations. This indicates that the correction formula for the dipolar fluid (Eq. (4.12)) is quite sensitive when the value of A deviates significantly from unity.

These results also suggest an optimal value for the damping parameter of ($\alpha \sim 0.2 - 0.3 \text{ \AA}^{-1}$) when evaluating dielectric constants of point dipolar fluids using either the perturbation and fluctuation approaches for the new real-space methods.

We have also evaluated the distance-dependent screening factor, $\epsilon(r)$, between two oppositely charged ions when they are placed in the dipolar fluid. These results were computed using Eq. (4.43) and are shown in Fig. 4.4.

The screening factor is similar to the dielectric constant, but measures a local property of the ions in the fluid and depends on both ion-dipole and dipole-dipole interactions. These interactions depend on the distance between ions as well as the electrostatic interaction methods utilized in the simulations. The screening

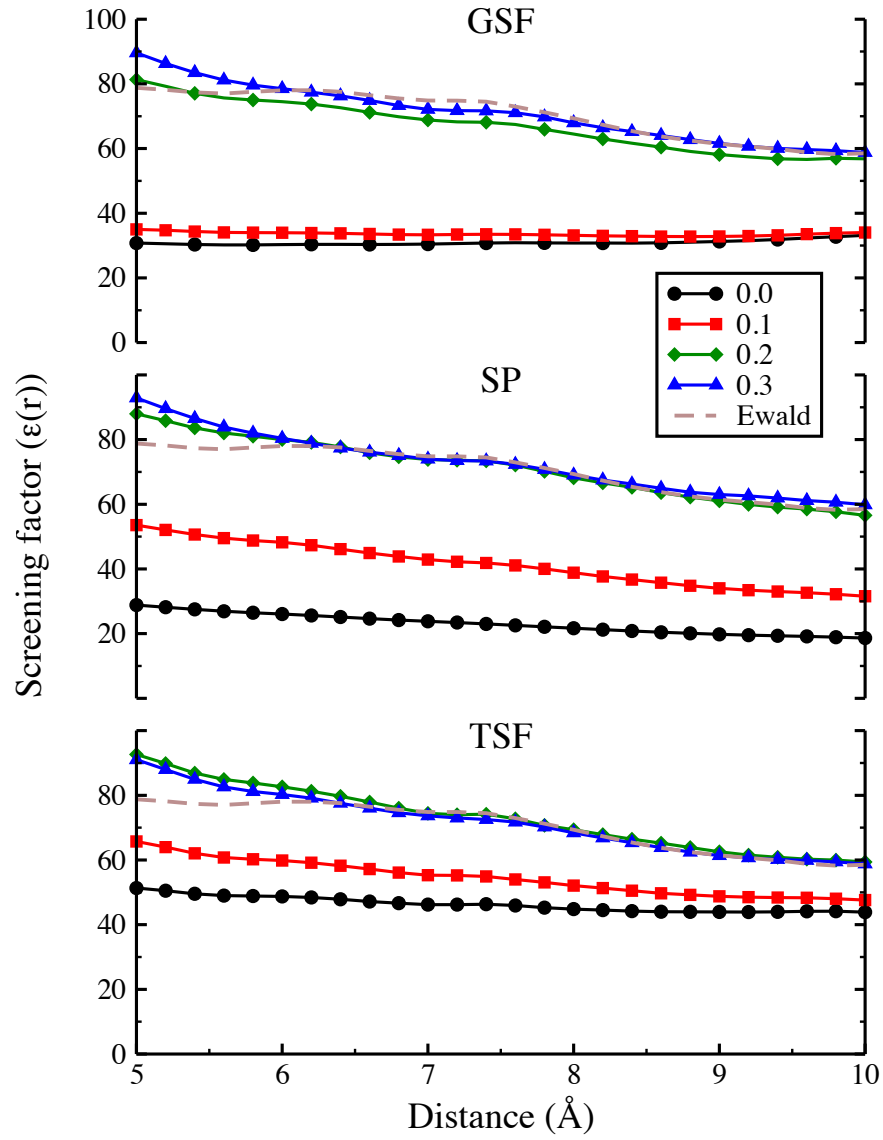


Figure 4.4. The distance-dependent screening factor, $\epsilon(r)$, between two ions immersed in the dipolar fluid. The new methods are shown in separate panels, and different values of the damping parameter (α) are indicated with different symbols. All of the methods appear to be converging to the bulk dielectric constant (~ 65) at large ion separations.

should converge to the dielectric constant when the field due to ions is small. This occurs when the ions are separated (or when the damping parameter is large). In Fig. 4.4 we observe that for the higher value of damping α *i.e.* $\alpha = 0.2 \text{ \AA}^{-1}$ and 0.3 \AA^{-1} and large separation between ions, the screening factor does indeed approach the correct dielectric constant.

It is also notable that the TSF method again displays smaller perturbations away from the correct dielectric screening behavior. We also observe that for TSF method yields high dielectric screening even for lower values of α .

At short distances, the presence of the ions creates a strong local field that acts to align nearby dipoles nearly perfectly in opposition to the field from the ions. This has the effect of increasing the effective screening when the ions are brought close to one another. This effect is present even in the full Ewald treatment, and indicates that the local ordering behavior is being captured by all of the moderately-damped real-space methods.

4.6.2 Quadrupolar fluid

The polarizability (α_Q), correction factor (B), and susceptibility (χ_Q) for the quadrupolar fluid is plotted against damping parameter Fig. 4.5. In quadrupolar fluids, both the polarizability and susceptibility have units of length^2 . Although the susceptibility has dimensionality, it is the relevant measure of macroscopic quadrupolar properties.[87, 88] The left panel in Fig. 4.5 shows results obtained from the applied field gradient simulations whereas the results from the equilibrium fluctuation formula are plotted in the right panels.

The susceptibility for the quadrupolar fluid is obtained from quadrupolarizability and a correction factor using Eq. (4.39). The susceptibilities are shown in

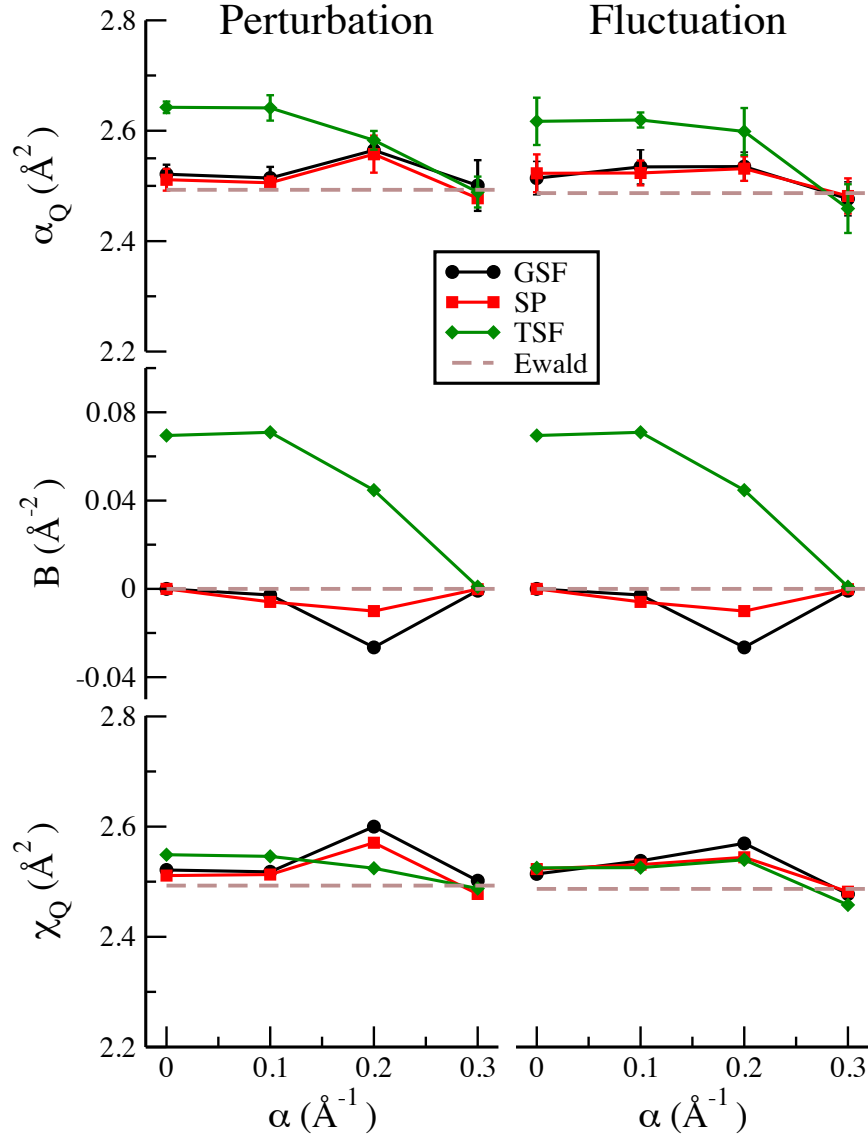


Figure 4.5. The quadrupole polarizability (α_Q), correction factor (B), and susceptibility (χ_Q) for the test quadrupolar fluid. The left panels were computed using external field gradients, and those on the right are the result of equilibrium fluctuations. The GSF and SP methods allow nearly unmodified use of the “conducting boundary” or polarizability results in place of the bulk susceptibility.

the bottom panels of Fig. 4.5. All three methods: (SP, GSF, and TSF) produce similar susceptibilities over the range of damping parameters. This shows that susceptibility derived using the quadrupolarizability and the correction factors are essentially independent of the electrostatic method utilized in the simulation.

A more difficult test of the quadrupolar susceptibility is made by comparing with direct calculation of the electrostatic screening using the potential of mean force (PMF). Since the effective dielectric constant for a quadrupolar fluid depends on the geometry of the field and field gradient, this is not a physical property of the quadrupolar fluid.

The geometrical factor for embedded ions changes with the ion separation distance. It is therefore reasonable to treat the dielectric constant as a distance-dependent screening factor. Since the quadrupolar molecules couple with the gradient of the field, the distribution of the quadrupoles will be inhomogeneously distributed around the point charges. Hence the distribution of quadrupolar molecules should be taken into account when computing the geometrical factors in the presence of this perturbation,

$$\begin{aligned}
G &= \frac{\int_V g(\mathbf{r}) |\nabla \mathbf{E}^\circ|^2 d\mathbf{r}}{\int_V |\mathbf{E}^\circ|^2 d\mathbf{r}} \\
&= \frac{2\pi \int_{-1}^1 \int_0^R r^2 g(r, \cos \theta) |\nabla \mathbf{E}^\circ|^2 dr d(\cos \theta)}{\int_V |\mathbf{E}^\circ|^2 d\mathbf{r}} \quad (4.45)
\end{aligned}$$

where $g(r, \cos \theta)$ is a distribution function for the quadrupoles with respect to an origin at midpoint of a line joining the two probe charges.

The effective screening factor is plotted against ion separation distance in Fig. 4.6. The screening evaluated from the perturbation and fluctuation methods are shown in right and central panels. Here the susceptibility is calculated from the

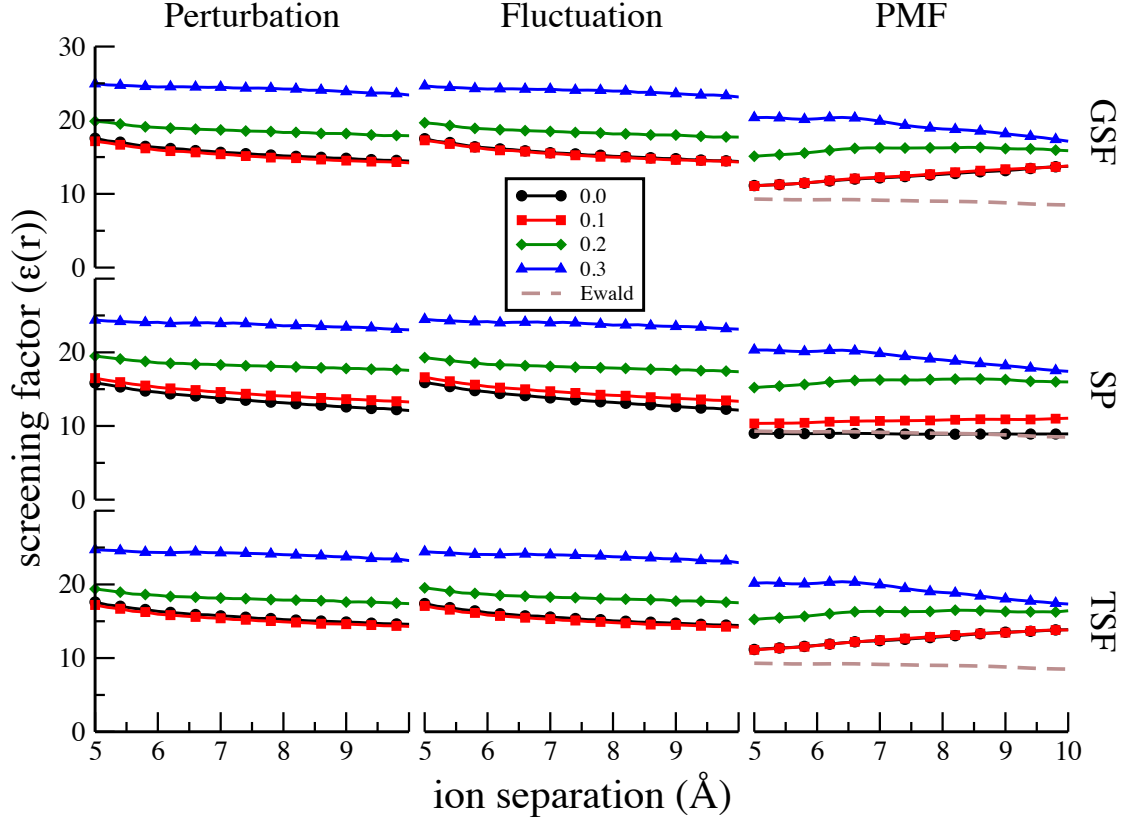


Figure 4.6. The distance-dependent screening factor, $\epsilon(r)$, between two ions immersed in the quadrupolar fluid. Results from the perturbation and fluctuation methods are shown in right and central panels. Here the susceptibility is calculated from the simulation and the geometrical factor is evaluated analytically, using the field and field-gradient produced by ions. The right hand panel shows the screening factor obtained from the PMF calculations.

simulation and the geometrical factor is evaluated analytically, using the field and field-gradient produced by ions. The right hand panel shows the screening factor obtained from the PMF calculations.

We note that the screening factor obtained from both the perturbation and fluctuation formula show good agreement with the screening factor calculated using PMF method. As there are no large differences in quadrupole-quadrupole interactions for various real-space methods,[62, 89] we generally good agreement for the screening factors using any of the real space methods.

4.7 Summary

We have used both perturbation and fluctuation approaches to evaluate dielectric properties for dipolar and quadrupolar fluids. The static dielectric constant is the relevant bulk property for dipolar fluids, while the quadrupolar susceptibility plays a similar role for quadrupoles. Corrections to both the static dielectric constant and the quadrupolar susceptibility were derived for three new real space electrostatic methods, and these corrections were tested against a third measure of dielectric screening, the potential of mean force between two ions immersed in the fluids.

For the dipolar fluids, we find that the polarizability evaluated using the perturbation and fluctuation methods show excellent agreement, indicating that equilibrium calculations of the dipole fluctuations are good measures of bulk polarizability. One of the findings of the Chapter 3 is that the moderately damped GSF and SP methods were most suitable for molecular dynamics and Monte Carlo simulations, respectively.[89]

The dielectric constant evaluated using the computed polarizability and cor-

rection factors agrees well with the previous Ewald-based simulation results [1, 2] for moderate damping parameters in the range $0.25\text{-}0.3 \text{ \AA}^{-1}$.

Although the TSF method alters many dynamic and structural features in multipolar liquids,[89] it is surprisingly good at computing bulk dielectric properties at nearly all ranges of the damping parameter. In fact, the correction factor, $A = 1$, for the TSF method so the conducting boundary formula is essentially correct when using this method for point dipolar fluids.

The dielectric correction formula (Eq. (4.12)) is extremely sensitive when the correction factor (A) deviates from 1, and this behavior is also seen in the effective screening of ions embedded in the fluid.

As in the dipolar case, the quadpole polarizability evaluated from both perturbation and fluctuation simulations show excellent agreement, again confirming that equilibrium fluctuation calculations are sufficient to reproduce bulk dielectric properties in these fluids. The quadrupolar susceptibility calculated via our derived correction factors tends to produce the same result for all three real space methods. Similarly, the screening factor calculated using the susceptibility and a weighted geometric factor provides good agreement with results obtained directly via potentials of mean force. For quadrupolar fluids, the distance dependence of the electrostatic interaction is significantly reduced and the correction factors are all small. These points suggest that how an electrostatic method treats the cutoff radius become less consequential for higher order multipoles.

For this reason, we renew our recommendation that the moderately-damped GSF method is an excellent choice for molecular dynamics simulation where point-multipole interactions are being utilized to compute bulk properties of fluids.

CHAPTER 5

CONCLUSIONS

In this dissertation, I have presented the three newly developed real-space methods: Shifted Potential (SP), Gradient Shifted Force (GSF), and Taylor Shifted Force (TSF), for evaluating electrostatic interactions between multipoles in molecular simulations. I have also computed various static and dynamic properties using newly developed real space methods and compared result with the Ewald sum. I have also studied the conservation of total energy using real-space as well as Ewald method. Finally, I have discussed the perturbation, fluctuation, and PMF methods for calculating dielectric properties for dipolar and quadrupolar systems.

The energy constant evaluated for the dipolar and quadrupolar crystal using SP and GSF methods show excellent agreement with the analytical result. The TSF method performs poorly in predicting the energy constant for both dipolar and quadrupolar crystal. We need to take larger cutoff radius and suitable damping alpha to predict energy constant using TSF method. For the dipolar crystal, higher damping favors the quick convergence of the energy constant when plotted against cutoff radius. But the higher damping can presents additional issues while calculating energy constant for quadrupolar crystal, hence the small damping parameter is suitable for the quadrupolar system.

The SP method is the mutipolar version of the Wolf's shifted potential for the charge-charge interaction, whereas the GSF and TSF method are multipolar

generalization of the Damped Shifted Force (DSF) method. In the SP method, the potential energy smoothly approaches to zero at the cutoff radius but the forces and torques derived from the energies are not continuous at the cutoff radius. On the other hand, the forces and torques as well as energies evaluated in the GSF and TSF method vanishes at the cutoff radius. Since the energy evaluated from the SP method shows excellent agreement with the Ewald, it is suitable for the Monte Carlo (MC) simulation. The GSF method performs well in conserving total energy in MD simulations and produces good quantitative agreement with the Ewald energies, forces and torques, therefore better choice for MD simulations. Both SP and GSF models perform remarkably well with moderate damping parameter for reproducing static as well as dynamic properties in the liquid systems. All of these real-space methods scales *linearly* with system size and are easily parallelizable, therefore reduce computational cost substantially while performing large simulations.

The test of the dielectric properties is very important to validate the electrostatic interaction methods. I presented three methods: perturbation, fluctuation, and potential of mean force (PMF), to evaluate dielectric properties for dipolar and quadrupolar fluids. The polarizability obtained from simulations, using perturbation and fluctuation methods, shows excellent agreement with each other for all SP, GSF, and TSF methods. To calculate the dielectric constant and susceptibility from the dipolar polarization (measured from simulations), we need to take account of correction factor listed in the Chapter 4. The correction factor for TSF method is 1, which essentially signifies no correction. Therefore the dielectric constant evaluated using conducting boundary condition can produce good result for all values of damping α . In the other words, the susceptibility and

polarizability are the same in the case of dipolar TSF method. The correction factor for SP and GSF methods depend on damping parameter as well as cutoff radius. The formula for deriving dielectric constant from polarization is very sensitive when the damping parameter is very small. Therefore moderate damping alpha between $(0.25 - 0.3 \text{ \AA}^{-2})$ are always suitable choice for calculating dielectric properties using SP and GSF method.

For the quadrupolar fluid, the correction factor essentially small for SP and GSF method whereas the correction factor is comparatively large for the TSF. Different than dipolar case, the quadrupolar susceptibility but not dielectric screening measures the actual bulk properties of the quadrupolar fluid. On other hand, the dielectric constant is geometry dependent and can be derived from the susceptibility and geometry of the applied field.

The dipolar dielectric screening calculated from the perturbation and fluctuation also agree with the screening factor measured from the PMF method for the damping parameter $0.25 - 0.3 \text{ \AA}^{-2}$. Similarly the quadrupolar dielectric screening calculated between two point charges using susceptibility and geometrical factor shows good agreement with the direct screening measured using PMF method.

All of these newly developed real space methods are computationally very efficient as compared to Ewald method. The physical properties predicted by the real-space methods, with the suitable choice of damping parameter, are as accurate as the computationally expensive Ewald method. We can even predict the dielectric properties correctly using newly developed methods with the use of the correction factor. Therefore our newly developed real space methods are the suitable choice for calculating electrostatic interactions between molecules in the large molecular simulations.

APPENDIX A

A.1 Smith's $B_l(r)$ functions for damped-charge distributions

The following summarizes Smith's $B_l(r)$ functions and includes formulas given in his appendix.[64] The first function $B_0(r)$ is defined by

$$B_0(r) = \frac{\text{erfc}(\alpha r)}{r} = \frac{2}{\sqrt{\pi}r} \int_{\alpha r}^{\infty} e^{-s^2} ds. \quad (\text{A.1})$$

The first derivative of this function is

$$\frac{dB_0(r)}{dr} = -\frac{1}{r^2} \text{erfc}(\alpha r) - \frac{2\alpha}{r\sqrt{\pi}} e^{-\alpha^2 r^2} \quad (\text{A.2})$$

which can be used to define a function $B_1(r)$:

$$B_1(r) = -\frac{1}{r} \frac{dB_0(r)}{dr} \quad (\text{A.3})$$

In general, the recurrence relation,

$$B_l(r) = -\frac{1}{r} \frac{dB_{l-1}(r)}{dr} = \frac{1}{r^2} \left[(2l-1)B_{l-1}(r) + \frac{(2\alpha^2)^l}{\alpha\sqrt{\pi}} e^{-\alpha^2 r^2} \right], \quad (\text{A.4})$$

is very useful for building up higher derivatives. As noted by Smith, it is possible to approximate the $B_l(r)$ functions,

$$B_l(r) = \frac{(2l)!}{l!2^l r^{2l+1}} - \frac{(2\alpha^2)^{l+1}}{(2l+1)\alpha\sqrt{\pi}} + O(r). \quad (\text{A.5})$$

A.2 The r -dependent factors for TSF electrostatics

Using the shifted damped functions $f_n(r)$ defined by:

$$f_n(r) = B_0(r) - \sum_{m=0}^{n+1} \frac{(r - r_c)^m}{m!} B_0^{(m)}(r_c), \quad (\text{A.6})$$

where the superscript (m) denotes the m^{th} derivative. In this Appendix, we provide formulas for successive derivatives of this function. (If there is no damping, then $B_0(r)$ is replaced by $1/r$.) First, we find:

$$\frac{\partial f_n}{\partial r_\alpha} = \hat{r}_\alpha \frac{df_n}{dr}. \quad (\text{A.7})$$

This formula clearly brings in derivatives of Smith's $B_0(r)$ function, and we define higher-order derivatives as follows:

$$g_n(r) = \frac{df_n}{dr} = B_0^{(1)}(r) - \sum_{m=0}^n \frac{(r - r_c)^m}{m!} B_0^{(m+1)}(r_c) \quad (\text{A.8})$$

$$h_n(r) = \frac{d^2 f_n}{dr^2} = B_0^{(2)}(r) - \sum_{m=0}^{n-1} \frac{(r - r_c)^m}{m!} B_0^{(m+2)}(r_c) \quad (\text{A.9})$$

$$s_n(r) = \frac{d^3 f_n}{dr^3} = B_0^{(3)}(r) - \sum_{m=0}^{n-2} \frac{(r - r_c)^m}{m!} B_0^{(m+3)}(r_c) \quad (\text{A.10})$$

$$t_n(r) = \frac{d^4 f_n}{dr^4} = B_0^{(4)}(r) - \sum_{m=0}^{n-3} \frac{(r-r_c)^m}{m!} B_0^{(m+4)}(r_c) \quad (\text{A.11})$$

$$u_n(r) = \frac{d^5 f_n}{dr^5} = B_0^{(5)}(r) - \sum_{m=0}^{n-4} \frac{(r-r_c)^m}{m!} B_0^{(m+5)}(r_c). \quad (\text{A.12})$$

We note that the last function needed (for quadrupole-quadrupole interactions) is

$$u_4(r) = B_0^{(5)}(r) - B_0^{(5)}(r_c). \quad (\text{A.13})$$

The functions $f_n(r)$ to $u_n(r)$ can be computed recursively and stored on a grid for values of r from 0 to r_c . Using these functions, we find

$$\frac{\partial f_n}{\partial r_\alpha} = r_\alpha \frac{g_n}{r} \quad (\text{A.14})$$

$$\frac{\partial^2 f_n}{\partial r_\alpha \partial r_\beta} = \delta_{\alpha\beta} \frac{g_n}{r} + r_\alpha r_\beta \left(-\frac{g_n}{r^3} + \frac{h_n}{r^2} \right) \quad (\text{A.15})$$

$$\begin{aligned} \frac{\partial^3 f_n}{\partial r_\alpha \partial r_\beta \partial r_\gamma} &= (\delta_{\alpha\beta} r_\gamma + \delta_{\alpha\gamma} r_\beta + \delta_{\beta\gamma} r_\alpha) \left(-\frac{g_n}{r^3} + \frac{h_n}{r^2} \right) \\ &\quad + r_\alpha r_\beta r_\gamma \left(\frac{3g_n}{r^5} - \frac{3h_n}{r^4} + \frac{s_n}{r^3} \right) \end{aligned} \quad (\text{A.16})$$

$$\begin{aligned} \frac{\partial^4 f_n}{\partial r_\alpha \partial r_\beta \partial r_\gamma \partial r_\delta} &= (\delta_{\alpha\beta} \delta_{\gamma\delta} + \delta_{\alpha\gamma} \delta_{\beta\delta} + \delta_{\beta\gamma} \delta_{\alpha\delta}) \left(-\frac{g_n}{r^3} + \frac{h_n}{r^2} \right) \\ &\quad + (\delta_{\alpha\beta} r_\gamma r_\delta + 5 \text{ permutations}) \left(\frac{3g_n}{r^5} - \frac{3h_n}{r^4} + \frac{s_n}{r^3} \right) \\ &\quad + r_\alpha r_\beta r_\gamma r_\delta \left(-\frac{15g_n}{r^7} + \frac{15h_n}{r^6} - \frac{6s_n}{r^5} + \frac{t_n}{r^4} \right) \end{aligned} \quad (\text{A.17})$$

$$\begin{aligned} \frac{\partial^5 f_n}{\partial r_\alpha \partial r_\beta \partial r_\gamma \partial r_\delta \partial r_\epsilon} &= (\delta_{\alpha\beta} \delta_{\gamma\delta} r_\epsilon + 14 \text{ permutations}) \left(\frac{3g_n}{r^5} - \frac{3h_n}{r^4} + \frac{s_n}{r^3} \right) \\ &\quad + (\delta_{\alpha\beta} r_\gamma r_\delta r_\epsilon + 9 \text{ permutations}) \left(-\frac{15g_n}{r^7} + \frac{15h_n}{r^6} - \frac{6s_n}{r^5} + \frac{t_n}{r^4} \right) \\ &\quad + r_\alpha r_\beta r_\gamma r_\delta r_\epsilon \left(\frac{105g_n}{r^9} - \frac{105h_n}{r^8} + \frac{45s_n}{r^7} - \frac{10t_n}{r^6} + \frac{u_n}{r^5} \right) \end{aligned} \quad (\text{A.18})$$

A.3 The r -dependent factors for GSF electrostatics

In Gradient-shifted force electrostatics, the kernel is not expanded, and the expansion is carried out on the individual terms in the multipole interaction energies. For damped charges, this still brings multiple derivatives of the Smith's $B_0(r)$ function into the algebra. To denote these terms, we generalize the notation of the previous appendix. For either $f(r) = 1/r$ (undamped) or $f(r) = B_0(r)$ (damped),

$$g(r) = \frac{df}{dr} = -\frac{1}{r^2} \quad \text{or} \quad -rB_1(r) \quad (\text{A.19})$$

$$h(r) = \frac{dg}{dr} = \frac{d^2f}{dr^2} = \frac{2}{r^3} \quad \text{or} \quad -B_1(r) + r^2B_2(r) \quad (\text{A.20})$$

$$s(r) = \frac{dh}{dr} = \frac{d^3f}{dr^3} = -\frac{6}{r^4} \quad \text{or} \quad 3rB_2(r) - r^3B_3(r) \quad (\text{A.21})$$

$$t(r) = \frac{ds}{dr} = \frac{d^4f}{dr^4} = \frac{24}{r^5} \quad \text{or} \quad 3B_2(r) - 6r^2B_3(r) + r^4B_4(r) \quad (\text{A.22})$$

$$u(r) = \frac{dt}{dr} = \frac{d^5f}{dr^5} = -\frac{120}{r^6} \quad \text{or} \quad -15rB_3(r) + 10r^3B_4(r) - r^5B_5(r). \quad (\text{A.23})$$

For undamped charges, Table I lists these derivatives under the Bare Coulomb column. Eqs. (A.14) to (A.18) are still correct for GSF electrostatics if the subscript n is eliminated.

APPENDIX B

B.1 Contraction of the quadrupolar tensor with the traceless quadrupole moment

For quadrupolar liquids modeled using point quadrupoles, the interaction tensor is shown in Eq. (4.27). The Fourier transformation of this tensor for $\mathbf{k} = 0$ is,

$$\tilde{T}_{\alpha\beta\gamma\delta}(0) = \int_V T_{\alpha\beta\gamma\delta}(\mathbf{r}) d\mathbf{r} \quad (\text{B.1})$$

On the basis of symmetry, the 81 elements can be placed in four different groups: \tilde{T}_{aaaa} , \tilde{T}_{aaab} , \tilde{T}_{aabb} , and \tilde{T}_{abcb} , where a , b , and c , and can take on distinct values from the set $\{x, y, z\}$. The elements belonging to each of these groups can be obtained using permutations of the indices. Integration of all of the elements shows that only the groups with indices $aaaa$ and $aabb$ are non-zero.

We can derive values of the components of \tilde{T}_{aaaa} and \tilde{T}_{aabb} as follows;

$$\begin{aligned} \tilde{T}_{xxxx}(0) &= \int_V [3v_{41}(R) + 6x^2v_{42}(r)/r^2 + x^4v_{43}(r)/r^4] d\mathbf{r} \\ &= 12\pi \int_0^{r_c} \left[v_{41}(r) + \frac{2}{3}v_{42}(r) + \frac{1}{15}v_{43}(r) \right] r^2 dr = 12\pi B \end{aligned} \quad (\text{B.2})$$

and

$$\begin{aligned} \tilde{T}_{xxyy}(0) &= \int_V [v_{41}(R) + (x^2 + y^2)v_{42}(r)/r^2 + x^2y^2v_{43}(r)/r^4] d\mathbf{r} \\ &= 4\pi \int_0^{r_c} \left[v_{41}(r) + \frac{2}{3}v_{42}(r) + \frac{1}{15}v_{43}(r) \right] r^2 dr = 4\pi B. \end{aligned} \quad (\text{B.3})$$

These integrals yield the same values for all permutations of the indices in both tensor element groups. In Eq. 4.32, for a particular value of the quadrupolar polarization $\tilde{\Theta}_{aa}$ we can contract $\tilde{T}_{aa\gamma\delta}(0)$ with $\tilde{\Theta}_{\gamma\delta}$, using the traceless properties of the quadrupolar moment,

$$\begin{aligned}
\tilde{T}_{xx\gamma\delta}(0)\tilde{\Theta}_{\gamma\delta}(0) &= \tilde{T}_{xxxx}(0)\tilde{\Theta}_{xx}(0) + \tilde{T}_{xxyy}(0)\tilde{\Theta}_{yy}(0) + \tilde{T}_{xxzz}(0)\tilde{\Theta}_{zz}(0) \\
&= 12\pi B\tilde{\Theta}_{xx}(0) + 4\pi B\tilde{\Theta}_{yy}(0) + 4\pi B\tilde{\Theta}_{zz}(0) \\
&= 8\pi B\tilde{\Theta}_{xx}(0) + 4\pi B\left(\tilde{\Theta}_{xx}(0) + \tilde{\Theta}_{yy}(0) + \tilde{\Theta}_{zz}(0)\right) \\
&= 8\pi B\tilde{\Theta}_{xx}(0)
\end{aligned} \tag{B.4}$$

Similarly for a quadrupolar polarization $\tilde{\Theta}_{xy}$ in Eq. 4.32, we can contract $\tilde{T}_{xy\gamma\delta}(0)$ with $\tilde{\Theta}_{\gamma\delta}$, using the only surviving terms of the tensor,

$$\begin{aligned}
\tilde{T}_{xy\gamma\delta}(0)\tilde{\Theta}_{\gamma\delta}(0) &= \tilde{T}_{xyxy}(0)\tilde{\Theta}_{xy}(0) + \tilde{T}_{xyyx}(0)\tilde{\Theta}_{yx}(0) \\
&= 4\pi B\tilde{\Theta}_{xy}(0) + 4\pi B\tilde{\Theta}_{yx}(0) \\
&= 8\pi B\tilde{\Theta}_{xy}(0)
\end{aligned} \tag{B.5}$$

Here, we have used the symmetry of the quadrupole tensor to combine the symmetric terms. Therefore we can write matrix contraction for $\tilde{T}_{\alpha\beta\gamma\delta}(0)$ and $\tilde{\Theta}_{\gamma\delta}(0)$ in a general form,

$$\tilde{T}_{\alpha\beta\gamma\delta}(0)\tilde{\Theta}_{\gamma\delta}(0) = 8\pi B\tilde{\Theta}_{\alpha\beta}(0), \tag{B.6}$$

which is the same as Eq. (4.33).

When the molecular quadrupoles are represented by point charges, the symmetry of the quadrupolar tensor is same as for point quadrupoles (see Eqs. 4.24 and (4.27)). However, for molecular quadrupoles represented by point dipoles,

the symmetry of the quadrupolar tensor must be handled separately (compare Eqs. (4.26) and (4.27). Although there is a difference in symmetry, the final result (Eq. B.6) also holds true for dipolar representations.

B.2 Quadrupolar correction factor for the Ewald-Kornfeld (EK) method

The interaction tensor between two point quadrupoles in the Ewald method may be expressed,[64, 85]

$$\begin{aligned}
T_{\alpha\beta\gamma\delta}(\mathbf{r}) = & \frac{4\pi}{V} \sum_{k \neq 0}^{\infty} e^{-k^2/4\kappa^2} e^{-i\mathbf{k}\cdot\mathbf{r}} \left(\frac{r_\alpha r_\beta k_\delta k_\gamma}{k^2} \right) \\
& + (\delta_{\alpha\beta}\delta_{\gamma\delta} + \delta_{\alpha\gamma}\delta_{\beta\delta} + \delta_{\alpha\delta}\delta_{\beta\gamma}) B_2(r) \\
& - (\delta_{\gamma\delta}r_\alpha r_\beta + 5 \text{ permutations}) B_3(r) \\
& + (r_\alpha r_\beta r_\gamma r_\delta) B_4(r)
\end{aligned} \tag{B.7}$$

where $B_n(r)$ are radial functions defined in Ref. [64],

$$B_2(r) = \frac{3}{r^5} \left(\frac{2r\kappa e^{-r^2\kappa^2}}{\sqrt{\pi}} + \frac{4r^3\kappa^3 e^{-r^2\kappa^2}}{3\sqrt{\pi}} + \text{erfc}(\kappa r) \right) \tag{B.8}$$

$$B_3(r) = -\frac{15}{r^7} \left(\frac{2r\kappa e^{-r^2\kappa^2}}{\sqrt{\pi}} + \frac{4r^3\kappa^3 e^{-r^2\kappa^2}}{3\sqrt{\pi}} + \frac{8r^5\kappa^5 e^{-r^2\kappa^2}}{15\sqrt{\pi}} + \text{erfc}(\kappa r) \right) \tag{B.9}$$

$$\begin{aligned}
B_4(r) = & \frac{105}{r^9} \left(\frac{2r\kappa e^{-r^2\kappa^2}}{\sqrt{\pi}} + \frac{4r^3\kappa^3 e^{-r^2\kappa^2}}{3\sqrt{\pi}} + \frac{8r^5\kappa^5 e^{-r^2\kappa^2}}{15\sqrt{\pi}} \right. \\
& \left. + \frac{16r^7\kappa^7 e^{-r^2\kappa^2}}{105\sqrt{\pi}} + \text{erfc}(\kappa r) \right)
\end{aligned} \tag{B.10}$$

We can divide $T_{\alpha\beta\gamma\delta}(\mathbf{r})$ into three parts:

$$\mathbf{T}(\mathbf{r}) = \mathbf{T}^K(\mathbf{r}) + \mathbf{T}^{R1}(\mathbf{r}) + \mathbf{T}^{R2}(\mathbf{r}) \tag{B.11}$$

where the first term is the reciprocal space portion. Since the quadrupolar correction factor $B = \tilde{T}_{abab}(0)/4\pi$ and $\mathbf{k} = 0$ is excluded from the reciprocal space sum, \mathbf{T}^K will not contribute.[85] The remaining terms,

$$\begin{aligned} \mathbf{T}^{R1}(\mathbf{r}) = & \mathbf{T}^{\text{bare}}(\mathbf{r}) \left(\frac{2r\kappa e^{-r^2\kappa^2}}{\sqrt{\pi}} + \frac{4r^3\kappa^3 e^{-r^2\kappa^2}}{3\sqrt{\pi}} + \frac{8r^5\kappa^5 e^{-r^2\kappa^2}}{15\sqrt{\pi}} \right. \\ & \left. + \frac{16r^7\kappa^7 e^{-r^2\kappa^2}}{105\sqrt{\pi}} + \text{erfc}(\kappa r) \right) \end{aligned} \quad (\text{B.12})$$

and

$$\begin{aligned} T_{\alpha\beta\gamma\delta}^{\text{R2}}(\mathbf{r}) = & (\delta_{\gamma\delta}r_\alpha r_\beta + 5 \text{ permutations}) \frac{16\kappa^7 e^{-r^2\kappa^2}}{7\sqrt{\pi}} \\ & - (\delta_{\alpha\beta}\delta_{\gamma\delta} + \delta_{\alpha\gamma}\delta_{\beta\delta} + \delta_{\alpha\delta}\delta_{\beta\gamma}) \left(\frac{8\kappa^5 e^{-r^2\kappa^2}}{5\sqrt{\pi}} + \frac{16r^2\kappa^7 e^{-r^2\kappa^2}}{35\sqrt{\pi}} \right) \end{aligned} \quad (\text{B.13})$$

are contributions from the real space sum.[1, 3, 101] Here $\mathbf{T}^{\text{bare}}(\mathbf{r})$ is the unmodified quadrupolar tensor (for undamped quadrupoles). Due to the angular symmetry of the unmodified tensor, the integral of $\mathbf{T}^{R1}(\mathbf{r})$ will vanish when integrated over a spherical region. The only term contributing to the correction factor (B) is therefore $T_{\alpha\beta\gamma\delta}^{\text{R2}}(\mathbf{r})$, which allows us to derive the correction factor for the Ewald-Kornfeld (EK) method,

$$\begin{aligned} B &= \frac{1}{4\pi} \int_V T_{abab}^{\text{R2}}(\mathbf{r}) \\ &= -\frac{8r_c^3\kappa^5 e^{-\kappa^2 r_c^2}}{15\sqrt{\pi}} \end{aligned} \quad (\text{B.14})$$

which is essentially identical with the correction factor from the direct spherical cutoff (SC) method.

B.3 Generating Uniform Field Gradients

One important task in carrying out the simulations mentioned in the Chapter 4 was to generate uniform electric field gradients. To do this, we relied heavily on both the notation and results from Torres del Castillo and Mendéz Garido.[102] In this work, tensors were expressed in Cartesian components, using at times a dyadic notation. This proves quite useful for computer simulations that make use of toroidal boundary conditions.

An alternative formalism uses the theory of angular momentum and spherical harmonics and is common in standard physics texts such as Jackson,[103] Morse and Feshbach,[104] and Stone.[105] Because this approach has its own advantages, relationships are provided below comparing that terminology to the Cartesian tensor notation.

The gradient of the electric field is given by

$$\mathbf{G}(\mathbf{r}) = -\nabla\nabla\Phi(\mathbf{r}),$$

where $\Phi(\mathbf{r})$ is the electrostatic potential. In a charge-free region of space, $\nabla\cdot\mathbf{E} = 0$, and \mathbf{G} is a symmetric traceless tensor. From symmetry arguments, we know that this tensor can be written in terms of just five independent components.

Following Torres del Castillo and Mendéz Garido's notation, the gradient of the electric field may also be written in terms of two vectors \mathbf{a} and \mathbf{b} ,

$$G_{ij} = \frac{1}{2}(a_i b_j + a_j b_i) - \frac{1}{3}(\mathbf{a} \cdot \mathbf{b})\delta_{ij}.$$

If the vectors \mathbf{a} and \mathbf{b} are unit vectors, the electrostatic potential that generates

a uniform gradient may be written:

$$\begin{aligned} \Phi(x, y, z) = & -\frac{g_o}{2} \left(\left(a_1 b_1 - \frac{\cos\psi}{3} \right) x^2 + \left(a_2 b_2 - \frac{\cos\psi}{3} \right) y^2 + \left(a_3 b_3 - \frac{\cos\psi}{3} \right) z^2 \right. \\ & \left. + (a_1 b_2 + a_2 b_1) xy + (a_1 b_3 + a_3 b_1) xz + (a_2 b_3 + a_3 b_2) yz \right). \end{aligned} \quad (\text{B.15})$$

Note $\mathbf{a} \cdot \mathbf{a} = \mathbf{b} \cdot \mathbf{b} = 1$, $\mathbf{a} \cdot \mathbf{b} = \cos\psi$, and g_0 is the overall strength of the potential.

Taking the gradient of Eq. (B.15), we find the field due to this potential,

$$\mathbf{E} = -\nabla\Phi = \frac{g_o}{2} \begin{pmatrix} 2(a_1 b_1 - \frac{\cos\psi}{3}) x & + (a_1 b_2 + a_2 b_1) y & + (a_1 b_3 + a_3 b_1) z \\ (a_2 b_1 + a_1 b_2) x & + 2(a_2 b_2 - \frac{\cos\psi}{3}) y & + (a_2 b_3 + a_3 b_3) z \\ (a_3 b_1 + a_3 b_2) x & + (a_3 b_2 + a_2 b_3) y & + 2(a_3 b_3 - \frac{\cos\psi}{3}) z \end{pmatrix}, \quad (\text{B.16})$$

while the gradient of the electric field in this form,

$$\mathbf{G} = \nabla\mathbf{E} = \frac{g_o}{2} \begin{pmatrix} 2(a_1 b_1 - \frac{\cos\psi}{3}) & (a_1 b_2 + a_2 b_1) & (a_1 b_3 + a_3 b_1) \\ (a_2 b_1 + a_1 b_2) & 2(a_2 b_2 - \frac{\cos\psi}{3}) & (a_2 b_3 + a_3 b_3) \\ (a_3 b_1 + a_3 b_2) & (a_3 b_2 + a_2 b_3) & 2(a_3 b_3 - \frac{\cos\psi}{3}) \end{pmatrix}, \quad (\text{B.17})$$

is uniform over the entire space. Therefore, to describe a uniform gradient in this notation, two unit vectors (\mathbf{a} and \mathbf{b}) as well as a potential strength, g_0 , must be specified. As expected, this requires five independent parameters.

The common alternative to the Cartesian notation expresses the electrostatic potential using the notation of Morse and Feshbach,[104]

$$\Phi(x, y, z) = - \left[a_{20} \frac{2z^2 - x^2 - y^2}{2} + 3a_{21}^e xz + 3a_{21}^o yz + 6a_{22}^e xy + 3a_{22}^o (x^2 - y^2) \right]. \quad (\text{B.18})$$

Here we use the standard (l, m) form for the a_{lm} coefficients, with superscript e and o denoting even and odd, respectively. This form makes the functional analogy to “d” atomic states apparent.

Applying the gradient operator to Eq. (B.18) the electric field due to this potential,

$$\mathbf{E} = -\nabla\Phi = \begin{pmatrix} (6a_{22}^o - a_{20}) x & + 6a_{22}^e y & + 3a_{21}^e z \\ 6a_{22}^e x & - (a_{20} + 6a_{22}^o) y & + 3a_{21}^o z \\ 3a_{21}^e x & + 3a_{21}^o y & + 2a_{20} z \end{pmatrix}, \quad (\text{B.19})$$

while the gradient of the electric field in this form is:

$$\mathbf{G} = \begin{pmatrix} 6a_{22}^o - a_{20} & 6a_{22}^e & 3a_{21}^e \\ 6a_{22}^e & -(a_{20} + 6a_{22}^o) & 3a_{21}^o \\ 3a_{21}^e & 3a_{21}^o & 2a_{20} \end{pmatrix} \quad (\text{B.20})$$

which is also uniform over the entire space. This form for the gradient can be factored as

$$\begin{aligned} \mathbf{G} = a_{20} \begin{pmatrix} -1 & 0 & 0 \\ 0 & -1 & 0 \\ 0 & 0 & 2 \end{pmatrix} + 3a_{21}^e \begin{pmatrix} 0 & 0 & 1 \\ 0 & 0 & 0 \\ 1 & 0 & 0 \end{pmatrix} + 3a_{21}^o \begin{pmatrix} 0 & 0 & 0 \\ 0 & 0 & 1 \\ 0 & 1 & 0 \end{pmatrix} \\ + 6a_{22}^e \begin{pmatrix} 0 & 1 & 0 \\ 1 & 0 & 0 \\ 0 & 0 & 0 \end{pmatrix} + 6a_{22}^o \begin{pmatrix} 1 & 0 & 0 \\ 0 & -1 & 0 \\ 0 & 0 & 0 \end{pmatrix}. \end{aligned} \quad (\text{B.21})$$

The five matrices in the expression above represent five different symmetric traceless tensors of rank 2.

It is useful to find the Cartesian vectors \mathbf{a} and \mathbf{b} that generate the five types of tensors shown in Eq. (B.21). If the two vectors are co-linear, e.g., $\psi = 0$, $\mathbf{a} = (0, 0, 1)$ and $\mathbf{b} = (0, 0, 1)$, then

$$\mathbf{G} = \frac{g_0}{3} \begin{pmatrix} -1 & 0 & 0 \\ 0 & -1 & 0 \\ 0 & 0 & 2 \end{pmatrix},$$

which is the a_{20} symmetry. To generate the a_{22}^o symmetry, we take: $\mathbf{a} = (\frac{1}{\sqrt{2}}, \frac{1}{\sqrt{2}}, 0)$ and $\mathbf{b} = (\frac{1}{\sqrt{2}}, -\frac{1}{\sqrt{2}}, 0)$ and find:

$$\mathbf{G} = \frac{g_0}{2} \begin{pmatrix} 1 & 0 & 0 \\ 0 & -1 & 0 \\ 0 & 0 & 0 \end{pmatrix}.$$

To generate the a_{22}^e symmetry, we take: $\mathbf{a} = (1, 0, 0)$ and $\mathbf{b} = (0, 1, 0)$ and find:

$$\mathbf{G} = \frac{g_0}{2} \begin{pmatrix} 0 & 1 & 0 \\ 1 & 0 & 0 \\ 0 & 0 & 0 \end{pmatrix}.$$

The pattern is straightforward to continue for the other symmetries.

We find the notation of Ref. [102] helpful when creating specific types of constant gradient electric fields in simulations. For this reason, Eqs. (B.15), (B.16), and (B.17) are implemented in our code. In the simulations using constant applied gradients that are mentioned in the main text, we utilized a field with the a_{22}^e symmetry using vectors, $\mathbf{a} = (1, 0, 0)$ and $\mathbf{b} = (0, 1, 0)$.

B.4 Point-multipolar interactions with a spatially-varying electric field

This section develops formulas for the force and torque exerted by an external electric field, $\mathbf{E}(\mathbf{r})$, on object a . [106] Object a has an embedded collection of charges and in simulations will represent a molecule, ion, or a coarse-grained substructure. We describe the charge distributions using primitive multipoles defined in Ref. [62] by

$$C_a = \sum_{k \text{ in } a} q_k, \quad (\text{B.22})$$

$$D_{a\alpha} = \sum_{k \text{ in } a} q_k r_{k\alpha}, \quad (\text{B.23})$$

$$Q_{a\alpha\beta} = \frac{1}{2} \sum_{k \text{ in } a} q_k r_{k\alpha} r_{k\beta}, \quad (\text{B.24})$$

where \mathbf{r}_k is the local coordinate system for the object (usually the center of mass of object a). Components of vectors and tensors are given using the Einstein repeated summation notation. Note that the definition of the primitive quadrupole here differs from the standard traceless form, and contains an additional Taylor-series based factor of 1/2. In Ref. [62], we derived the forces and torques each object exerts on the other objects in the system.

Here we must also consider an external electric field that varies in space: $\mathbf{E}(\mathbf{r})$. Each of the local charges q_k in object a will then experience a slightly different field. This electric field can be expanded in a Taylor series around the local origin of each object. For a particular charge q_k , the electric field at that site's position is given by:

$$\mathbf{E}(\mathbf{r}_k) = E_\gamma|_{\mathbf{r}_k=0} + \nabla_\delta E_\gamma|_{\mathbf{r}_k=0} r_{k\delta} + \frac{1}{2} \nabla_\delta \nabla_\epsilon E_\gamma|_{\mathbf{r}_k=0} r_{k\delta} r_{k\epsilon} + \dots \quad (\text{B.25})$$

Note that if one shrinks object a to a single point, the E_γ terms are all evaluated at the center of the object (now a point). Thus later the E_γ terms can be written using the same (molecular) origin for all point charges in the object. The force exerted on object a by the electric field is given by,

$$F_\gamma^a = \sum_{k \text{ in } a} q_k E_\gamma(\mathbf{r}_k) = \sum_{k \text{ in } a} q_k \{E_\gamma + \nabla_\delta E_\gamma r_{k\delta} + \frac{1}{2} \nabla_\delta \nabla_\varepsilon E_\gamma r_{k\delta} r_{k\varepsilon} + \dots\} \quad (\text{B.26})$$

$$= C_a E_\gamma + D_{a\delta} \nabla_\delta E_\gamma + Q_{a\delta\varepsilon} \nabla_\delta \nabla_\varepsilon E_\gamma + \dots \quad (\text{B.27})$$

Thus in terms of the global origin \mathbf{r} , $F_\gamma(\mathbf{r}) = C E_\gamma(\mathbf{r})$ etc.

Similarly, the torque exerted by the field on a can be expressed as

$$\tau_\alpha^a = \sum_{k \text{ in } a} (\mathbf{r}_k \times q_k \mathbf{E})_\alpha \quad (\text{B.28})$$

$$= \sum_{k \text{ in } a} \epsilon_{\alpha\beta\gamma} q_k r_{k\beta} E_\gamma(\mathbf{r}_k) \quad (\text{B.29})$$

$$= \epsilon_{\alpha\beta\gamma} D_\beta E_\gamma + 2\epsilon_{\alpha\beta\gamma} Q_{\beta\delta} \nabla_\delta E_\gamma + \dots \quad (\text{B.30})$$

We note that the Levi-Civita symbol can be eliminated by utilizing the matrix cross product as defined in Ref. [64]:

$$[\mathbf{A} \times \mathbf{B}]_\alpha = \sum_\beta [\mathbf{A}_{\alpha+1,\beta} \mathbf{B}_{\alpha+2,\beta} - \mathbf{A}_{\alpha+2,\beta} \mathbf{B}_{\alpha+1,\beta}] \quad (\text{B.31})$$

where $\alpha + 1$ and $\alpha + 2$ are regarded as cyclic permutations of the matrix indices. Finally, the interaction energy U^a of object a with the external field is given by,

$$U^a = \sum_{k \text{ in } a} q_k \phi_k(\mathbf{r}_k) \quad (\text{B.32})$$

TABLE B.1

Potential energy (U), force (\mathbf{F}), and torque (τ) expressions for a multipolar site at \mathbf{r} in an electric field, $\mathbf{E}(\mathbf{r})$ using the definitions of the multipoles in Eqs. (B.22), (B.23) and (B.24).

	Charge	Dipole	Quadrupole
$U(\mathbf{r})$	$C\phi(\mathbf{r})$	$-\mathbf{D} \cdot \mathbf{E}(\mathbf{r})$	$-\mathbf{Q} : \nabla \mathbf{E}(\mathbf{r})$
$\mathbf{F}(\mathbf{r})$	$C\mathbf{E}(\mathbf{r})$	$\mathbf{D} \cdot \nabla \mathbf{E}(\mathbf{r})$	$\mathbf{Q} : \nabla \nabla \mathbf{E}(\mathbf{r})$
$\tau(\mathbf{r})$		$\mathbf{D} \times \mathbf{E}(\mathbf{r})$	$2\mathbf{Q} \times \nabla \mathbf{E}(\mathbf{r})$

Performing another Taylor series expansion about the local body origin,

$$\phi(\mathbf{r}_k) = \phi|_{\mathbf{r}_k=0} + r_{k\alpha} \nabla_\alpha \phi|_{\mathbf{r}_k=0} + \frac{1}{2} r_{k\alpha} r_{k\beta} \nabla_\alpha \nabla_\beta \phi|_{\mathbf{r}_k=0} + \dots \quad (\text{B.33})$$

Writing this in terms of the global origin \mathbf{r} , we find

$$U(\mathbf{r}) = C\phi(\mathbf{r}) - \mathbf{D}_\alpha \mathbf{E}_\alpha - \mathbf{Q}_{\alpha\beta} \nabla_\alpha \mathbf{E}_\beta + \dots \quad (\text{B.34})$$

These results have been summarized in Table B.1.

B.5 Boltzmann averages for orientational polarization

If we consider a collection of molecules in the presence of external field, the perturbation experienced by any one molecule will include contributions to the field or field gradient produced by the all other molecules in the system. In subsections B.5.1 and B.5.2, we discuss the molecular polarization due solely to external field perturbations. This illustrates the origins of the polarizability Eqs. (4.3,4.2, 4.17

and 4.18).

B.5.1 Dipoles

Consider a system of molecules, each with permanent dipole moment p_o . In the absence of an external field, thermal agitation orients the dipoles randomly, and the system moment, \mathbf{P} , is zero. External fields will line up the dipoles in the direction of applied field. Here we consider the net field from all other molecules to be zero. Therefore the total Hamiltonian acting on each molecule is,[103]

$$H = H_o - \mathbf{p}_o \cdot \mathbf{E}, \quad (\text{B.35})$$

where H_o is a function of the internal coordinates of the molecule. The Boltzmann average of the dipole moment in the direction of the field is given by,

$$\langle p_{mol} \rangle = \frac{\int p_o \cos \theta e^{p_o E \cos \theta / k_B T} d\Omega}{\int e^{p_o E \cos \theta / k_B T} d\Omega}, \quad (\text{B.36})$$

where the z -axis is taken in the direction of the applied field, \mathbf{E} and $\int d\Omega = \int_0^\pi \sin \theta d\theta \int_0^{2\pi} d\phi \int_0^{2\pi} d\psi$ is an integration over Euler angles describing the orientation of the molecule.

If the external fields are small, *i.e.* $p_o E \cos \theta / k_B T \ll 1$,

$$\langle p_{mol} \rangle \approx \frac{p_o^2}{3k_B T} E, \quad (\text{B.37})$$

where $\alpha_p = \frac{p_o^2}{3k_B T}$ is the molecular polarizability. The orientational polarization depends inversely on the temperature as the applied field must overcome thermal agitation to orient the dipoles.

B.5.2 Quadrupoles

If instead, our system consists of molecules with permanent *quadrupole* tensor $q_{\alpha\beta}$. The average quadrupole at temperature T in the presence of uniform applied field gradient is given by,[93, 94]

$$\langle q_{\alpha\beta} \rangle = \frac{\int q_{\alpha\beta} e^{-H/k_B T} d\Omega}{\int e^{-H/k_B T} d\Omega} = \frac{\int q_{\alpha\beta} e^{q_{\mu\nu} \partial_\nu E_\mu / k_B T} d\Omega}{\int e^{q_{\mu\nu} \partial_\nu E_\mu / k_B T} d\Omega}, \quad (\text{B.38})$$

where $H = H_o - q_{\mu\nu} \partial_\nu E_\mu$ is the energy of a quadrupole in the gradient of the applied field and H_o is a function of internal coordinates of the molecule. The energy and quadrupole moment can be transformed into the body frame using a rotation matrix η^{-1} ,

$$q_{\alpha\beta} = \eta_{\alpha\alpha'} \eta_{\beta\beta'} q_{\alpha'\beta'}^* \quad (\text{B.39})$$

$$H = H_o - q : \nabla \mathbf{E} \quad (\text{B.40})$$

$$= H_o - q_{\mu\nu} \partial_\nu E_\mu \quad (\text{B.41})$$

$$= H_o - \eta_{\mu\mu'} \eta_{\nu\nu'} q_{\mu'\nu'}^* \partial_\nu E_\mu. \quad (\text{B.42})$$

Here the starred tensors are the components in the body fixed frame. Substituting Eq. (B.42) in the Eq. (B.38) and taking linear terms in the expansion we obtain,

$$\langle q_{\alpha\beta} \rangle = \frac{\int q_{\alpha\beta} \left(1 + \frac{\eta_{\mu\mu'} \eta_{\nu\nu'} q_{\mu'\nu'}^* \partial_\nu E_\mu}{k_B T} \right) d\Omega}{\int \left(1 + \frac{\eta_{\mu\mu'} \eta_{\nu\nu'} q_{\mu'\nu'}^* \partial_\nu E_\mu}{k_B T} \right) d\Omega}. \quad (\text{B.43})$$

Note that $\eta_{\alpha\alpha'}$ is the inverse of the rotation matrix that transforms the body fixed coordinates to the space coordinates.

Integration of the first and second terms in the denominator gives $8\pi^2$ and $8\pi^2(\nabla \cdot \mathbf{E})\text{Tr}(q^*)/3$ respectively. The second term vanishes for charge free space (where $\nabla \cdot \mathbf{E} = 0$). Similarly, integration of the first term in the numerator produces $8\pi^2\delta_{\alpha\beta}\text{Tr}(q^*)/3$ and second produces $8\pi^2(3q_{\alpha'\beta'}^*q_{\beta'\alpha'}^* - q_{\alpha'\alpha'}^*q_{\beta'\beta'}^*)\partial_\alpha E_\beta/15k_B T$. Therefore the Boltzmann average of a quadrupole moment can be written as,

$$\langle q_{\alpha\beta} \rangle = \frac{1}{3}\text{Tr}(q^*) \delta_{\alpha\beta} + \frac{\bar{q}_o^2}{15k_B T} \partial_\alpha E_\beta, \quad (\text{B.44})$$

where $\alpha_q = \frac{\bar{q}_o^2}{15k_B T}$ is a molecular quadrupole polarizability and $\bar{q}_o^2 = 3q_{\alpha'\beta'}^*q_{\beta'\alpha'}^* - q_{\alpha'\alpha'}^*q_{\beta'\beta'}^*$ is the square of the net quadrupole moment of a molecule.

B.6 Gradient of the field due to quadrupolar polarization

In section IV.C of the Chapter 4, we stated that for quadrupolar fluids, the self-contribution to the field gradient vanishes at the singularity. In this section, we prove this statement. For this purpose, we consider a distribution of charge $\rho(\mathbf{r})$ which gives rise to an electric field $\mathbf{E}(\mathbf{r})$ and gradient of the field $\nabla\mathbf{E}(\mathbf{r})$ throughout space. The gradient of the electric field over volume due to the charges within the sphere of radius R is given by (cf. Ref. [103], Eq. 4.14):

$$\int_{r < R} \nabla\mathbf{E} d\mathbf{r} = - \int_{r=R} R^2 \mathbf{E} \hat{n} d\Omega \quad (\text{B.45})$$

where $d\Omega$ is the solid angle and \hat{n} is the normal vector of the surface of the sphere,

$$\hat{n} = \sin\theta \cos\phi \hat{x} + \sin\theta \sin\phi \hat{y} + \cos\theta \hat{z} \quad (\text{B.46})$$

in spherical coordinates. For the charge density $\rho(\mathbf{r}')$, the total gradient of the electric field can be written as,[103]

$$\int_{r < R} \nabla \mathbf{E} \, d\mathbf{r} = - \int_{r=R} R^2 \nabla \Phi \, \hat{n} \, d\Omega = - \frac{1}{4\pi \epsilon_o} \int_{r=R} R^2 \nabla \left(\int \frac{\rho(\mathbf{r}')}{|\mathbf{r} - \mathbf{r}'|} \, d\mathbf{r}' \right) \hat{n} \, d\Omega. \quad (\text{B.47})$$

The radial function in the Eq. (B.47) can be expressed in terms of spherical harmonics as,[103]

$$\frac{1}{|\mathbf{r} - \mathbf{r}'|} = 4\pi \sum_{l=0}^{\infty} \sum_{m=-l}^{m=l} \frac{1}{2l+1} \frac{r_{<}^l}{r_{>}^{l+1}} Y_{lm}^*(\theta', \phi') Y_{lm}(\theta, \phi) \quad (\text{B.48})$$

If the sphere completely encloses the charge density then $r_{<} = r'$ and $r_{>} = R$. Substituting Eq. (B.48) into (B.47) we get,

$$\begin{aligned} \int_{r < R} \nabla \mathbf{E} \, d\mathbf{r} &= - \frac{R^2}{\epsilon_o} \int_{r=R} \nabla \left(\int \rho(\mathbf{r}') \sum_{l=0}^{\infty} \sum_{m=-l}^{m=l} \frac{1}{2l+1} \frac{r^l}{R^{l+1}} \right. \\ &\quad \left. Y_{lm}^*(\theta', \phi') Y_{lm}(\theta, \phi) \, d\mathbf{r}' \right) \hat{n} \, d\Omega \\ &= - \frac{R^2}{\epsilon_o} \sum_{l=0}^{\infty} \sum_{m=-l}^{m=l} \frac{1}{2l+1} \int \rho(\mathbf{r}') r^l Y_{lm}^*(\theta', \phi') \\ &\quad \left(\int_{r=R} \vec{\nabla} (R^{-(l+1)} Y_{lm}(\theta, \phi)) \hat{n} \, d\Omega \right) d\mathbf{r}'. \end{aligned} \quad (\text{B.49})$$

The gradient of the product of radial function and spherical harmonics is given by:[107]

$$\begin{aligned} \nabla [f(r) Y_{lm}(\theta, \phi)] &= - \left(\frac{l+1}{2l+1} \right)^{1/2} \left[\frac{\partial}{\partial r} - \frac{l}{r} \right] f(r) Y_{l,l+1,m}(\theta, \phi) \\ &\quad + \left(\frac{l}{2l+1} \right)^{1/2} \left[\frac{\partial}{\partial r} + \frac{l}{r} \right] f(r) Y_{l,l-1,m}(\theta, \phi). \end{aligned} \quad (\text{B.50})$$

where $Y_{l,l+1,m}(\theta, \phi)$ is a vector spherical harmonic.[107] Using Eq. (B.50) we get,

$$\nabla (R^{-(l+1)} Y_{lm}(\theta, \phi)) = [(l+1)(2l+1)]^{1/2} Y_{l,l+1,m}(\theta, \phi) \frac{1}{R^{l+2}}, \quad (\text{B.51})$$

Using Clebsch-Gordan coefficients $C(l+1, 1, l|m_1, m_2, m)$, the vector spherical harmonics can be written in terms of spherical harmonics,

$$Y_{l,l+1,m}(\theta, \phi) = \sum_{m_1, m_2} C(l+1, 1, l|m_1, m_2, m) Y_{l+1}^{m_1}(\theta, \phi) \hat{e}_{m_2}. \quad (\text{B.52})$$

Here \hat{e}_{m_2} is a spherical tensor of rank 1 which can be expressed in terms of Cartesian coordinates,

$$\hat{e}_{+1} = -\frac{\hat{x} + i\hat{y}}{\sqrt{2}}, \quad \hat{e}_0 = \hat{z}, \quad \text{and} \quad \hat{e}_{-1} = \frac{\hat{x} - i\hat{y}}{\sqrt{2}}. \quad (\text{B.53})$$

The normal vector \hat{n} is then expressed in terms of spherical tensor of rank 1 as shown in below,

$$\hat{n} = \sqrt{\frac{4\pi}{3}} (-Y_1^{-1}\hat{e}_1 - Y_1^1\hat{e}_{-1} + Y_1^0\hat{e}_0). \quad (\text{B.54})$$

The surface integral of the product of \hat{n} and $Y_{l+1}^{m_1}(\theta, \phi)$ gives,

$$\begin{aligned} \int \hat{n} Y_{l+1}^{m_1} d\Omega &= \int \sqrt{\frac{4\pi}{3}} (-Y_1^{-1}\hat{e}_1 - Y_1^1\hat{e}_{-1} + Y_1^0\hat{e}_0) Y_{l+1}^{m_1} d\Omega \\ &= \int \sqrt{\frac{4\pi}{3}} (Y_1^{1*}\hat{e}_1 + Y_1^{-1*}\hat{e}_{-1} + Y_1^{0*}\hat{e}_0) Y_{l+1}^{m_1} d\Omega \\ &= \sqrt{\frac{4\pi}{3}} (\delta_{l+1,1} \delta_{1,m_1} \hat{e}_1 + \delta_{l+1,1} \delta_{-1,m_1} \hat{e}_{-1} + \delta_{l+1,1} \delta_{0,m_1} \hat{e}_0), \end{aligned} \quad (\text{B.55})$$

where $Y_l^{-m} = (-1)^m Y_l^{m*}$ and $\int Y_l^{m*} Y_{l'}^{m'} d\Omega = \delta_{ll'} \delta_{mm'}$. Non-vanishing values of Eq. B.55 require $l = 0$, therefore the value of $m = 0$. Since the values of m_1 are -1, 1, and 0 then m_2 takes the values 1, -1, and 0, respectively provided that

$m = m_1 + m_2$. Eq. B.49 can therefore be modified,

$$\begin{aligned}
\int_{r < R} \nabla \mathbf{E} \, d\mathbf{r} &= -\sqrt{\frac{4\pi}{3}} \frac{1}{\epsilon_o} \int \rho(r') Y_{00}^*(\theta', \phi') [C(1, 1, 0 | -1, 1, 0) \hat{e}_{-1} \hat{e}_1 \\
&\quad + C(1, 1, 0 | -1, 1, 0) \hat{e}_1 \hat{e}_{-1} + C(1, 1, 0 | 0, 0, 0) \hat{e}_0 \hat{e}_0] \, d\mathbf{r}' \\
&= -\sqrt{\frac{4\pi}{3}} \frac{1}{\epsilon_o} \int \rho(r') \, d\mathbf{r}' (\hat{e}_{-1} \hat{e}_1 + \hat{e}_1 \hat{e}_{-1} - \hat{e}_0 \hat{e}_0) \\
&= -\sqrt{\frac{4\pi}{3}} \frac{1}{\epsilon_o} C_{\text{total}} (\hat{e}_{-1} \hat{e}_1 + \hat{e}_1 \hat{e}_{-1} - \hat{e}_0 \hat{e}_0).
\end{aligned} \tag{B.56}$$

In the last step, the charge density was integrated over the sphere, yielding a total charge C_{total} . Eq. (B.56) gives the total gradient of the field over a sphere due to the distribution of the charges. For quadrupolar fluids the total charge within a sphere is zero, therefore $\int_{r < R} \nabla \mathbf{E} \, d\mathbf{r} = 0$. Hence the quadrupolar polarization produces zero net gradient of the field inside the sphere.

B.7 Quadrupole tensors and electric field gradients

In this section of this appendix, useful relationships for quadrupole tensors and electric field gradients are derived. We use heavily both the notation and results from Torres del Castillo and Mendéz Garido (Ref. [102]). In this reference, tensors are expressed in Cartesian components, using at times a dyadic notation. This proves to be useful for our work since in simulations, we frequently will want to use toroidal boundary conditions, which are much more easily implemented using Cartesian coordinate systems.

An alternative formalism uses the theory of angular momentum and spherical harmonics; e.g., see standard physics texts such as Jackson, Morse and Feshbach. Because this approach has its own advantages, relationships are provided below comparing that terminology to the tensor notation.

B.7.1 General results

In calculations, we have defined both a traced quadrupole tensor

$$Q_{\alpha\beta} = \frac{1}{2} \sum_k q_k r_{k\alpha} r_{k\beta} = \frac{1}{2} \int r'_i r'_j \rho(\mathbf{r}') d^3 r'$$

and a traceless form:

$$\Theta_{\alpha\beta} = 3Q_{\alpha\beta} - \delta_{\alpha\beta} \text{Tr} \mathbf{Q}.$$

Here, we continue to use notation and results from Torres del Castillo and Mendez Gardio [102]

$$Q_{ij}^C = \int (3r'_i r'_j - r'^2 \delta_{ij}) \rho(\mathbf{r}') d^3 r' = 2\Theta_{ij},$$

in order to discuss generalized forms of traceless tensors \mathbf{Q}^C and the gradients of the electric field. In their notation,

$$\mathbf{G} = -\nabla_i \nabla_j \Phi(\mathbf{r})|_{\mathbf{r}=0},$$

where $\Phi(\mathbf{r})$ is the electrostatic potential. Since in a charge-free region of space, $\nabla \cdot \mathbf{E} = 0$, both \mathbf{Q}^C and \mathbf{G} are symmetric traceless tensors. From symmetry arguments, we know that each tensor can be written in terms of just five independent components. We choose these when needed to be Q_{11}^C , Q_{22}^C , Q_{12}^C , Q_{13}^C , and Q_{23}^C and G_{11} , G_{22} , G_{12} , G_{13} , and G_{23} . A better way to characterize these tensors is in terms of their eigenvalues, which are all real, and eigenvectors, which are real and can be made to be orthonormal. Following Ref. [102], the eigenvalues and eigenvectors of \mathbf{Q} are written respectively in the order λ , μ , and ν and \hat{X} , \hat{Y} , and \hat{Z} , where the eigenvalues are named in the order $\lambda \geq \nu \geq \mu$. Thus a preferred plane XY is singled out by the largest and smallest eigenvalue. A similar notation

(with primes) is used for \mathbf{G} , $\lambda' \geq \nu' \geq \mu'$. Thus the traceless condition is written $\lambda + \mu + \nu = 0$ and $\lambda' + \mu' + \nu' = 0$ and the two tensors are represented by:

$$Q_{ij}^C = \lambda \hat{X}_i \hat{X}_j + \mu \hat{Y}_i \hat{Y}_j + \nu \hat{Z}_i \hat{Z}_j \quad \text{and} \quad G_{ij} = \lambda' \hat{X}'_i \hat{X}'_j + \mu' \hat{Y}'_i \hat{Y}'_j + \nu' \hat{Z}'_i \hat{Z}'_j.$$

Using again the notation of Ref. [102], the interaction energy of a quadrupole \mathbf{Q}^C with the gradient of the electric field \mathbf{G} is

$$U = -\frac{1}{6} \sum_{i,j} G_{ij} Q_{ij}^C.$$

Assuming that \mathbf{G} is written in the space frame, generally one would need to transform \mathbf{Q}^C from body to space frame:

$$Q_{ij}^C = \eta_{ii'} \eta_{jj'} Q_{i'j'}^{C*}.$$

Natural coordinates for the body frame of \mathbf{Q}^C are its eigenvectors.

Now a single quadrupole can be considered to be embedded in the gradient of an electric field. Torres del Castillo and Mendéz Garido have shown that the lowest energy state is the one where the eigenvector axes align with each other; \hat{X} with \hat{X}' , \hat{Y} with \hat{Y}' , and \hat{Z} with \hat{Z}' . For that case of idealized alignment, tensor \mathbf{Q}^C will be in its body frame. Thus

$$U = -\frac{1}{6}(\lambda\lambda' + \mu\mu' + \nu\nu').$$

This equation is used below in the derivation of the quadrupolar scaling factor B .

B.7.2 Special cases of quadrupole tensors

Any general quadrupole can be written in terms of position vectors \mathbf{c} and \mathbf{d} which go from one negative charge $-q$ to the two positive charges q , thus forming two of the sides of a parallelogram:

$$Q_{ij}^C = 3q(c_i d_j + c_j d_i) - 2q(\mathbf{c} \cdot \mathbf{d})\delta_{ij}.$$

Placing the origin at the center of the parallelogram that is in the xy plane, charges $-q$ and q are located at $\pm(\mathbf{c} + \mathbf{d})/2$ and $\pm(\mathbf{c} - \mathbf{d})/2$, respectively;

$$\mathbf{Q}^C = 2q \begin{pmatrix} 2c_x d_x - c_y d_y & 3(c_x d_y + c_y d_x) & 0 \\ 3(c_x d_y + c_y d_x) & 2c_y d_y - c_x d_x & 0 \\ 0 & 0 & -(c_x d_x + c_y d_y) \end{pmatrix}.$$

As discussed previously, this tensor will have three distinct eigenvalues; in Ref. [102] this is rewritten by eliminating the middle eigenvalue ν and its eigenvector \hat{Z} , which leads to the form

$$Q_{ij}^C = (2\lambda + \mu)\hat{X}_i\hat{X}_j + (2\mu + \lambda)\hat{Y}_i\hat{Y}_j - (\lambda + \mu)\delta_{ij}.$$

Continuing to use Ref. [102] notation, vectors \mathbf{v} and \mathbf{w} are defined:

$$\mathbf{v} = \sqrt{2\lambda + \mu}\hat{X} + \sqrt{-2\mu - \lambda}\hat{Y} \quad \text{and} \quad \mathbf{w} = \sqrt{2\lambda + \mu}\hat{X} - \sqrt{-2\mu - \lambda}\hat{Y}.$$

Now $|\mathbf{v}| = |\mathbf{w}| = \lambda - \mu$ and the angle between \mathbf{v} and \mathbf{w} is $\frac{3(\lambda+\nu)}{(\lambda-\nu)}$. Rewriting vectors \mathbf{c} and \mathbf{d} in rescaled form as

$$\mathbf{v} = \left(6q \frac{|\mathbf{d}|}{|\mathbf{c}|}\right)^{1/2} \mathbf{c} \quad \text{and} \quad \mathbf{w} = \left(6q \frac{|\mathbf{c}|}{|\mathbf{d}|}\right)^{1/2} \mathbf{d},$$

one finds:

$$Q_{ij}^C = \frac{1}{2}(c_i d_j + c_j d_i) - \frac{1}{3}(\mathbf{c} \cdot \mathbf{d})\delta_{ij}.$$

Discussing special cases now, if vectors \mathbf{v} and \mathbf{w} are orthogonal, then $\lambda = -\nu$. Using axes as defined above, this represents a square planar quadrupole which is located in the XY plane where

$$\mathbf{Q}^C = \begin{pmatrix} \lambda & 0 & 0 \\ 0 & -\lambda & 0 \\ 0 & 0 & 0 \end{pmatrix}.$$

In a similar way, a linear quadrupole with a natural body axis in the \hat{Z} direction can be written:

$$\mathbf{Q}^C = \begin{pmatrix} \nu & 0 & 0 \\ 0 & \nu & 0 \\ 0 & 0 & -2\nu \end{pmatrix} \quad \text{or} \quad \mathbf{Q}^C = \begin{pmatrix} 2\nu & 0 & 0 \\ 0 & -\nu & 0 \\ 0 & 0 & -\nu \end{pmatrix}.$$

If needed, the tensor components Q_{11}^C , Q_{22}^C , Q_{12}^C , Q_{13}^C , and Q_{23}^C can be written in terms of the five multipole moments associated with $l = 2$ (Ref. [103]):

$$q_{lm} = \int Y_{lm}^*(\theta', \phi') r'^l \rho(\mathbf{r}') d^3 r'.$$

B.8 Alternative method for calculating correction factor B

Here, the method of calculation the quadrupole correction factor B is explained. We start from Eq.4.31, which reads:

$$\frac{1}{3}\Theta_{\alpha\beta}(\mathbf{r}) = \epsilon_0\chi_Q\left(\partial_\alpha E_\beta^0(\mathbf{r}) + \frac{1}{24\pi\epsilon_0}\int_{|\mathbf{r}-\mathbf{r}'|>0} T_{\alpha\beta\gamma\delta}(|\mathbf{r}-\mathbf{r}'|)\Theta_{\gamma\delta}(\mathbf{r})d\mathbf{r}'\right). \quad (\text{B.57})$$

We reason in analogy to the dipole case. For dipoles, one considers a constant electric field oriented in the \hat{z} direction. Then the dipole correction factor A, Eq. (4.11), is derived. For quadrupoles, we must consider a constant gradient electric field and its effect of the orientation of an isolated quadrupole. This can be done using the dyadic forms for both $\Theta_{\alpha,\beta}$ and $\partial_\alpha E_\beta^0$, see Sec. 4.2.3. Using that notation, $\Theta = \lambda\hat{X}\hat{X} + \mu\hat{Y}\hat{Y} + \nu\hat{Z}\hat{Z}$ and $\nabla\mathbf{E}^0 = \lambda'\hat{X}'\hat{X}' + \mu'\hat{Y}'\hat{Y}' + \nu'\hat{Z}'\hat{Z}'$. The quadrupole orients itself into its lowest energy state; Cartesian axes \hat{X} , \hat{Y} , and \hat{Z} and \hat{X}' , \hat{Y}' , and \hat{Z}' align, as explained previously. Then both $\Theta_{\alpha,\beta}$ and $\partial_\alpha E_\beta^0$ are diagonal and can be written simply in terms of their eigenvalues.

Now the contraction $T_{\alpha\beta\gamma\delta}\Theta_{\gamma\delta}$ can be more easily considered. The only components of $T_{\alpha\beta\gamma\delta}$ that are required are the nine terms with $(\alpha, \beta) = (11), (22), (33)$ and $(\gamma, \delta) = (11), (22), (33)$. Because of the symmetry of $T_{\alpha\beta\gamma\delta}$, the nine terms can be used to write a symmetric matrix:

$$\mathbf{M}(R) = \begin{pmatrix} T_{1111}(R) & T_{1122}(R) & T_{1133}(R) \\ T_{2211}(R) & T_{2222}(R) & T_{2233}(R) \\ T_{3311}(R) & T_{3322}(R) & T_{3333}(R) \end{pmatrix}$$

where $\mathbf{R} = \mathbf{r} - \mathbf{r}'$, $R = |\mathbf{r} - \mathbf{r}'|$, and $\mathbf{R}_1 = X$, etc. Taking for example the case of

a point quadrupole (Eq. 4.27 of the paper):

$$\begin{aligned}
T_{\alpha\beta\gamma\epsilon}(R) &= (\delta_{\alpha\beta}\delta_{\gamma\epsilon} + \delta_{\alpha\gamma}\delta_{\beta\epsilon} + \delta_{\beta\gamma}\delta_{\alpha\epsilon}) v_{41}(R) \\
&+ (R_{\alpha}R_{\beta}\delta_{\gamma\epsilon} + R_{\alpha}R_{\gamma}\delta_{\beta\epsilon} + R_{\alpha}R_{\epsilon}\delta_{\beta\gamma} + R_{\beta}R_{\gamma}\delta_{\alpha\epsilon} + R_{\beta}R_{\epsilon}\delta_{\alpha\gamma} + R_{\gamma}R_{\epsilon}\delta_{\alpha\beta}) v_{42}(R)/R^2 \\
&+ R_{\alpha}R_{\beta}R_{\gamma}R_{\epsilon} v_{43}(R)/R^4,
\end{aligned}$$

we explicitly find:

$$\begin{aligned}
T_{1111}(R) &= 3v_{41}(R) + 6X^2v_{42}(R)/R^2 + X^4v_{43}(R)/R^4 \\
T_{2222}(R) &= 3v_{41}(R) + 6Y^2v_{42}(R)/R^2 + Y^4v_{43}(R)/R^4 \\
T_{3333}(R) &= 3v_{41}(R) + 6Z^2v_{42}(R)/R^2 + Z^4v_{43}(R)/R^4 \\
T_{1122}(R) &= T_{2211}(R) = v_{41}(R) + (X^2 + Y^2)v_{42}(R)/R^2 + X^2Y^2v_{43}(R)/R^4 \\
T_{1133}(R) &= T_{3311}(R) = v_{41}(R) + (X^2 + Z^2)v_{42}(R)/R^2 + X^2Z^2v_{43}(R)/R^4 \\
T_{2233}(R) &= T_{3322}(R) = v_{41}(R) + (Y^2 + Z^2)v_{42}(R)/R^2 + Y^2Z^2v_{43}(R)/R^4.
\end{aligned}$$

Now we follow Neumann and Steinhäuser and Fourier transform Eq. (4.31). Then we assume that the applied field gradient is homogeneous over the entire volume (tensor \mathbf{G} is a constant), the only relevant contribution of the interaction tensor is at $\mathbf{k} = 0$. Schematically, the form of the equation is:

$$\frac{1}{3} \begin{pmatrix} \lambda \\ \mu \\ \nu \end{pmatrix} = \epsilon_0 \chi_q \begin{pmatrix} \lambda' \\ \mu' \\ \nu' \end{pmatrix} + \frac{\chi_q}{24\pi} \begin{pmatrix} \tilde{T}_{1111}(0) & \tilde{T}_{1122}(0) & \tilde{T}_{1133}(0) \\ \tilde{T}_{2211}(0) & \tilde{T}_{2222}(0) & \tilde{T}_{2233}(0) \\ \tilde{T}_{3311}(0) & \tilde{T}_{3322}(0) & \tilde{T}_{3333}(0) \end{pmatrix} \begin{pmatrix} \lambda \\ \mu \\ \nu \end{pmatrix}. \quad (\text{B.58})$$

The matrix in this equation is the Fourier transform of matrix $\mathbf{M}(R)$ evaluated at

$\mathbf{k} = 0$, which would be written as $\tilde{M}(0)$, and shows the nine needed components of $\tilde{T}_{\alpha\beta\gamma\epsilon}(0)$ to be computed. Factors such as X^2 , Y^2 , and X^2Y^2 get angle averaged, and the nine components are given a temporary name. For example,

$$\begin{aligned}\tilde{T}_{1111}(0) &= \int_{\text{cutoff sphere}} [3v_{41}(R) + 6X^2v_{42}(R)/R^2 + X^4v_{43}(R)/R^4] d^3R \\ &= 12\pi \int_0^{R_c} [v_{41}(R) + \frac{2}{3}v_{42}(R) + \frac{1}{15}v_{43}(R)] R^2 dR = 3B'\end{aligned}$$

and

$$\begin{aligned}\tilde{T}_{1122}(0) &= \int_{\text{cutoff sphere}} [v_{41}(R) + (X^2 + Y^2)v_{42}(R)/R^2 + X^2Y^2v_{43}(R)/R^4] d^3R \\ &= 4\pi \int_0^{R_c} [v_{41}(R) + \frac{2}{3}v_{42}(R) + \frac{1}{15}v_{43}(R)] R^2 dR = B' .\end{aligned}$$

Now we see that

$$\tilde{\mathbf{M}}(0) = \begin{pmatrix} 3B' & B' & B' \\ B' & 3B' & B' \\ B' & B' & 3B' \end{pmatrix} .$$

Then Eq. (B.58) can be written as three separate equations:

$$\begin{aligned}\lambda &= \epsilon_0\chi_q\lambda' + \frac{\chi_q}{8\pi}(3B'\lambda + B'\mu + B'\nu) \\ \mu &= \epsilon_0\chi_q\mu' + \frac{\chi_q}{8\pi}(B'\lambda + 3B'\mu + B'\nu) \\ \nu &= \epsilon_0\chi_q\nu' + \frac{\chi_q}{8\pi}(B'\lambda + B'\mu + 3B'\nu)\end{aligned}$$

Using the traceless condition $\lambda + \mu + \nu = 0$, we find

$$\lambda = \frac{3\epsilon_0\chi_q\lambda'}{1 - \frac{\chi_q B'}{4\pi}}, \text{ etc.}$$

Comparing with Eq. (4.36),

$$\frac{\Theta}{3} = \mathbf{Q} - \frac{1}{3}\mathbf{1} = \frac{\epsilon_0\chi_q}{1 - \chi_q B} \nabla \mathbf{E}^0 = \frac{\epsilon_0\chi_q\lambda'}{1 - \frac{\chi_q B'}{4\pi}} \quad (\text{B.59})$$

from which we find $B'/(4\pi) = B$ and thus

$$B = \int_0^{R_c} \left[v_{41}(R) + \frac{2}{3}v_{42}(R) + \frac{1}{15}v_{43}(R) \right] R^2 dR. \quad (\text{B.60})$$

BIBLIOGRAPHY

1. Adams, D.; Adams, E. *Mol. Phys.* **1981**, *42*, 907–926.
2. Neumann, M. *Mol. Phys.* **1983**, *50*, 841–858.
3. Adams, D. *Mol. Phys.* **1980**, *40*, 1261–1271.
4. Perram, J. W.; Petersen, H. G.; Leeuw, S. W. D. *Mol. Phys.* **1988**, *65*, 875–893.
5. Shimada, J.; Kaneko, H.; Takada, T. *J. Comput. Chem.* **1993**, *14*, 867–878.
6. Luty, B. A.; Tironi, I. G.; Van Gunsteren, W. F. *J. Chem. Phys.* **1995**, *103*, 3014–3021.
7. Darden, T.; York, D.; Pedersen, L. *J. Chem. Phys.* **1993**, *98*, 10089–10092.
8. Essmann, U.; Perera, L.; Berkowitz, M. L.; Darden, T.; Lee, H.; Pedersen, L. G. *J. Chem. Phys.* **1995**, *103*, 8577–8593.
9. Roberts, J. E.; Schnitker, J. *J. Chem. Phys.* **1994**, *101*, 5024–5031.
10. Roberts, J. E.; Schnitker, J. *J. Phys. Chem.* **1995**, *99*, 1322–1331.
11. Luty, B. A.; van Gunsteren, W. F. *J. Phys. Chem.* **1996**, *100*, 2581–2587.
12. Hünenberger, P. H.; McCammon, J. A. *J. Chem. Phys.* **1999**, *110*, 1856–1872.

13. Hünenberger, P. H.; McCammon, J. A. *Biophys. Chem.* **1999**, *78*, 69–88.
14. Weber, W.; Hünenberger, P. H.; McCammon, J. A. *J. Phys. Chem. B* **2000**, *104*, 3668–3675.
15. Fennell, C. J.; Gezelter, J. D. *J. Chem. Phys.* **2006**, *124*, 234104.
16. Wolf, D.; Keblinski, P.; Phillpot, S. R.; Eggebrecht, J. *J. Chem. Phys.* **1999**, *110*, 8254–8282.
17. Dirk, Z.; Bernd, S.; Stefan, M. K. *J. Phys. Chem. B* **2002**, *106*, 10725–10732.
18. Gezelter, J. D.; Lamichhane, M.; Michalka, J.; Loudon, P.; Stocker, K. M.; Kuang, S.; Marr, J.; Li, C.; Vardeman, C. F.; Lin, T.; Fennell, C. J.; Sun, X.; Daily, K.; Zheng, Y.; Meineke, M. A. *OpenMD*; An open source molecular dynamics engine, version 2.4, <http://openmd.org> (accessed 4/8/2016).
19. Born, M.; Karman, T. V. *Physik* **1912**, *Z*, 297.
20. Allen, M. P. Introduction to molecular dynamics simulation. 2004.
21. Metropolis, N.; Rosenbluth, A. W.; Rosenbluth, M. N.; Teller, A. H.; Teller, E. *J. Chem. Phys.* **1953**, *21*, 1087–1092.
22. Allen, M. P.; Tildesley, D. J. *Computer Simulation of Liquids*; Clarendon Press: New York, NY, USA, 1989.
23. Toukmaji, A. Y.; Jr., J. A. B. *Comput. Phys. Commun.* **1996**, *95*, 73 – 92.
24. Rycerz, Z. A.; Jacobs, P. W. M. *Mol. Simul.* **1992**, *8*, 197–213.
25. Hockney, R. W.; Eastwood, J. W. *Computer simulation using particles*; CRC Press, 1988.

- 26. Luty, B. A.; Davis, M. E.; Tironi, I. G.; Gunsteren, W. F. V. *Mol. Simul.* **1994**, *14*, 11–20.
- 27. Rajagopal, G.; Needs, R. *J. Comput. Phys.* **1994**, *115*, 399 – 405.
- 28. Fukuda, I. *J. Chem. Phys.* **2013**, *139*, 174107.
- 29. Lamichhane, M.; Gezelter, J. D.; Newman, K. E. *J. Chem. Phys.* **2014**, *141*, 134109.
- 30. Kast, S. M.; Schmidt, K. F.; Schilling, B. *Chem. Phys. Lett.* **2003**, *367*, 398–404.
- 31. Beck, D.; Armen, R.; Daggett, V. *Biochem.* **2005**, *44*, 609–616.
- 32. Ma, Y.; Garofalini, S. H. *Mol. Simul.* **2005**, *31*, 739–748.
- 33. Chen, Y.; Kaur, C.; Weeks, J. *J. Phys. Chem. B* **2004**, *108*, 19874–19884.
- 34. Chen, Y.; Weeks, J. *Proc. Natl. Acad. Sci.* **2006**, *103*, 7560–7565.
- 35. Rodgers, J. M.; Kaur, C.; Chen, Y.-G.; Weeks, J. D. *Phys. Rev. Lett.* **2006**, *97*, 097801.
- 36. Denesyuk, N. A.; Weeks, J. D. *J. Chem. Phys.* **2008**, *128*, 124109.
- 37. Izvekov, S.; Swanson, J. M. J.; Voth, G. A. *J. Phys. Chem. B* **2008**, *112*, 4711–4724.
- 38. Hansen, J. S.; Schroder, T. B.; Dyre, J. C. *J. Phys. Chem. B* **2012**, *116*, 5738–5743.
- 39. Shi, W.; Luebke, D. R. *Langmuir* **2013**, *29*, 5563–5572.

- 40. McCann, B. W.; Acevedo, O. *J. Chem. Theory Comput.* **2013**, *9*, 944–950.
- 41. Kannam, S. K.; Todd, B. D.; Hansen, J. S.; Daivis, P. J. *J. Chem. Phys.* **2013**, *138*, 094701.
- 42. Forrest, K. A.; Pham, T.; McLaughlin, K.; Belof, J. L.; Stern, A. C.; Zaworotko, M. J.; Space, B. *J. Phys. Chem. C* **2012**, *116*, 15538–15549.
- 43. English, N. J. *Mol. Phys.* **2008**, *106*, 1887–1898.
- 44. Loudon, P.; Schoenborn, R.; Lawrence, C. P. *Fluid Phase Equilib.* **2013**, *349*, 83–86.
- 45. Tokumasu, T.; Meurisse, M.-H.; Fillot, N.; Vergne, P. *Tribol. Int.* **2013**, *59*, 10–16.
- 46. Golubkov, P. A.; Ren, R. *J. Chem. Phys.* **2006**, *125*, 064103.
- 47. Orsi, M.; Michel, J.; Essex, J. W. *J. Phys. Cond. Matt.* **2010**, *22*, 155106.
- 48. Orsi, M.; Essex, J. W. *PLoS One* **2011**, *6*, e28637.
- 49. Chowdhuri, S.; Tan, M.-L.; Ichiye, T. *J. Chem. Phys.* **2006**, *125*, 144513.
- 50. Te, J. A.; Tan, M.-L.; Ichiye, T.
- 51. Te, J. A.; Ichiye, T. *J. Chem. Phys.* **2010**, *132*, 114511.
- 52. Te, J. A.; Ichiye, T. *Chem. Phys. Lett.* **2010**, *499*, 219–225.
- 53. Ichiye, T.; Tan, M.-L. *J. Chem. Phys.* **2006**, *124*, 134504–10.

54. Ponder, J. W.; Wu, C.; Ren, P.; Pande, V. S.; Chodera, J. D.; Schnieders, M. J.; Haque, I.; Mobley, D. L.; Lambrecht, D. S.; DiStasio, R. A., Jr; Head-Gordon, M.; Clark, G. N. I.; Johnson, M. E.; Head-Gordon, T. *J. Phys. Chem. B* **2010**, *114*, 2549–64.
55. Schnieders, M. J.; Baker, N. A.; Ren, P.; Ponder, J. W. **2007**, *126*, 124114.
56. Ren, P.; Wu, C.; Ponder, J. W. *J. Chem. Theory Comput.* **2011**, *7*, 3143–3161.
57. de Leeuw, S. W.; Perram, J. W.; Smith, E. R. *Proc. R. Soc. London Ser. A* **1980**, *373*, 27–56.
58. Fukuda, I.; Yonezawa, Y.; Nakamura, H. *J. Chem. Phys.* **2011**, *134*, 164107.
59. Fukuda, I.; Kamiya, N.; Yonezawa, Y.; Nakamura, H. *J. Chem. Phys.* **2012**, *137*, 054314.
60. Allen, M. P.; Germano, G. *Mol. Phys.* **2006**, *104*, 3225–3235.
61. Price, S.; Stone, A.; Alderton, M. *Mol. Phys.* **1984**, *52*, 987–1001.
62. Lamichhane, M.; Gezelter, J. D.; Newman, K. E. *J. Chem. Phys.* **2014**, *141*, 134109.
63. Smith, W. *CCP5 Information Quarterly* **1982**, *4*, 13–25.
64. Smith, W. *CCP5 Information Quarterly* **1998**, *46*, 18–30.
65. Aguado, A.; Madden, P. A. *J. Chem. Phys.* **2003**, *119*, 7471–7483.
66. Sauer, J. A. *Phys. Rev.* **1940**, *57*, 142–146.
67. Luttinger, J. M.; Tisza, L. *Phys. Rev.* **1946**, *70*, 954–964.

- 68. Luttinger, J. M.; Tisza, L. *Phys. Rev.* **1947**, *72*, 257–257.
- 69. Nagai, O.; Nakamura, T. *Progr. Theoret. Phys.* **1960**, *24*, 432–454.
- 70. Nagai, O.; Nakamura, T. *Progr. Theoret. Phys.* **1963**, *30*, 412.
- 71. Wolf, D. *Phys. Rev. Lett.* **1992**, *68*, 3315–3318.
- 72. Wolf, D. In *Computer Simulation Studies in Condensed-Matter Physics VIII*; Landau, D., Mon, K., Schüttler, H.-B., Eds.; Springer Proceedings in Physics; Springer Berlin Heidelberg, 1995; Vol. 80; pp 57–68.
- 73. Lacman, R. *Colloq. Int. CNRS* **1965**, *152*, 195.
- 74. Wu, X.; Brooks, B. R. *J. Chem. Phys.* **2005**, *122*, 044107.
- 75. Dullweber, A.; Leimkuhler, B.; McLachlan, R. *J. Chem. Phys.* **1997**, *107*, 5840–5851.
- 76. Fisher, R. *Proc. R. Soc. Lond. A* **1953**, *217*, 295–305.
- 77. Allen, F. H.; Doyle, M. J.; Taylor, R. *Acta Cryst. B* **1991**, *47*, 29–40.
- 78. Impey, R. W.; Madden, P. A.; McDonald, I. R. *Mol. Phys.* **1982**, *46*, 513–539.
- 79. Kirkwood, J. G. *J. Chem. Phys.* **1939**, *7*, 911–919.
- 80. Onsager, L. *J. Am. Chem. Soc.* **1936**, *58*, 1486–1493.
- 81. Chitanvis, S. M. *J. Chem. Phys.* **1996**, *104*, 9065–9074.
- 82. Stern, H. A.; Feller, S. E. *J. Chem. Phys.* **2003**, *118*, 3401–3412.
- 83. Slavchov, R. I.; Ivanov, T. I. *J. Chem. Phys.* **2014**, *140*, 074503.

84. Slavchov, R. I. *J. Chem. Phys.* **2014**, *140*, 164510.
85. Neumann, M.; Steinhauser, O. *Chem. Phys. Lett.* **1983**, *95*, 417 – 422.
86. Ernst, R. M.; Wu, L.; Liu, C. H.; Nagel, S. R.; Neubert, M. E. *Phys. Rev. B* **1992**, *45*, 667–672.
87. Jeon, J.; Kim, H. J. *J. Chem. Phys.* **2003**, *119*, 8606–8625.
88. Jeon, J.; Kim, H. J. *J. Chem. Phys.* **2003**, *119*, 8626–8635.
89. Lamichhane, M.; Newman, K. E.; Gezelter, J. D. *J. Chem. Phys.* **2014**, *141*, 134110.
90. Neumann, M.; Steinhauser, O.; Pawley, G. S. *Mol. Phys.* **1984**, *52*, 97–113.
91. Neumann, M. *J. Chem. Phys.* **1985**, *82*, 5663–5672.
92. Stenqvist, B.; Trulsson, M.; Abrikosov, A. I.; Lund, M. *J. Chem. Phys.* **2015**, *143*, 014109.
93. Adu-Gyamfi, D. *Physica A* **1978**, *93*, 553 – 558.
94. Adu-Gyamfi, D. *Physica A* **1981**, *108*, 205 – 210.
95. Logan, D. E. *Mol. Phys.* **1981**, *44*, 1271–1295.
96. Logan, D. E. *Mol. Phys.* **1982**, *46*, 271–285.
97. Logan, D. E. *Mol. Phys.* **1982**, *46*, 1155–1194.
98. Trzesniak, D.; Kunz, A.-P. E.; van Gunsteren, W. F. *ChemPhysChem* **2007**, *8*, 162–169.
99. Fixman, M. *Proc. Natl. Acad. Sci. USA* **1974**, *71*, 3050–3053.

100. Meineke, M. A.; Vardeman II, C. F.; Lin, T.; Fennell, C. J.; Gezelter, J. D. *J. Comp. Chem.* **2005**, *26*, 252–271.
101. Adams, D. J.; McDonald, I. R. *Molecular Physics* **1976**, *32*, 931–947.
102. Torres del Castillo, G. F.; Méndez Garrido, A. *Revista Mexicana de Física* **2006**, *52*, 501–506.
103. Jackson, J. D. *Classical Electrodynamics Third Edition*, 3rd ed.; Wiley, 1998.
104. Morse, P.; Feshbach, H. *Methods of Theoretical Physics*; Technology Press, 1946.
105. Stone, A. *The Theory of Intermolecular Forces*; International Series of Monographs on Chemistry; Clarendon Press, 1997.
106. Raab, R.; de Lange, O. *Multipole Theory in Electromagnetism: Classical, quantum, and symmetry aspects, with applications*; International Series of Monographs on Physics; OUP Oxford, 2004.
107. Arfken, G. B.; Weber, H. J.; Harris, F. E. *Mathematical Methods for Physicists*, 6th ed.; Academic Press, 2005.

<p><i>This document was prepared & typeset with pdfL^AT_EX, and formatted with NDdiss2_ε classfile (v3.0[2005/07/27]) provided by Sameer Vijay.</i></p>
